RICE UNIVERSITY

Interactions of Amyloid-Forming Peptides with Lipid Bilayer Membranes

by

Chang-Chun Lee

A THESIS SUBMITTED
IN PARTIAL FULFILLMENT OF THE
REQUIREMENTS FOR THE DEGREE

Doctor of Philosophy

APPROVED, THESIS COMMITTEE

Huey W. Huang, Chair
Professor,
Physics and Astronomy

Jason H. Hafner
Associate Professor,
Physics and Astronomy and Chemistry

Sibani Lisa Biswal
Assistant Professor,
Chemical and Biomolecular Engineering

HOUSTON, TEXAS
APRIL 2012

Abstract

Interactions of Amyloid-Forming Peptides with Lipid Bilayer Membranes

by

Chang-Chun Lee

Amyloid-proteins are among the most actively researched biological topics today, because they have been associated with many serious human diseases, such as Alzheimer's disease and type II diabetes. In particular the deposition of protein aggregates on cell membranes has been suspected as the causes of the diseases, although the proof is still elusive. Studying the interactions of amyloid-forming peptides with lipid-bilayer membranes may clarify the pathway of the β-aggregate formation and provide new insights into the amyloid hypothesis of diseases.

In this thesis, I investigate how three peptides, penetratin, amylin, and LL-37, interact with lipid membranes by using several techniques well-developed in our lab. In the study of penetratin interacting with lipid membranes, we were able to clarify the energy pathway of amyloid formation mediated by membrane-binding. This provides the sole experimental proof for the Jarrett-Lansbury theory of β-amyloid formation. Our investigation on amylin-membrane interaction clarifies how amylin in different forms damage bilayer membranes. Between penetratin and amylin we have clarified the complicated pattern of interactions between amyloid-forming peptides and lipid bilayers.

The third peptide LL-37 studied in my thesis turned out to a pore forming peptide. I found the mistake made by previous investigators in several different laboratories that made them erroneously conclude that LL-37 was not a pore forming peptide. The results of these three peptides show that methods we used are a comprehensive set of tools that can reveal a broad range of peptide properties.

Both the formation of amyloid aggregates and formation of membrane pores can be explained by a two-state model proposed by Huang describing peptide-membrane interactions. For LL-37, the second state is a pore in membrane. But for penetratin and amylin the second state is an aggregation in the β form. We found that β-aggregates have low affinity within a lipid bilayer, and therefore exit from the bilayer structure. However, this exit process extracts lipid molecules from the bilayer and incorporates them in the peptide aggregates. We suggest that this is the molecular process of how amylin might damage of the membranes of β-cells.

Acknowledgments

I would like to express my great gratitude to my advisor, Dr. Huey W. Huang, for all his support and expert advice in my research projects. Without his advice and careful attention, this thesis would not have been possible.

I would like to thank Dr. Jason H. Hafner and Dr. Sibani Lisa Biswal for serving on my thesis committee, and for their interest and advice on my thesis.

I would like to thank my fellow graduate students Yen Sun, Shuo Qian, Wang-Chen Wang, and Tzu-Lin Sun for their assistance in the lab and helpful discussions for the research projects.

Finally, I would like to express my gratitude to all the members of my family, in particular, to my wife, Yen Sun, for their full support and encouragement during my journal of the academic study.

This work was supported in part by NIH (US) Grant GM55203, and by the Robert A. Welch Foundation Grant C-0991. Neutron experiment was performed at Oak Ridge National Laboratory; its High Flux Isotope Reactor was sponsored by the Scientific User Facilities Division, Office of Basic Energy Sciences, U. S. Department of Energy (DOE); its Center for Structural Molecular Biology was supported by the Office of Biological and Environmental Research, using facilities supported by the DOE, managed by UT-Battelle, LLC under Contract No.DE-AC05-00OR22725.

Contents

List of Figures

List of Tables

Chapter 1

Introduction

The lipid bilayers, thin membranes made of two layers of lipid molecules, constitute a continuous barrier of living cells. These sheet-like assembles play an important role in preventing ions, proteins, and other molecules from diffusing into areas where they should not be. Besides being the boundary of the cells, the lipid bilayers are natural binding sites for proteins, peptides and other amphipathic molecules. Many essential biological functions, such as ion transport [1], and cell fusion [2], are carried out by integrating these membrane proteins and molecules on the membrane. Lipid membranes, according to the fluid-mosaic model by Singer and Nicolson[3], are two-dimensional fluids of lipid molecules in which membrane proteins and other molecules, such as cholesterol, are embedded. The effects of these membrane proteins on the membranes and how the functions of proteins are affected by the membrane are very essential issues in biology but still not very well studied. Because of the complexity of biological membranes, it is difficult to study

these membranes, consisting of phospholipids, proteins, and many other molecules, in their native states. In order to perform biophysical studies, model membranes, made of phospholipid in which specific target protein or peptide is embedded, have generally been used in experiments. Phospholipids are the major component of cell membranes as they can form lipid bilayers in biological environment. Lipid molecule generally consists of a hydrophilic head and hydrophobic tails. The hydrophilic phosphate headgroup and one or two hydrophobic fatty acid chains make phospholipids amphiphilic molecules (Fig. 1-1). This amphiphilic property allows lipids spontaneously to form small vesicles in water solution, or to arrange themselves into multilayer structure with water layers in between when depositing on the flat substrate.

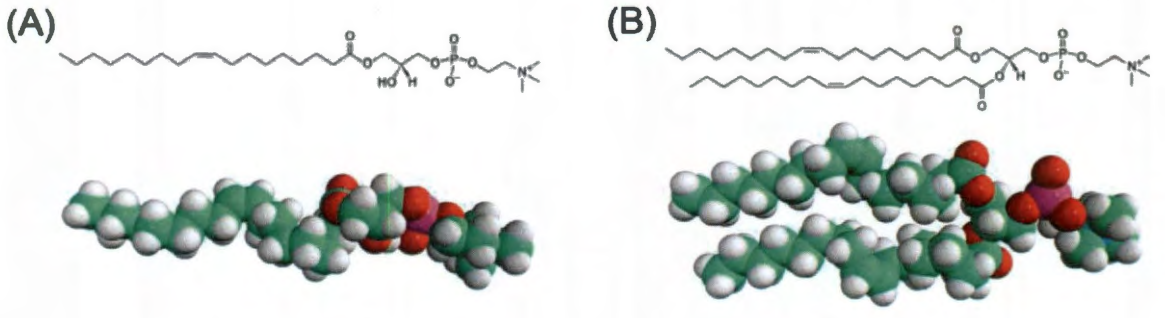

Figure 1-1 The structure formula (top) and the space-filling model (bottom) for the phospholipid molecule. (A) 1-oleoyl-2-hydroxy-*sn*-glycero-3-phosphocholine, or 18:1 Lyso PC, as an example of a one-chain phospholipid molecule. (B) 1,2-dioleoyl-sn-glycero-3-phosphocholine, or DOPC, as an example of a two-chains phospholipid molecule.

One of the primary goals of our membrane biophysics laboratory is to study small membrane-active peptides interacting with lipid membranes. Peptides, which are distinguished from proteins by their sizes, typically contain 20-50 amino acids. Several techniques, such as X-ray lamellar diffraction, neutron in-plane scattering, oriented circular dichroism, and giant unilamellar vesicle aspiration method, have been well-developed in our lab to investigate the peptide-lipid interactions. Because of the amphiphilic property of lipid molecules, lipids in the bilayer form spontaneously arrange themselves into multilayer structures on the substrate. The regularity of the multilayer peptide-lipid samples allows us to investigate the structures of the peptide-containing bilayers by X-ray diffraction [4]. The electron density profile of the bilayer reveals how peptides interact with lipid bilayers. The technique of neutron in-plane scattering [5] is the only method that has successfully detected and measured the pores formed by antimicrobial peptides in membranes. This technique makes use of the large contrast between the neutron scatterings by hydrogen and deuterium. The detail information about the size of pores can be analyzed from the neutron scattering data. The oriented circular dichroism, invented in our lab by Wu et al. in 1990 [6], is the simplest method that can be used to detect the orientation of the α-helical peptides in membranes. The results of oriented circular dichroism of peptide orientation can be correlated with the results of X-ray diffraction of membrane thickness to understand the process of pore formation. Then by use of the GUV aspiration method [7, 8], the peptide-lipid interactions can be observed in the water solution, which is the ideal environment of living cells. The GUV experiments can be performed not only to confirm the

results obtained from multilayer samples by X-ray diffraction and oriented circular dichroism but also to investigate the dynamic process of peptides interacting with lipid membranes. By correlating the results of this diverse set of experimental methods, we gain a better understanding of how different types of peptides interact with bilayer membranes.

With the techniques initially developed in our laboratory for the studies of antimicrobial peptides, I further extend my research area into the study of amyloid-forming peptides. Amyloids, formed by proteins and polypeptides which are naturally produced in our body, are insoluble fibrous protein aggregates. These "misfolded" structures alter the functions of original proteins and result in improper interaction between one another or with other cellular components causing plagues. They have been associated with many serious human diseases, like Alzheimer's disease and type II diabetes, and are considered as a very important topic in biological studies today. Although the causes of these amyloid-related diseases are still not clear, one hypothesis is that amyloid fibrous aggregates are abnormally deposited on cell membranes and cause harm to organs or tissues. Thus investigations on how amyloid-forming peptides interacting with lipid bilayers may provide insights into this topic. However, the tendency of amyloid-forming proteins, like β-amyloid peptides 1-40 and Aβ 1-42 (the major component of Alzheimer's disease), to self-aggregate [9] makes the biophysical experiments difficult to perform. To understand the mechanism of β-amyloid formation, we choose a 16-reside peptide penetratin to investigate how amyloid-forming peptides interacting with lipid bilayers. Both Aβ 1-40 and penetratin are random coils in solution but

change to α-helical or β-like conformations in the presence of lipid membranes. The spectra of both peptides change from α-helical to β-like conformations as the lipid charge increases or as the peptide concentration increases [9-14]. The main difference is that these changes for penetratin occur in higher concentrations than for Aβ 1-40. We are able to observe very explicitly configurational changes of penetratin in equilibrium states as well as during dynamic processes. Our experimental results support Jarrett-Lansbury's nucleation-dependent polymerization theory which was proposed to describe the generic process of β-amyloid formation. Most importantly, we have demonstrated the catalytic role of membrane binding in the formation β-amyloid.

Another study of amyloid-forming peptides is to investigate how human islet amyloid polypeptide (amylin or hIAPP, the type II diabetes related amyloid peptide) interacting with lipid membranes. One possible cause of impaired insulin secretion in type II diabetes is the decimation of insulin-producing β-cells [15]. Prevailing hypotheses that explain the underlying cell attrition is the deleterious effects on the cell membranes by hIAPP, a 37-residue peptide which is synthesized in pancreatic islet beta-cells and cosecreted with insulin [16-20]. A large body of research has described the phenomena of hIAPP interactions with lipid bilayers. However, it has been difficult to correlate the effects on lipid bilayers with the effects of hIAPP added to islet cells in culture, which indeed induce cell death. Our experimental results provide new structural information about the hIAPP-membrane interactions and reveal a low threshold peptide concentration for damaging the membranes. The new structural information is that the β-aggregates of hIAPP bind on the surface

of lipid bilayers. This is true even when the β-aggregates originated from α-helical hIAPPs bind inside the headgroup region of lipid bilayers. This behavior of hIAPPs is identical to penetratin. Thus, it could be a common pattern of interaction between amyloid-forming peptides and lipid bilayers. i.e., the peptides bind as α-helical inside the head group region of the bilayer, but once peptides convert to β-aggregates, they bind on the surface of the bilayer.

Antimicrobial peptides are naturally produced innate immune factors found in every plant and animal, in fact in every organism, the researchers have looked into. They are known to kill microorganisms by targeting directly their cellular membranes. The studies of antimicrobial peptides have attracted more and more attentions not only because of their ubiquitous presence in nature but also because they may be used as therapeutics. During the past two decades, the richness of antimicrobial peptide problems has provided very interesting research in our lab. Among many advances this lab has made, we have resolved the structures for the two types of pores formed by antimicrobial peptides [21]. One is the barrel-stave type pore formed by alamethicin, and the other is the toroidal type pore formed by all other antimicrobial peptides like melittin or magainin. With our understanding of antimicrobial peptides, it is reasonable to make a comparison between antimicrobial peptides and amyloid-forming peptides. I chose to study human antimicrobial peptide LL-37 because this was a controversial peptide at the time. LL-37 is a multifunctional cathelicidin peptide that has shown a wide spectrum of antimicrobial activity. It is significant that despite the versatile multi-functionality of LL-37, experimental results suggest that its molecular mechanism for direct

antimicrobial activity is similar to that of smaller antimicrobial peptides. Yet numerous reports declared that LL-37 is not a pore-forming peptide. I am pleased to report that my experiments have resolved the controversy. I found that LL-37 does make transmembrane pores. I have measured the pore size and recorded the leakage activity resulted from LL-37 forming pores on lipid vesicle.

Based on the experiments of many different antimicrobial peptides, such as alamethicin, melittin, and magainin, Huang proposed a two-state model [22] to describe the general mechanism of antimicrobial peptides interacting with lipid membranes. In this two-state model, each peptide has two distinct physical states when bound to the lipid bilayers. At low peptide-to-lipid (P/L) ratio, peptides energetically prefer to bind on the interface of lipid membranes which is in a functionally inactive state. Once the bound P/L exceeds a critical value P/L*, the excessive peptides transit to another energy state which form transmembrane pores. My experimental results of amyloid-forming peptides also follow a pattern of the two-state model. In this case, the second state of amyloid-forming peptides is β-aggregates on the membrane surface, instead of forming transmembrane pores. The phenomena are different but the energetics is the same. It is very satisfying to find that there is a unified picture of peptide-membrane interactions.

Chapter 2

Experimental Techniques

2.1. X-ray Lamellar Diffraction

2.1.1. Basic Theory

X-ray lamellar diffraction is an ideal technique to investigate the structure of the sample made of one-dimensional regular stacked multilayers of peptide-lipid mixtures. In our membrane biophysics laboratory, we have developed a complete method, including sample preparation, system setup and data analysis, for the X-ray lamellar diffraction to study the change of the lipid bilayer structure upon the addition of other amphipathic molecules, such as peptides and drugs. The precisely measurement of lipid bilayer structure obtaining from X-ray diffraction can reveal the information of how the target amphipathic molecule may interact with lipid bilayer membranes. The basic physics and equations of X-ray diffraction as applied to lamellar samples will be briefly described in the following.

We first define the momentum transfer vector as the difference between the incoming beam $\boldsymbol{k}_i$ and the diffracted beam $\boldsymbol{k}_f$, i.e.

$$\boldsymbol{q} = \boldsymbol{k}_f - \boldsymbol{k}_i \tag{2-1}$$

Since the energy of the radiation is not changed in the elastic scattering case, we have $|\boldsymbol{k}_f| = |\boldsymbol{k}_i| = 2\pi/\lambda$. The magnitude of the momentum transfer vector can be obtained from Fig. 2-1 as

$$|\boldsymbol{q}| = \frac{4\pi}{\lambda} Sin\theta \tag{2-2}$$

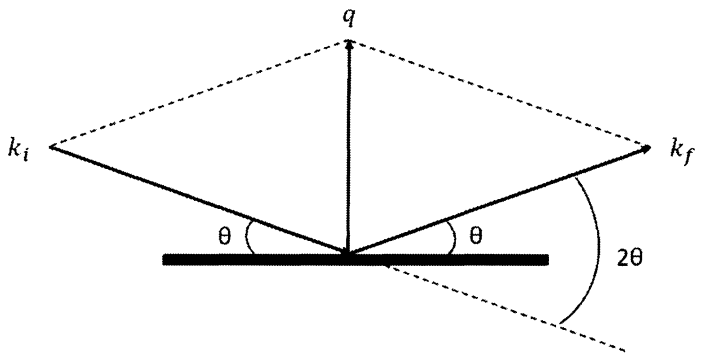

Figure 2-1 Schematic of momentum transfer vector q in the case of the elastic scattering.

The intensity of X-ray scattering is given as

$$I(\boldsymbol{q}) = I_e \left| \int_V \rho(\boldsymbol{r}) \exp(-i\boldsymbol{q}\cdot\boldsymbol{r}) d^3r \right|^2 \tag{2-3}$$

where $\rho(\boldsymbol{r})$ is the electron density of the sample of volume V and I_e is the intensity of scattering by a single free electron. Suppose we have a multilayer sample

composed of N bilayers, separated in the z-direction by a repeat distance D. Since the membranes are fluid in the x-y plane and peptides/lipids are homogenous distributed in the sample, the electron density is a constant within the x-y plane, i.e., $\rho(x,y,z) = \rho(z)$. We can then describe the sample, assuming that the stacked membrane have uniform lateral structure, with the equation

$$\rho(z) = \rho(z + nD) \qquad with\ -\frac{D}{2} \le z \le \frac{D}{2}, \quad n = 0,1,2,\dots,N-1 \tag{2-4}$$

where $\rho(z)$ is the electron density of a single bilayer in the sample.

Therefore, the integral in Eq. (2-3) can therefore be written as

$$\begin{aligned}\int_V \rho(\boldsymbol{r}) \exp(-i\boldsymbol{q}\cdot\boldsymbol{r})\, d^3r &= \int \rho(z)\ e^{-q_z z} dz \\ &= \sum_{n=0}^{N-1} \int_{-D/2}^{D/2} \rho(z) e^{-iq_z z} e^{-inq_z D} dz \\ &= \int_{-D/2}^{D/2} \rho(z) e^{-iq_z z} dz \sum_{n=0}^{N-1} e^{-inq_z D}\end{aligned} \tag{2-5}$$

The summation in the last line of Eq. (2-5) is a geometric series. By use of the fact that $\sum_{n=0}^{N-1} e^{inx} = (1 - e^{iNx})/(1 - e^{ix})$, this summation can be written as

$$\sum_{n=0}^{N-1} e^{-inq_z D} = \frac{\sin(N\frac{qD}{2})}{sin\frac{qD}{2}} \exp[-i(N-1)(qD/2)] \tag{2-6}$$

We can therefore rewrite the diffraction intensity from multilayer stacked membranes given in Eq. (2-3) as

$$I(q_z) = I_e \frac{\sin^2\left(N\frac{qD}{2}\right)}{sin^2\frac{qD}{2}} \left| \int_{-\frac{D}{2}}^{\frac{D}{2}} \rho(z) e^{-iq_z z} dz \right|^2$$

$$= I_e S(q_z) |F(q_z)|^2 \tag{2-7}$$

where we define the form factor of the bilayer, which is the Fourier transform of the electron density of the unit cell, as

$$F(q) = \int_{-\frac{D}{2}}^{\frac{D}{2}} \rho(z) e^{-iq_z z} dz \tag{2-8}$$

and the structure factor of the sample, which carries the information of the arrangement of the unit cells, as

$$S(q) = \frac{sin^2\left(N\frac{qD}{2}\right)}{sin^2(\frac{qD}{2})} \tag{2-9}$$

The function of structure factor S(q) is plotted in Fig. 2-2 for several values of N. In the case of large N, the structure factor only has appreciable values at points at

$$q = \frac{2\pi n}{D} \quad with \quad n = 0, \pm 1, \pm 2, \ldots \tag{2-10}$$

The value at the peak position is N^2 while the peaks has a width of $2\pi/(ND)$. Since from Eq. (2-2) we know that $q = (4\pi/\lambda)Sin\theta$, we can rewrite Eq. (2-10) as the equivalent expression of Bragg equation for a one-dimensional multilayers:

$$2DSin\theta = n\lambda \quad with \quad n = 0, \pm 1, \pm 2, \ldots \tag{2-11}$$

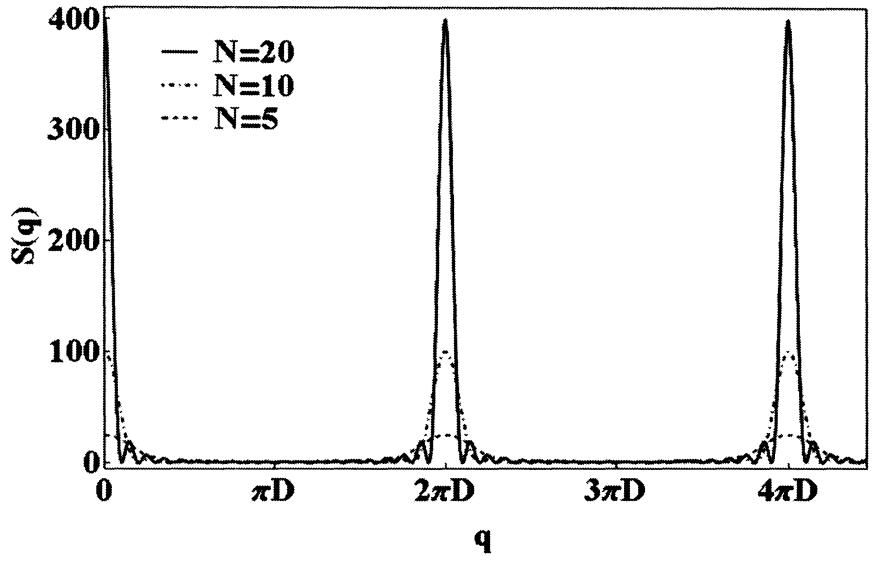

Figure 2-2 The structure factor for various values of N. The function peaks at $q=2\pi n/D$ with the peak vales of N^2.

In order to calculate the electron density from the measured intensities, we need the phases associated with them. Once the phases have been determined by the swelling method, the electron density profile can be reconstructed by

$$\rho(z) = \sum_{n=-\infty}^{\infty} \frac{1}{D} F(\frac{2\pi n}{D}) e^{-i\frac{2\pi}{D}nz} \tag{2-12}$$

Since the sine function is anti-symmetric and will be vanished after the summation, the equation above can be rewritten as

$$\rho(z) - \rho_0 = \frac{1}{d} \sum_{n=1}^{m} F(\frac{2\pi n}{D}) \cos(\frac{2\pi nz}{D}) \tag{2-13}$$

Because we cannot measure $F(n = 0)$ in the experiment, the reconstructed electron density profile will be on a relative scale

2.1.2. The Swelling Method

To reconstruct the electron density profile, we need to determine the phase of the observed amplitudes. This is the so-called phasing problem, which is the main challenge in the structure determination by X-ray diffraction.

It can be easily proved that the form factor give in Eq. (2-8) is independent of the repeat spacing D. The is also valid for the square modulus of F(q) and we can write the total scattering intensity as

$$\int_{-\infty}^{\infty} |F(q)|^2 dq = \frac{2\pi}{D} \sum_{n=-\infty}^{\infty} |F(\frac{2\pi n}{D})|^2 \tag{2-14}$$

by use of the following equation based on the Shannon theorem

$$F(q) = \sum_{n=-\infty}^{\infty} F\left(\frac{2\pi n}{D}\right) sinc(\frac{qD}{2} - n\pi) \tag{2-15}$$

and the orthogonality of sinc functions. For two different D-spacings at various hydration levels, we must require that their total diffracted intensities are equal, i.e.

$$\frac{2\pi}{D_1} \sum_{n=-\infty}^{\infty} |F(\frac{2\pi n}{D_1})|^2 = \frac{2\pi}{D_2} \sum_{n=-\infty}^{\infty} |F(\frac{2\pi n}{D_2})|^2 \tag{2-16}$$

This can be rewritten by using the fact that $F(2\pi n/D) = F(-2\pi n/D)$, and $F(0) \approx 0$ to give the scaling relation:

$$\frac{\sum_{n=1}^{\infty} |F(2\pi n/D_1)|^2}{\sum_{n=1}^{\infty} |F(2\pi n/D_2)|^2} = \frac{D_1}{D_2} \tag{2-17}$$

Using this relation to rescale the measured intensities for different swelling states and plotting them versus q, we are able to find the right phases associated with the measured amplitudes. An example of such a phasing diagram and its corresponding electron density profile is given in Fig. 2-3.

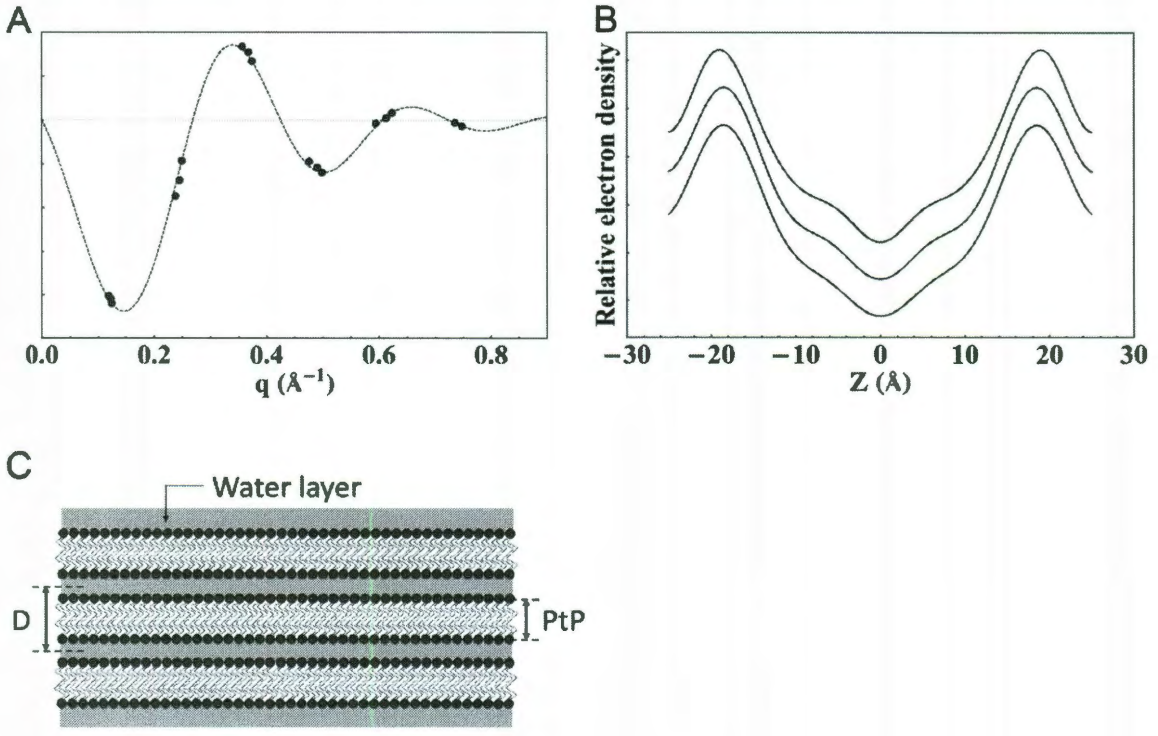

Figure 2-3 (A) The phasing diagram of pure DOPC at RH=92, 96 and 98% RH (from the larger q value to the smaller q value). (B) The corresponding relative electron density profiles of pure DOPC at RH=92, 96 and 98% RH (from top to bottom). (C)Schematic of multilayers sample of lipid membranes. PtP is the phosphate-to-phosphate distance, and D is the repeated water spacing between the multilayer sample.

2.1.3. Experimental Setup

ω-2θ diffraction experiment was performed on an Enraf Nonius Diffractis 581 sealed tube X-ray generator and a Huber (Huber Diffraktionstechnik, Rimsting, Germany) four-circle goniometer, with a line-focused Cu Kα source (λ = 1.542 Å) operating at 40 kV and 15-30 mA. The heated X-ray tube is cooled for the safety reason by a low-temperature water circulation system. At a 6° take-off angle, the X-ray incident beam was collimated by a horizontal soller slit and two vertical slits on the front and the back sides of the soller slit. The purpose of the soller slit is to reduce the horizontal divergence of the incident X-ray beam to the sample and the two vertical slits is used to adjust the vertical divergence of the incident X-ray beam. The resulting horizontal and vertical divergence of the incident beam were 0.23° and 0.3°, respectively. A schematic of the experiment setup is shown in Fig. 2-4.

The X-ray incident beam is carefully aligned to pass through the center of the goniometer in order to ensure the quality of the diffraction data. A needle is mounted on the goniometer in order to perform the alignment. A 2θ scan is performed twice when the needle is positioned at top and bottom of the circle. The position of the goniometer is adjusted until the intensity of 2θ scan with the presence of the needle is nearly half of that without the presence of the needle.

The diffracted beam from the multilayers sample first passed through a vertical slit and then was discriminated by a bent graphite monochromator before entering a PMT (photomultiplier tube) detector. The bent graphite crystal was oriented to reflect the diffraction signal into the detector and to discriminate against

higher harmonics and fluorescence. This diffractometer was designed to minimize the background signal, which in turn allowed the measurement of high diffraction orders. The diffraction signals detected by the PMT detector were then recorded by a LabVIEW program for further data analysis.

Our X-ray diffraction system is controlled by a LabVIEW program, which I develop to replace the old program on the NeXTSTEP system. This LabVIEW program can be used to control the mode of X-ray incident beam (ON/ OFF/ ATTENUATED), angle position of four-circle goniometer (with a smallest step 0.0025° in ω and 2θ circle), sample conditions inside the chamber (temperature and relative humidity), and PMT detector (acquisition time of the detector).

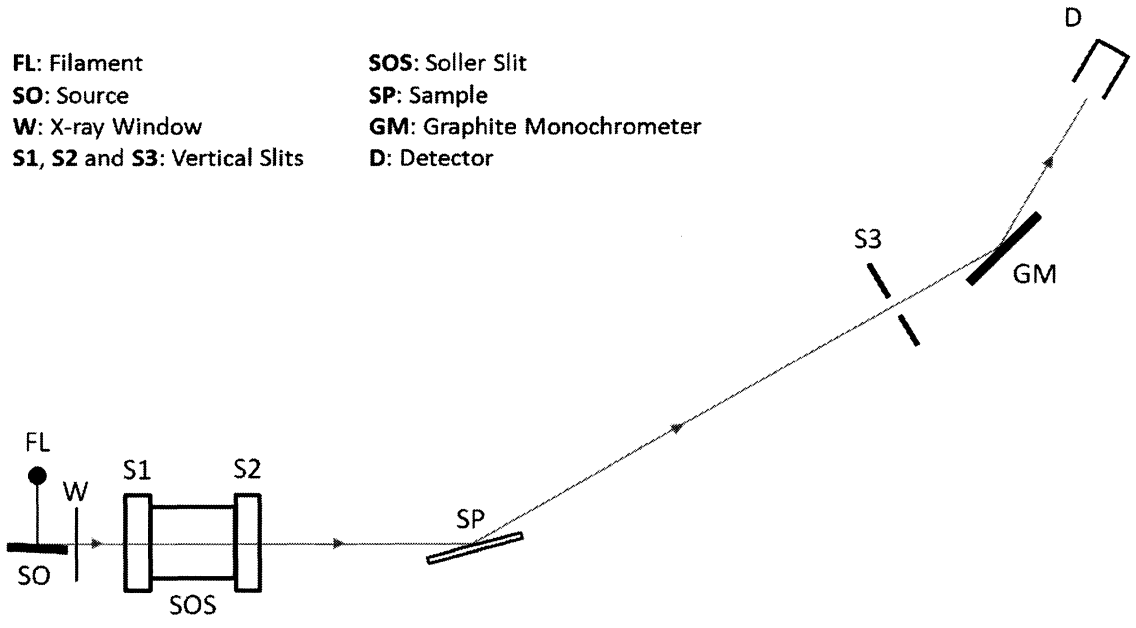

Figure 2-4 Schematic of the X-ray experimental setup for ω-2θ diffraction on the lipid bilayers sample.

2.1.4. Sample Alignment

Before the measurement, the multilayer sample is carefully positioned at the center of the X-ray beam and is oriented at $\omega = 0°$ and $\theta = 0°$. To do so, a 2θ scan is first performed to center the position of the detector at $\theta = 0°$. Then the sample chamber is mounted on the goniometer and another 2θ scan is performed to adjust the depth of the sample to block nearly half of the X-ray incident beam. The ω scan is then performed to adjust the angle of the sample roughly to $\omega = 0°$. Since the ω scan and 2θ scan affect the results with each other, these scans need to be performed more than one time to ensure the quality of the alignment. A two-dimensional ω-2θ scan around the second or the third Bragg peak is used to fine-tune the alignment of the ω-angle. The position of ω-angle is adjusted so that the peak position of the two-dimensional ω-2θ scan is at (ω-angle) = (1/2) (2θ-angle). Fig. 2-5 shows the representative results of scans for sample alignment.

Once the sample was properly positioned and aligned, ω-2θ scans are performed from $\omega = 0.5°$ to $\omega = 7.5°$ with a step size of $\Delta\omega = 0.01°$. During the experiment, the samples were housed in a temperature-humidity chamber in which the hydration level of the sample was controlled by the relative humidity (RH) of water vapor. An attenuator is used to prevent the first-order Bragg peak from saturating the detector. The scan is repeated 3–5 times for each hydration level and then averaged for data analysis. To use the swelling method for the determination of the phases of diffraction amplitudes, each sample was scanned at several different hydration levels.

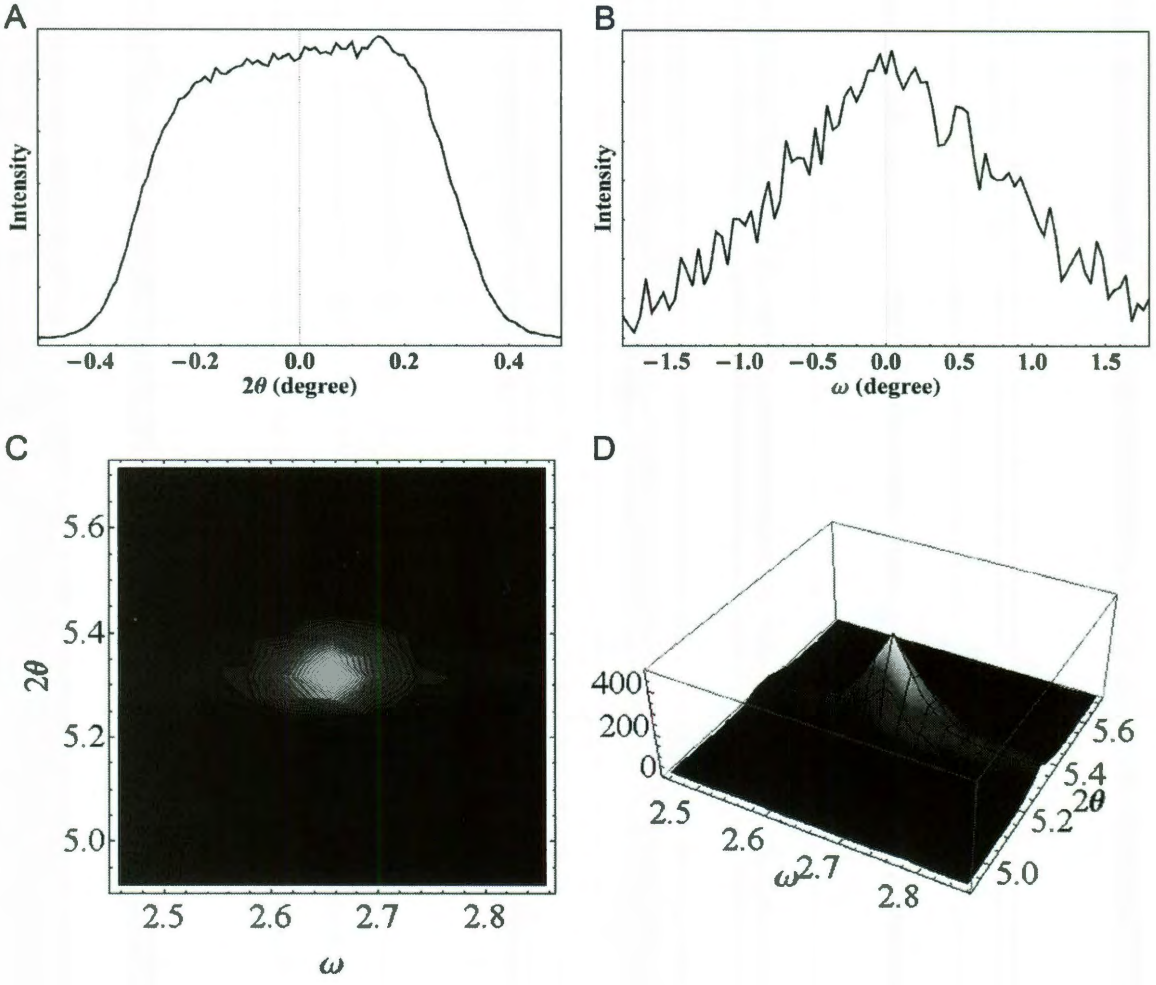

Figure 2-5 X-ray lamellar diffraction scans for the sample alignment. (A) The plot of the 2θ scan which is performed to center the detector position relative to the incident beam of X-ray. (B) The plot of the ω scan, which is performed to coarse-tune the orientation of the substrate. For a substrate roughly oriented paraell to the incident beam, a symmetry result centered at ω=0 should be obtained. (C) The contour plot of the two-dimensional ω-2θ scan. This two-dimensional scan was used to fine-tune the orientation of the substrate so that the substract can be perfectly oriented paraell to the incident beam. (D) The three-dimensional plot of the ω-2θ scan. The sharp peak was resulted from the diffraction signals on a well-aligned multilayer sample.

2.1.5. Data Reduction

In order to reconstruct the correct electron density profiles, the measured diffraction amplitudes $I_m$need to be corrected for artifacts and distortions introduced by the experimental setup and geometry. Considering all the artifacts and distortions of the system, the corrected intensity I_c can be written as:

$$I_c =< (I_m C_{det}\, C_{att} - bg)\; C_{sam}\, C_{abs}\, C_{pol} > C_{Lor}$$

where (1) C_{det}: the correction for the detector dead-time. (2) C_{att}: the correction for the attenuator. (3) bg: the background of diffraction signal. (4) C_{sam}: the correction for the geometry of sample. (5) C_{abs}: the correction for the sample absorption. (6) C_{pol}: the correction for polarization. (7) C_{Lor}: the correction for Lorentz factor.

The measured diffraction intensity was first corrected for the attenuator absorption and for the detector's dead-time factor. After removing the background, data was corrected for sample absorption and diffraction volume. The integrated peak intensities were then corrected for the polarization and the Lorentz factors. The relative magnitude of the diffraction amplitude was the square-root of the integrated intensity. The phases were determined by the swelling method. With their phases determined, the diffraction amplitudes can be used to reconstruct the electron density profile of the bilayer.

2.2. Neutron In-plane Scattering

2.2.1. Background

Neutron in-plane scattering is a very useful tool to detect the lateral distribution of channels on the lipid membranes. The principal of neutron in-plane scattering is basically the same as that of X-ray in-plane scattering. X-ray scattering amplitudes are proportional to the atomic number of atoms which incident X-ray beam interacts with. Therefore, the detail information of lipid structure can be further investigated by adding heavy atoms (for example, bromine) on the lipid chains. Neutron scattering amplitudes, on the other hand, are determined by the nuclear property of atoms. A particular advantage of neutron scattering is the possibility of exchanging H_2O with D_2O without altering the molecular configuration of the sample. This technique makes use of the large contrast between the scattering by hydrogen and by deuterium since the scattering lengths of hydrogen and deuterium are very different. Therefore, if water is a part of the scattering object, as in the case of a membrane pore making by antimicrobial peptides, the scattering amplitude can be enhanced by changing H_2O with D_2O without changing the molecular configuration of the pore.

In-plane scattering experiment in both neutron and X-ray case was performed in the transmission mode as shown in Fig. 2-6. The incident beam with the direction $\hat{\boldsymbol{s}}_0$ and an angle θ with respect to the normal plane of the substrate was directed into the sample, and the scattered beam with the direction $\hat{\boldsymbol{s}}$ was detected

on the other side of the sample. If the scattered beam is at an angle θ with respect to the normal plane of the substrate, the vector $\hat{\boldsymbol{s}} - \hat{\boldsymbol{s}}_0$, or the momentum transfer vector $\boldsymbol{q} = (2\pi/\lambda)(\hat{\boldsymbol{s}} - \hat{\boldsymbol{s}}_0)$, is parallel to the plane of the substrate. The in-plane scattering can be carried out by two different ways: (1) θ-2θ scan can be performed by incremental θ, and (2) 0-2θ scan can be performed by a normal incident beam. The scattering curves of θ-2θ and 0-2θ are essentially the same. In the θ-2θ scan, the momentum transfer vector $\boldsymbol{q}$ is exactly parallel to the plane of the substrate. In the 0-2θ scan, the momentum transfer is slightly off the plane of the substrate. However, the normalized magnitude of the component parallel to the plane of the substrate is $q_{||}/|\boldsymbol{q}| = cos\theta > 0.966$, if $\theta < 15°$. Therefore, the results of the θ-2θ scan and 0-2θ scan are practically the same in small angles.

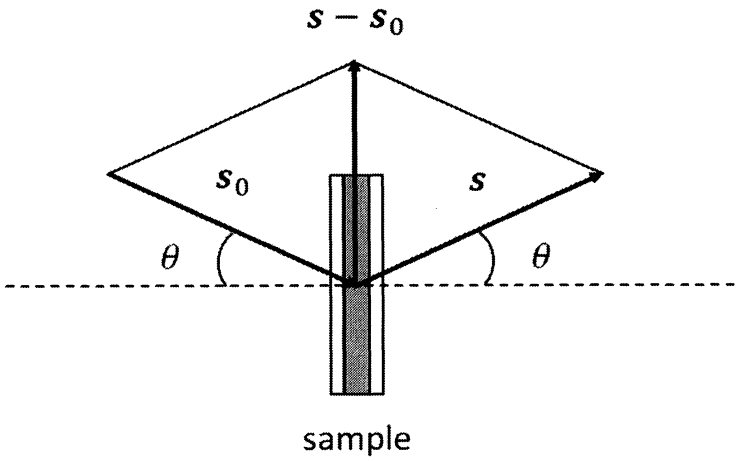

Figure 2-6 Schematic of in-plane scattering experimental setup. The directions of incident and scattered beam are the unit vector s_0 and s, respectively. The momentum transfer $q=(2\pi/\lambda)(s-s_0)$ is parallel to the plane of the substrate.

2.2.2. Sample Preparation

For neutron experiments which required a large amount of sample (~30 mg of lipid), stacked membranes were sandwiched between two cleaned quartz plates. Lipid and peptide of desired peptide-to-lipid molar ratio (P/L) were first co-dissolving in organic solvent (1:1 (v/v) chloroform and tetrafluoroethylene (TFE)) in a glass vial. The solvent was removed by a gentle nitrogen gas flow and the sample glass vial was then put under vacuum overnight. After organic solvent was completely removed, 4ml of water was added to the peptide/lipid mixture. The suspension was vortexed and sonicated for 1 hour to break up large aggregates of lipids and peptides. The sample then went through the lyophilization process (also known as freeze-drying). This dehydration process works by freezing the material and then reducing the surrounding pressure to allow the frozen water in the material to sublimate directly from the solid phase to the gas phase. The remaining lyophilized powder in the glass vial was hydrated by 100% relative humidity (RH) water vapor overnight to a gel-like texture at ~35°C. The gel-like mixture was spread on one quartz plate and then covered by a second plate. The sandwiched sample with the desired experimental condition was then sealed in an aluminum sample holder with two quartz windows that provided a beam path of 16 mm in diameter. Double substrates have proven to be capable of aligning thick lipid multilayers [23]. The membrane alignment in a sandwiched sample can be examined by polarized microscopy [23, 24] or neutron diffraction.

2.2.3. Experiment of Neutron In-plane Scattering

Neutron experiment was performed at the HFIR Bio-SANS CG-3 station [25] in the Oak Ridge National Laboratory. The small angle scattering beamline was equipped with a 1 x 1 m area detector (5.1 x 5.1 mm^2 pixels) with adjustable sample to detector distance 1-15 m. The neutron wavelength was 6 Å with $\Delta\lambda/\lambda \sim 15\%$. The detector was positioned to record the q range from 0.013 to 0.3 $Å^{-1}$. Sandwiched samples were sealed in an aluminum holder that provided a beam path of 16 mm in diameter. The neutron in-plane scattering data (one example is shown in Fig. 2-7) were collected for 10-30 minutes per sample at room temperature by a LabVIEW program and analyzed by Mathematica.

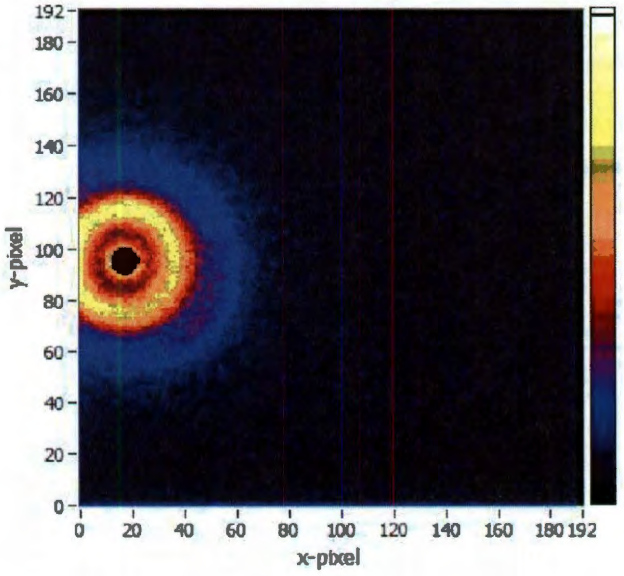

Figure 2-7 The raw data of the neutron in-plane scattering obtaining from the sample of LL-37/DOPC at P/L=1/50.

2.2.4. Data Analysis

The neutron in-plane scattering data can be interpreted by a channel model originally proposed by Baumann and Mueller in 1974. The inserted peptides at concentration above critical peptide-to-lipid ratio formed cylindrical channels on the lipid membrane. Each channel was made of several peptides helices which surrounded a cylindrical water pore. By exchanging H_2O with D_2O in the water pore, neutron in-plane scattering can be used to detect the lateral distribution of channels on membranes. The neutron scattering intensity $I(q)$ can be written as

$$I(q) = N|F(q)|^2 S(q) \tag{2-18}$$

where N is the total number of channels. F(q), the form factor, is the scattering amplitude by an individual channel. S(q) is the structure factor. The form factor of an individual channel is given by

$$F(q) = \int_p [\rho_p(\boldsymbol{r}) - \rho_l(\boldsymbol{r})] \exp[i\boldsymbol{q} \cdot (\boldsymbol{r} - \boldsymbol{r}_a)] \, dV(\boldsymbol{r}) \tag{2-19}$$

where $\rho_p(\boldsymbol{r})$ is the scattering density of the peptide molecules, $\rho_l(\boldsymbol{r})$ is the scattering density of the lipid molecules, $\boldsymbol{r}_a$ is the position of the channel axis and the integration is over the space occupied by the peptides. The peptides are assumed to be cylindrically symmetric with respect to the channel axis in the z direction which is perpendicular to the plane of the membrane or substrate. The form factor can be further rewritten as

$$F(q) = \int_0^r \rho_{pore}(\boldsymbol{r}) \exp[i\boldsymbol{q} \cdot (\boldsymbol{r} - \boldsymbol{r}_a)]\, d^3r + \int_r^R \rho_{peptide}(\boldsymbol{r}) \exp[i\boldsymbol{q} \cdot (\boldsymbol{r} - \boldsymbol{r}_a)]\, d^3r$$

(2-20)

Each channel has two distinct regions: a water pore of radius r and a peptide ring of outside radius R. ρ_{pore} and $\rho_{peptide}$ are the scattering length density contrast of pore region and peptide ring region relative to the lipid background, respectively. For $q \ll 2\pi/d$ (d is the in-pane molecular dimension), the molecules are considered uniformly distributed in each region. The lipid background is also considered as a uniform region. With these approximations, Eq. (2-20) can be integrated as

$$F(q) = 2\rho_{pore}V_{pore}\frac{J_1(qr)}{qr} + 2\rho_{ring}V_{ring}\frac{RJ_1(qR) - rJ_1(qr)}{q(R^2 - r^2)}$$

(2-21)

where $V_{pore}$and V_{ring} are the volumes of the pore region and ring region, respectively.

S(q) is the structure factor, and defined as

$$S(q) = \frac{1}{N} < |\sum_j \exp(-iq \cdot r_j)|^2 > = 1 + 2\pi \int_0^\infty (pcf(r) - 1) r J_0(qr) dr$$

(2-22)

where r_j is the position of the center of the jth channel, $pcf(r)$ is the pair correlation function which is related to the probability of finding the centers of particles at a given distance from the center of a chosen particle, and $J_0(qr)$ is the 0th order Bessel function of qr.

2.2.5. Computer simulation

The structure factor was computed by computer simulations with the Monte Carlo method. 961 channels (31 channels of radius r on each side) were first positioned regularly in a square plane of side L. The channels were allowed to move randomly in the square plane with the constraint that no two channels were allowed to overlap. The periodic boundary condition was applied to the system to make simulations with limited number of channels closer to the reality. Each Monte Carlo step first randomly chose one channel and then randomly moved it to a new position. If the new position of the chosen channel was not overlap with other channels, this Monte Carlo step was a successful step; otherwise, it was rejected. The regular positioned channels were first performed 1 million successful Monte Carlo steps to make channels distributed randomly in the square plane. After every 100 thousand successful steps, the positions of all channels were used to calculate the structure factor from Eq. (2-22). To get a smooth curve of the structure factor, 100 thousand calculated structure factors were average for further data analysis.

The simulated structure factor can be adjusted by two parameters: (1) the radius of the channels and (2) the number density of channel in the square plane. Because the number of channels is a constant, the second parameter is now the length of the square plane. The positions of peaks are determined by the radius of the channels due to non-overlapping between channels. The intensities of the peaks are determined by density of channels in the square plane shown in Fig. 2-8. The scattering peaks can be easily observed at high area density.

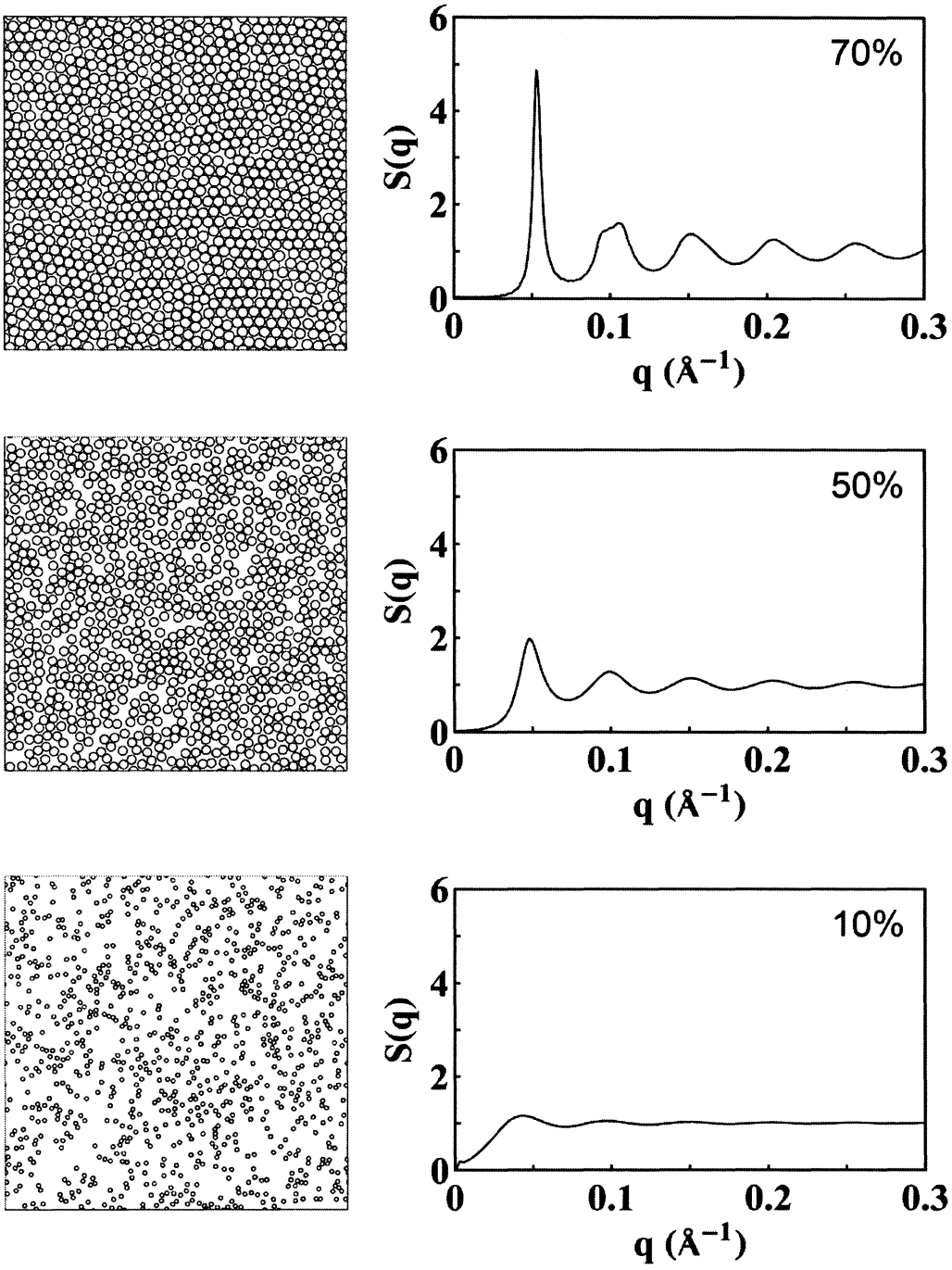

Figure 2-8 Computer simulation of structure factor at different area density (defined as total area of all channels divided by area of the square).

2.3. Circular Dichroism and Oriented Circular Dichroism

2.3.1. Circular Dichroism

Circular Dichroism (CD) is a technique widely used to investigate the secondary structures of proteins and peptides. It measures the absorption differential between left-handed circularly polarized light and right-handed circularly polarized light which arise due to structural asymmetry. The absence of regular structure in protein and peptides results in zero CD intensity, while an ordered structure results in a spectrum containing both positive and negative signals. Secondary structure of proteins and peptides is determined by CD spectrum in the far-UV spectral region (190-250 nm). The structure of α-helix, β-sheet, and random coil each has its own characteristic CD spectrum shown in Fig. 2-9. Although CD cannot detect the location of the α-helix within the molecules or completely predict how many they are, it is still a valuable tool for showing the conformation changes of proteins or peptides. Anyone studying proteins or peptides will find CD a very useful and valuable tool for verifying that the protein is in the correct conformation before performing extensive experiments with it.

Experimentally circular dichroism spectrum of proteins and peptides is measured in solution. The sample solution is contained in a cuvette made of fused quartz which is transparent to the light in the far-UV spectral region. The solvent is usually water, but can also be any other organic solvents (e.g., ethanol, methanol, trifluoroethanol (TFE)) in which the protein or peptide dissolves. Often the solvent

dependence of the secondary structure can provide some important insight on the folding pathways of proteins and peptides when interact with lipid membrane. For membrane active peptide studied in the lab, a suspension of lipid vesicles in water or some membrane mimicking environments (for example, tetrafluoroethylene (TFE)) is often used to measure the CD spectrum.

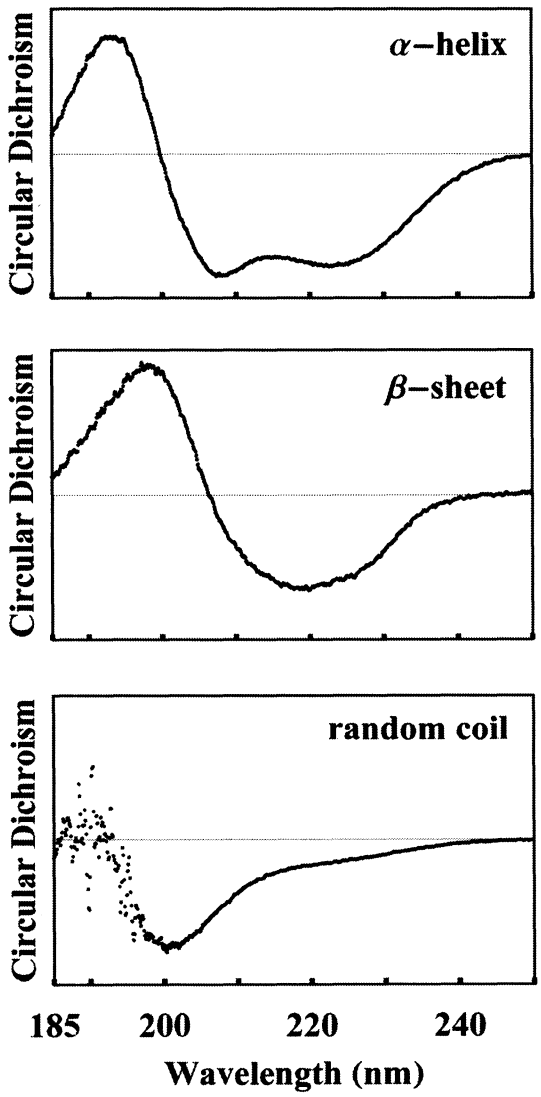

Figure 2-9 Characteristic CD spectra for the different secondary structures: α-helix, β-sheet and random coil.

2.3.2. Oriented Circular Dichroism

The technique of oriented circular dichroism (OCD), developed by Wu et al. [6] in our lab in 1990, is an technique modified from solution circular dichroism for measuring orientation of membrane active peptides. The technical details of OCD can be found in previous study [6]. For practical purpose, one recognizes the CD of helices in solution by a positive ~190 nm peak, a negative ~208 nm peak and a negative ~224 nm peak. The OCD of a helix perpendicular to the incident light (parallel to the plane of the membrane), called surface spectrum, is similar to the solution CD except with a stronger negative 208 nm peak. In comparison with the solution helical CD, the OCD of a helix parallel to the incident light (normal to the plane of the membrane), call insertion spectrum, has the positive peak red-shifted, no peak at 208 nm and a smaller 224 nm negative peak; as a result the zero crossing point between the positive and negative peaks is also red shifted. The vanishing of the negative peak at ~208 nm has a theoretical basis, i.e., the Moffitt theory [26] and is the most prominent feature for a helix oriented in the direction of light (normal to the membrane).

The two oriented spectra were experimentally verified by several α-helical antimicrobial peptides, like alamethicin [27], magainin [28], melittin [29] and LL-37 [30]. Fig. 2-10 shows two basis spectra (surface spectrum and insertion spectrum) as measured for LL-37 in the DOPC lipid together with the proposed peptides orientation in the well-aligned lipid bilayer.

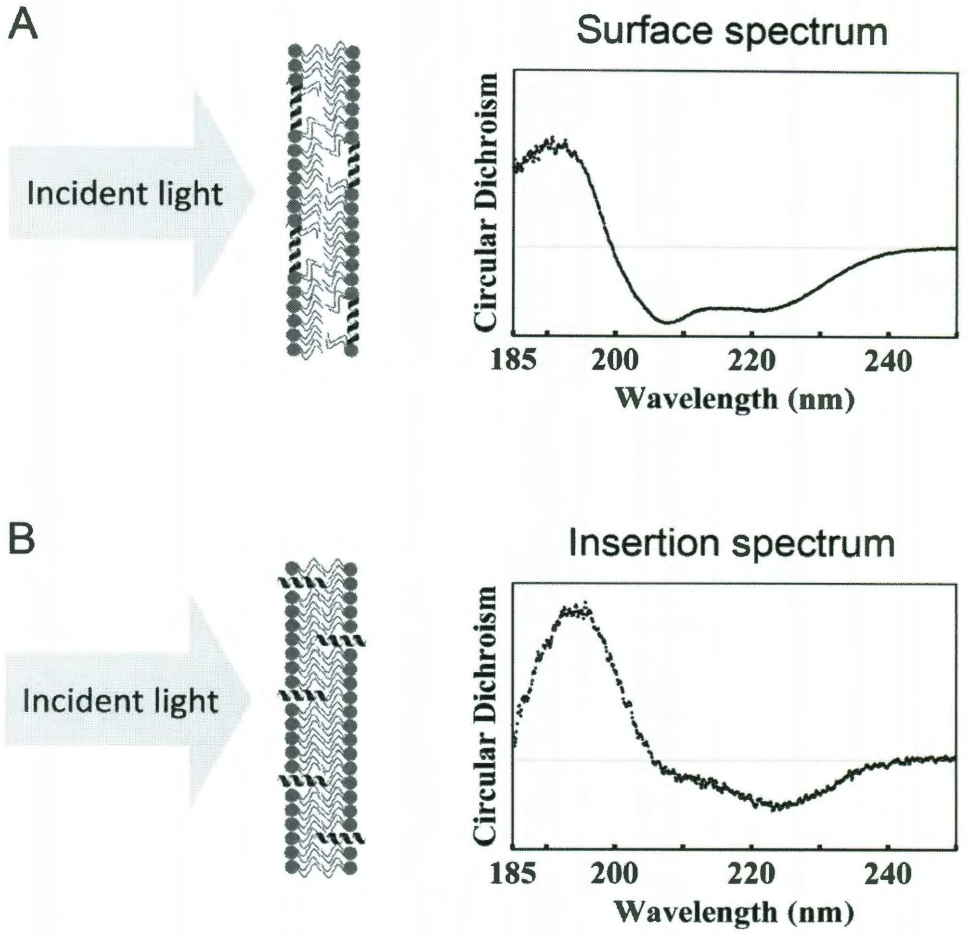

Figure 2-10 Basis OCD spectra of LL-37 in lipid bilayers. (A) Helix axis parallel to the plane of the membrane and its corresponding OCD spectrum is called surface spectrum. (B) Helix axis perpendicular to the plane of the membrane and its corresponding OCD spectrum is call insertion spectum.

2.3.3. Experimental Setup

The sample used in the OCD experiment is basically the same as that of X-ray experiment. Only a silicon substrate of the sample is replaced by a 1cm×1cm quartz substrate, which is transparent to far-UV spectral region. Since lipids could absorb the polarized light and increase the noise significantly in far-UV spectral region, lipid amount on a single substrate is controlled around 0.3mg per substrate. The background spectrum for each OCD sample is the spectrum for the same amount of lipid on the quartz substrate. The OCD spectrum of peptides shown in each figure is the sample spectrum minus the background spectrum.

Spectra were measured in a Jasco (Tokyo, Japan) J-810 Spectropolarimeter. The linearly polarized monochromatic light comes out from a xenon lamp. A photoelastic modulator is used to modulate the polarization of the incoming linearly polarized light source. Modulated right-handed and left-handed components go through the optically active sample and result in preferential absorption of right-handed or left-handed polarization. The photomultiplier is then used to accumulate signals for a specific wavelength in the far-UV spectral region. The prepared sample is mounted in the home-made chamber, where relative humidity (RH) and temperature can be controlled by the computer program. To reach the equilibrium condition, the sample was measured after 5-10 minutes once the hydrated level was changed. The measurement is repeated 2-5 times for each condition and then average for further data analysis. The detail experimental setup of our modified spectropolarimeter is shown in Fig. 2-11.

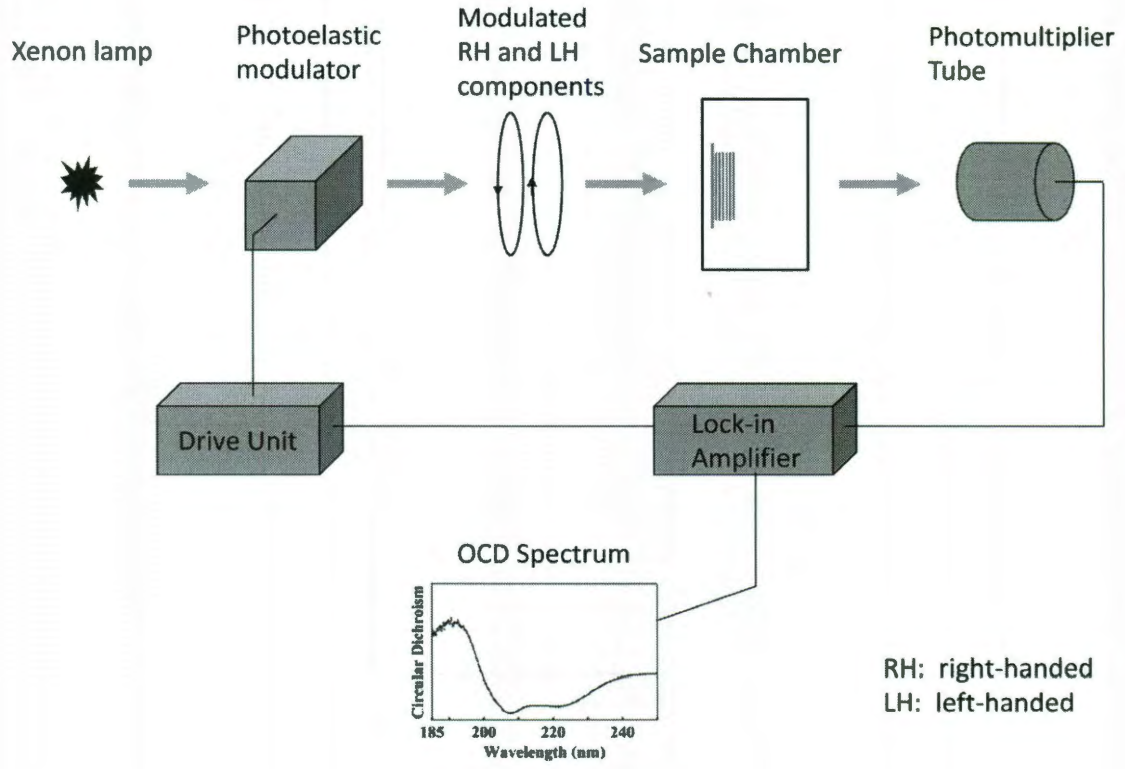

Figure 2-11 Schematic of OCD experimental setup. Sample substrate is mounted vertically onto the RH-temperature controlled sample chamber.

2.4. Micropipette Aspiration System

2.4.1. Background

The micropipette aspiration system is a unique technique to the study physical properties of a lipid vesicle aspirated by a glass micropipette. This method was originally developed by Evan Evans and his collaborators in the 1980s to measure the elastic moduli of lipid bilayers [31, 32], the Van der Waals force [33], and the adhesion energy [34, 35] between two lipid vesicles. In our membrane biophysics laboratory, we adopted and modified this method to study the dynamic interaction processes between amphipathic molecules and lipid membrane vesicle. We also apply the system to investigate the membrane-membrane interactions and develop a theory for measuring its corresponding energy.[36]

Lipid vesicles self-assemble when phospholipids are hydrated in water solution. They can be prepared by many different methods, such as sonication, extrusion, and electroformation, resulting in a great variety of sizes from tens of nanometers to hundreds of micrometers. Small unilamellar vesicles (SUVs), which have the smallest diameter around 30-50 nm, can be prepared by sonication method. Large unilamellar vesicles (LUVs), produced by extrusion method, are 80-800 nm in diameter while giant unilamellar vesicles (GUVs), produced by eletroformation, range from 1-100 μm in diameter. In our study, we use GUVs as a model system to mimic cell membranes since they are similar in size. GUVs are distinguished from SUVs and LUVs because their size is large enough to be directly

observed under microscope. As a result, a variety of experiments can be performed at the level of a single GUV.

Many vesicle experiments have been carried out by the use of a suspension solution containing LUVs or SUVs using fluorescence spectroscopy, light scattering and X-ray diffraction. What has been measured in these vesicle experiments is the average behavior of a large number of vesicles, while the behavior of the individual vesicle cannot be observed. In contrast, the study of a single GUV allows us to get the information on the structure and physical properties of individual vesicle in real time under microscope. By using the micropipette aspiration system, the experiments with aspirated single GUV provide us further insights into the dynamic process of the peptide/lipid interactions.

2.4.2. Sample Preparation

Giant unilamellar vesicles (GUVs) were produced by the electroformation method [37]. Lipid and 0.5% molar ratio of a headgroup-fluorescent lipid (1,2-dioleoyl-sn-glycero-3-phosphoethanolamine-N-(Lissamine Rhodamine B Sulfonyl) (Rh-DOPE)) were co-dissolving in organic solvent (1:1 (v/v) chloroform and tetrafluoroethylene (TFE)). A small amount of fluorescent lipids were added to enhance the contrast of the GUV boundary when observing the GUV under fluorescent microscope (Fig. 2-12). The lipid solution was then deposited onto two ITO coated glass cover slips (~0.03 mg of lipid on each glass cover slip). Two ITO glass cover slips were kept under vacuum for 1-2 hours to remove the remaining organic solvents. After vacuum, an o-ring was sandwiched between two ITO slips

and the gap in between was filled with 200 mM sucrose solution. 1.2 V AC at 10 Hz was applied between the two ITO electrodes for 1 hour. Subsequently the frequency was adjusted to 5 Hz for 40 minutes and followed by 1 Hz for 20 minutes. This electroformation method has been shown to produce unilamellar vesicles [37]. The vesicle suspension was then gently collected in a glass. The vesicles were used for experiment within 24 hours of production.

Micropipettes, for aspirating a single GUV, were made by a micropipette puller P-97 made from Sutter Instrument Company (Novato, CA) and refined by a Narishige (East Meadow, NY) microforge, MF-900. Micropipettes and the glass surfaces of experimental chambers were coated with 1% bovine serum albumin (BSA) for few hours in order to neutralize the charge on the bare glass surface and then washed extensively with water.

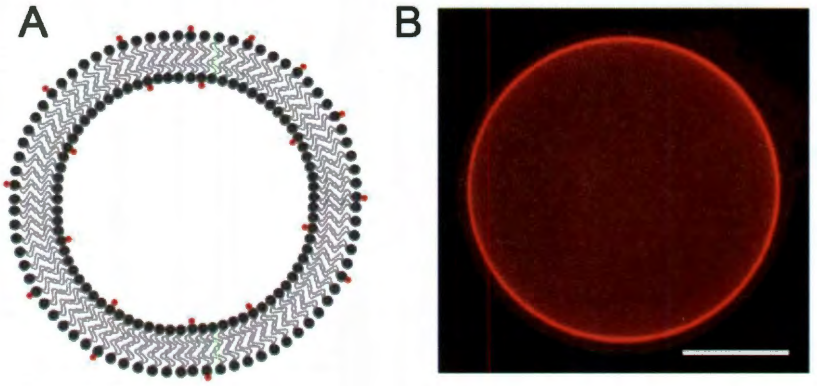

Figure 2-12 (A) Schematic of giant unilamellar vesicle (GUV). Rhodamine B (in red color) was attached on the head group of DOPE. (B) Fluorescent image of a single GUV (Scale bar=20μm).

2.4.3. Experimental Setup

A small amount of vesicles were first transferred to a control chamber. The solution in the control chamber contains 190 mM glucose solution and 10 mM buffer solution, which is used to maintain pH value of the solution. The osmolality of every solution used in the GUV experiment was measured by a Wescor (Logan, UT) dew-point Osmometer model 5520. The single GUV aspiration experiment was performed by transferring an aspirated GUV from a control chamber to an observation chamber containing peptide/glucose/buffer solution (Fig. 2-13). The observation chamber was placed side by side with the control chamber, separated by ~0.5 cm. The osmolality of the solution in the control chamber was the same as 200 mM sucrose solution inside the GUVs. The GUVs settled at the bottom due to the density differential inside and outside of GUVs. A micropipette (inner diameter 10-15 μm) was used to picked and hold a chosen GUV (40-60 μm in diameter) by aspiration at a constant negative pressure (~100 Pa producing a membrane tension ~0.5 mN/m). A transfer pipette (inner diameter 0.75mm), filled with the control solution, was inserted from the opposite side of the aspiration pipette through the observation chamber into the control chamber. The aspiration micropipette and the transfer pipette were held separately by Narishige (East Meadow, NY) motor-driven micromanipulators MM-188NE. The aspirated GUV was inserted into the transfer pipette in the control chamber. By moving the microscope stage, the aspirated GUV in the transfer pipette was moved from the control chamber to the observation chamber. Then the transfer pipette was swiftly moved away, so that the GUV was

exposed to the peptide/glucose/buffer solution (marked as t=0). The video of the process was captured by a CCD camera.

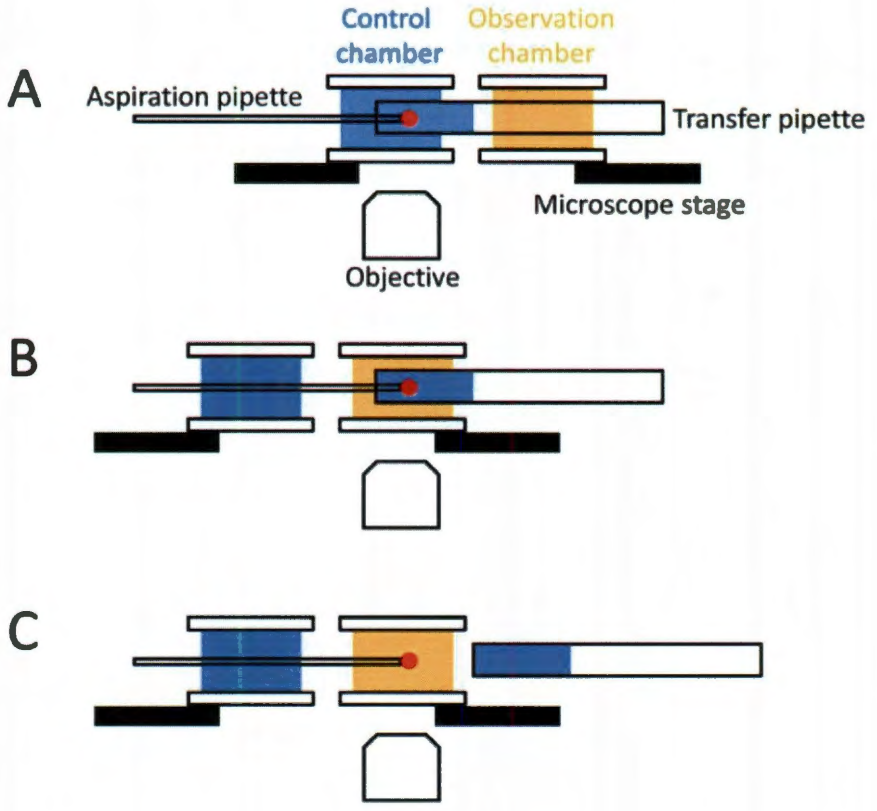

Figure 2-13 Schematic of the GUV experiment. (A) An aspirated GUV was positioned into the transfer pipette in the control chamber. (B) The aspirated GUV in the transfer pipette was moved from the control chamber to the observation chamber by moving the microscope stage. (C) The transfer pipette was moved away, and the aspirated GUV was exposed to the solution in observation chamber.

2.4.4. Data Analysis

A single aspirated GUV consisted of two parts: a spherical vesicle (radius R_v) outside the tip of the micropipette (radius R_p) and a cylindrical protrusion (length L) inside the micropipette (Fig. 2-14). By maintaining a constant sucking pressure inside the aspiration micropipette, the protrusion length would change if there was a change in the surface area A or in the volume V of the GUV. From the geometry of an aspirated GUV (Fig. 2-14), the change of the surface area ΔA is related to the change of the protrusion length (ΔL) and the change of the GUV radius (ΔR_v) by

$$\Delta A = 8\pi R_v \Delta R_v + 2\pi R_p \Delta L \tag{2-23}$$

and the change of the volume ΔV is related to ΔR_v and ΔL by

$$\Delta V = 4\pi R_v^2 \Delta R_v + \pi R_p^2 \Delta L \tag{2-24}$$

When the solutions inside and outside the GUV were isotonic (the same osmotic pressure), the change of the volume should be zero due to no water influx and efflux. Under such a condition ($\Delta V = 0$), the change of the surface area can be directly related to the change of the protrusion length by

$$\Delta A = 2\pi R_p\left(1 - R_p/R_v\right)\Delta L \tag{2-25}$$

Chapter 3

Membrane-mediated Peptide Conformation Change from α-Momomers to β-Aggregates

3.1. Introduction

The major component of Alzheimer's disease amyloid plaque, β-amyloid protein 1-40 (Aβ 1-40) [38] and the peptide penetratin [39] exhibited the same membrane mediated conformation changes. Both peptides are random coils in solution but change to α-helical or β-like conformations in the presence of negatively charged lipid membranes. Both peptides change from α to β conformations as the lipid charge increases or as the peptide concentration increases [9-14]. Since the principle behind these phenomena might clarify the molecular mechanism of β-amyloid formation, we investigated the correlation between the peptide conformation of penetratin and its effect on the membrane

thickness in four different lipids with various degrees of chain unsaturation. The results revealed a new effect of membranes on penetratin, i.e., the degree of chain unsaturation influences the peptide conformation. We found that penetratin in the helical conformation was bound to the interface and thinned the membrane. In contrast, penetratin in the β-conformation had little effect on the bilayer thickness; therefore it was most likely not embedded in lipid bilayers. From the systematic results we were able to deduce the molecular mechanism in terms of free energies that explains the effect of membrane binding on the secondary structure of penetratin. The mechanism could be the prototype for the membrane-mediated version of nucleation-dependent amyloid formation proposed by Jarrett and Lansbury (J & L) [38]. It might explain why membrane binding has been suspected as the catalyst for polymerization leading to amyloid formation [38, 40-43].

β-amyloid formation appears to be a generic process for a large number of diverse proteins and peptides [43, 44]. For this study we chose penetratin since small peptides are more likely to produce precise quantitative measurements than larger proteins. Penetratin is a 16-residue peptide corresponding to the third helix of the Antennapedia homeodomian of Drosophila [45]. This peptide has been studied as a cell-penetrating peptide but its purported membrane-penetrating mechanism remains controversial [46-48]. We do not address the question of cell penetration here. Rather we investigated how penetratin interacts with lipid bilayers. We believe that this is the first step toward understanding how penetratin was internalized into cells or vesicles as reported [46, 47].

Penetratin is similar to antimicrobial peptides (AMPs) [49] in that both are water soluble and spontaneously bind to membranes; however, unlike AMPs, penetratin does not form pores in the membranes [50-52]. There is a long history of studying the interactions between lipid bilayers and amphipathic molecules, such as AMPs [22, 49, 53, 54] and drugs [7, 55-57]. Despite the diversity of these molecules, their interactions with lipid bilayers were all characterized by strong concentration dependence. In particular, AMPs exhibited two distinct phases [22, 58]: at low peptide/lipid ratios the peptides did not form pores, but at high ratios they did. We found that this concentration dependence was due to a combination of two effects, a critical micellar transition [7] from a monomeric binding phase to an oligomeric pore-forming phase and a membrane thinning effect that made the energy level of the monomeric phase increase with the bound-molecule/lipid ratio [58]. What distinguishes penetratin from the other amphipathic molecules is that it forms β-aggregates in the second phase. Nevertheless we found important similarities between penetratin and AMPs in their interaction with lipid bilayers.

In solution penetratin is a random coil according to its circular dichroism (CD) spectrum [11-13]. In the presence of negatively charged vesicles, the CD spectra varied with the molar fraction of the charged lipids in the vesicles. At low fractions of charged lipids the spectra were α helical, but at high fractions the spectra were β-like. In between, the spectra were continuous mixtures of the two [11-13]. In the literature the β-like CD was often attributed to a β-sheet structure [9, 10]. Su et al. [59] called the corresponding conformation a "turn-rich structure"

based on their NMR analysis. The same α to β transition was observed if the lipid vesicles were held constant but the penetratin concentration was increased from low to high.

Beschiaschvili and Seelig [60] were the first to have shown that the binding of charged amphipathic peptides to oppositely charged lipid vesicles involved two kinetic equilibria. The positively charged peptides are attracted to the proximity of the negatively charged lipid headgroups according to the Poisson-Boltzmann distribution, known as the Gouy-Chapman theory [60]. The peptides are subsequently bound to the lipid interface by the hydrophobic effect. If the partition coefficients (called the surface partition constant) are measured between the bound peptides and the peptide concentration in the vicinity of the charged vesicles, the values are quite independent of the lipid charge. (The apparent partition coefficients relative to the average bulk concentrations are three to five orders of magnitude larger than the surface partition constants [52, 61]; however the former are not constant of concentration, whereas the latter are.) In fact, after removing the electrostatic effect, the surface partition constants to charged lipids are very close to the partition constants to neutral lipids [60, 61]. Very careful measurements of penetratin binding to lipid vesicles performed by Persson et al [52] revealed the same phenomenon. Excluding the effect of electrostatic attraction, the surface partition constants of penetratin to lipid bilayers are essentially independent of the PC/PG ratios, indicating that the hydrophobic interactions are independent of the charged headgroups of the lipids. Thus the effect of lipid charge

is to accumulate penetratin to the vesicles' vicinity. The apparent effect of anionic lipid charge on the conformation of penetration [12, 13, 62] was essentially due to the effect of increasing peptide binding to the bilayers. The effect of increasing anionic lipid charge was the same as the effect of increasing peptide concentration. There is no independent effect of lipid charge on peptide conformation.

This leaves the main question about the peptide's β-formation to its concentration dependence. To understand how increasing the peptide concentration promotes the β-formation in the presence of lipid bilayers, we sought correlations between the peptide conformation and its effect on the membrane thickness. Previously we have found in other examples that membrane thinning played an important role in peptide-membrane interactions [22, 55, 57, 58].

3.2. Materials and Methods

3.2.1. Materials

1,2-dimyristoyl-sn-glycero-3-phosphocholine (DMPC), 1-stearoyl-2-oleoyl-sn-glycero-3-phosphocholine (SOPC), 1-oleoyl-2-myristoyl-sn-glycero-3-phosphocholine (OMPC), and 1,2-dioleoyl-sn-glycero-3-phosphocholine (DOPC), 1,2-di-(9Z-octadecenoyl)-sn-glycero-3-phospho-(1'-rac-glycerol) (DOPG) and 1,2-dioleoyl-sn-glycero-3-phosphoethanolamine-N-(Lissamine Rhodamine B Sulfonyl) (Rh-DOPE) were purchased from Avanti Polar Lipids (Alabaster, AL). Penetratin (RQIKI WFQNR RMKWK K) was synthesized by GenScript Corp (Piscataway, NJ) to

>95% purity. All chemicals were purchased from Sigma-Aldrich (St. Louis, MO) and were used without further purification.

Penetratin was first dissolved in tetrafluoroethylene (TFE). Appropriate amounts of penetratin and lipid of chosen peptide/lipid molar ratio, P/L, were mixed in 1:1 (v/v) chloroform and TFE, and deposited on a thoroughly cleaned flat substrate (for X-ray, 0.3mg of lipid on $1cm^2$ of silicon wafer; for CD, 0.02mg of peptide on $1cm^2$ quartz plate for high P/Ls, 0.2 mg of lipid on $1cm^2$ for low P/Ls). After the solvent was removed in vacuum, the samples were hydrated by saturated water vapor at 35°C overnight [63]. The results were well aligned parallel hydrated bilayers as proven by X-ray diffraction. The samples were kept in a temperature-humidity chamber during the measurement. The experiments of DMPC were performed at 33°C, and the other lipids at 25°C to ensure that all lipid-peptide bilayers were in the fluid lamellar phase [64].

3.2.2. X-ray Lamellar Diffraction

ω-2θ diffraction was collected on an Enraf Nonius Diffractis 581 and a Huber (Huber Diffraktionstechnik, Rimsting, Germany) four-circle goniometer, with a line-focused Cu Kα source (λ = 1.542 Å) operating at 40 kV and 15-30 mA. The incident beam was collimated by a horizontal soller slit and two vertical slits on the front and the back sides of the soller slit. The horizontal and vertical divergence of the incident beam were 0.23° and 0.3°, respectively. The diffracted beam first passed through a vertical slit and then was discriminated by a bent graphite

monochromator before entering a scintillation detector, which was biased to discriminate against higher harmonics and fluorescence. This diffractometer was designed to minimize the background signal, which in turn allowed the measurement of high diffraction orders.

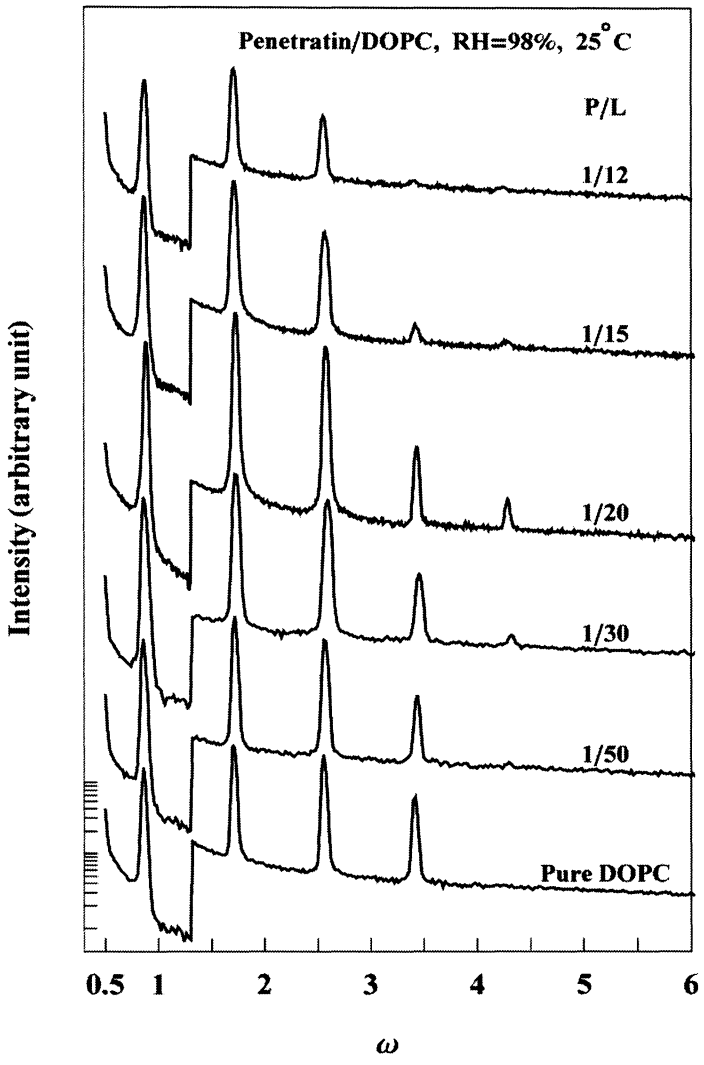

Figure 3-1 Representative diffraction patterns: series of patterns for DOPC containing penetratin in different P/L, displaced vertically for clarity.

Before the measurement, the aligned multilayer sample was carefully positioned at the center of the X-ray beam and was oriented so that $\omega = 0°$ and $\theta = 0°$ coincided. We have established an elaborate routine for positioning and orienting the sample as described in Wu et al. [65]. A two-dimensional ω-θ around the second or the third Bragg order was used to check the alignment of the ω-angle and the mosaic of the multilayers alignment. Typically the FWHM (full width half maximum) of the peak on the ω axis (of the ω-θ scan) was 0.2°-0.3° (example in [66]). Once the sample was properly positioned and aligned on the diffractometer, each ω-2θ scan was performed from $\omega = 0.5°$ to $\omega = 6°$ with a step size of $\Delta\omega = 0.01°$. An attenuator was used to prevent the first-order Bragg peak from saturating the detector. The scan was repeated 3–5 times for each hydration level and then averaged for data analysis. To use the swelling method [67] for the determination of the phases of diffraction amplitudes, each sample was scanned at several different hydration levels between 88% and 98% relative humidity (RH). Representative diffraction patterns at 98% RH are shown in Fig. 3-1.

The procedure of data reduction was described in many of our previous works [64, 68]. Briefly, the measured diffraction intensity was first corrected by the attenuator absorption and the detector's dead-time factor. After removing the background, data were corrected for absorption and diffraction volume. The integrated peak intensities were then corrected for the polarization and Lorentz factors. The relative magnitude of the diffraction amplitude was the square root of the integrated intensity. The phases were determined by the swelling method. With

their phases determined, the diffraction amplitudes were Fourier transformed to obtain the bilayer electron density profile (Fig. 3-2). The density profile peaks at the position of the phosphate group on each side of the bilayer. Therefore the peak to peak distance (PtP) corresponds to the phosphate to phosphate distance across the bilayer, which was used as a measure of the bilayer thickness. The errors of the PtP values (± 0.2 Å) were estimated by reproducibility using two to three independently prepared samples.

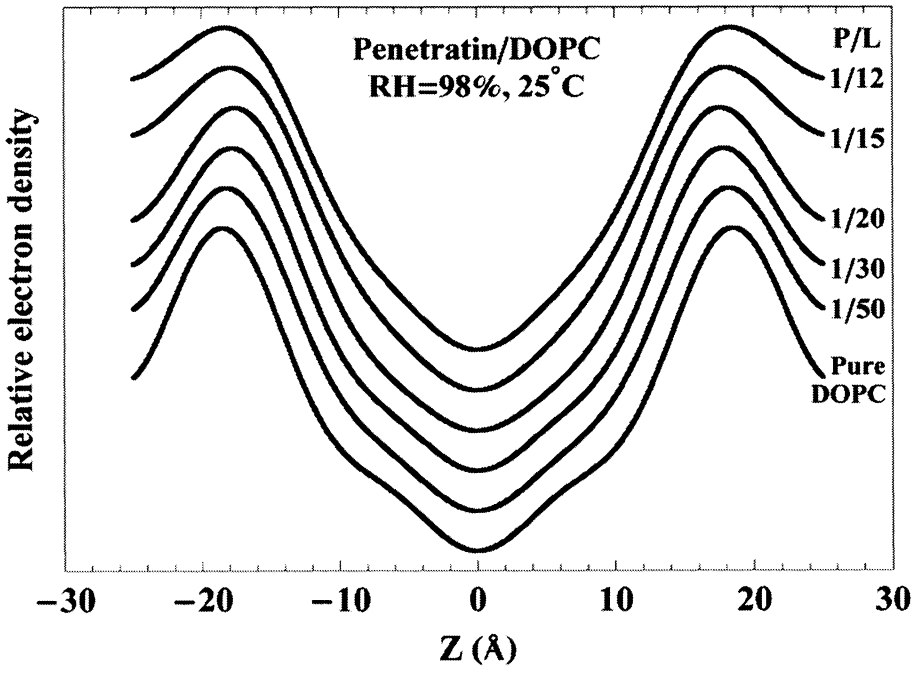

Figure 3-2 Representative electron density profiles across the bilayer in one unit cell, constructed from the data shown in Fig. 3-1.

3.2.3. Circular Dichroism

Spectra were measured in a Jasco (Tokyo, Japan) J-810 Spectropolarimeter. The substrates were oriented normal to the incident light as for the measurement of oriented circular dichroism (OCD) [26]; however no change of peptide orientation was detected during the changes of temperature or humidity. All samples were measured at the same condition as for X-ray diffraction, i.e., 33°C for DMPC, 25°C for other lipids and all at 98% RH. During the experiment, the samples were kept in a temperature-humidity chamber in which the hydration level of the sample was controlled by the relative humidity (RH) of water vapor [69]. To reach the equilibrium condition, the sample was measured after 5-10 minutes once the hydrated level was changed. The scan time for each spectrum was ~4 minutes, including the resetting time, at 1 nm bandwidth, 0.1 nm/point, and 20 nm/min scan rate. The background spectrum for each sample was the spectrum for the same amount of lipid on the same substrate. After the background correction, the spectra of different P/L for each lipid were normalized by the amount of penetratin on each sample and slightly adjusted so that all the spectra cross one isodichroic point. The resulted CD spectra of penetratin in four lipids at various peptide-to-lipid ratio are shown in Fig. 3-3.

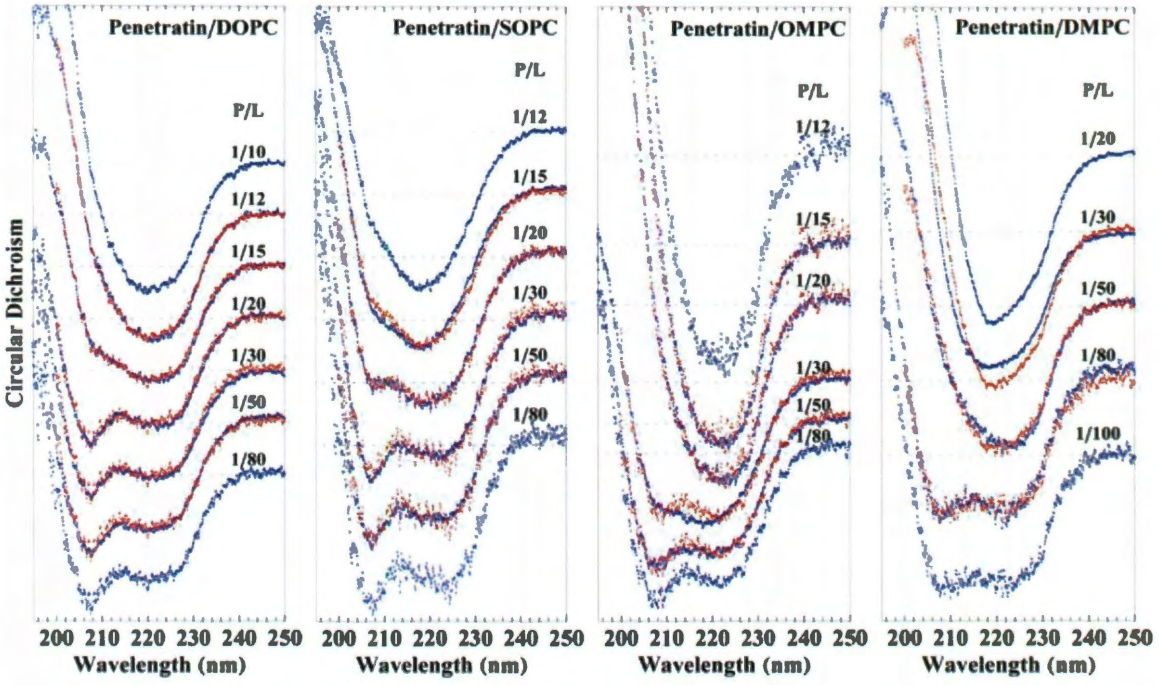

Figure 3-3 CD spectra of penetratin in four lipids as a function of P/L. The measured CD are in blue color; their zero lines were displaced for clarity. For each lipid, the spectra, after the background correction, were relatively normalized to the same amount of peptide. The spectrum of the lowest P/L is defined as Spec[α] and the spectrum of the highest P/L is defined as Spec[β]. All the spectra in between were fit by $c_1 \cdot Spec[\alpha] + (1 - c_1) \cdot Spec[\beta]$ (in red color). From the fit we obtained c_1 versus P/L shown in Fig. 3-5. Reproducibility of the c_1 values from multiple samples was better than 10%.

3.2.4. GUV Experiment

The experiments were performed as described in Sun et al [7]. Briefly GUVs of 7:3 DOPC/DOPG and 0.5% Rh-DOPE were produced in 210 mM sucrose solution by electroformation, and were transferred to a control chamber containing 200 mM

glucose and 10 mM HEPES (pH 7.0). A GUV was aspirated by a micropipette with a small constant sucking pressure (~80 Pa producing a membrane tension ~0.35 mN/m) in the control chamber and then transferred to the observation chamber containing 200 mM glucose, 10 mM HEPES and 6 μM penetratin by the use of a transfer pipette. The osmolality of every solution used in the GUV experiment was measured by a Wescor model 5520 dew-point Osmometer (Wescor, Logan, UT). Equi-osmolality between the inside and outside of the GUV was maintained throughout the experiment. Micropipettes and the glass walls of experimental chambers were coated with 1% bovine serum albumin (BSA) in order to neutralize the charge on the bare glass surface and then washed extensively with water. The video image of the process was captured by a Nikon (Tokyo, Japan).coolSNAP HQ2 camera (Fig. 3-4).

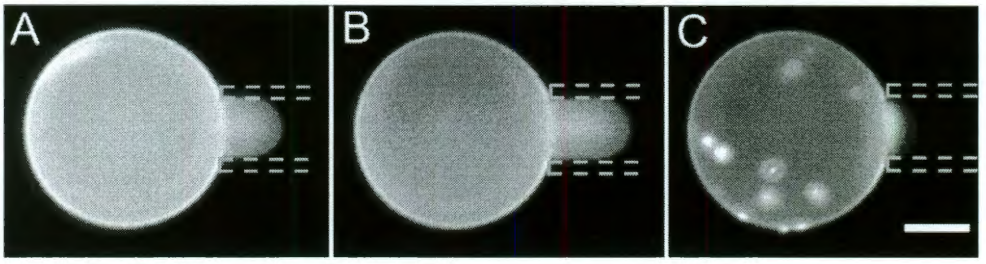

Figure 3-4 Fluorescence images of a GUV (7:3 DOPC/DOPG and 0.5% lipid dye) in a solution containing 6 μM penetratin. The dotted lines indicate the micropipette which is not visible in the fluorescence image. (A) Before the GUV was exposed to penetratin. (B) The increasing protrusion in the micropipette indicated membrane area expansion. (C) Concomitant to the decreasing of the protrusion length, bright spots appeared on the surface of GUV indicating the presence of peptide-lipid aggregates. Scale bar = 20 μm.

A phase condenser was used to record the phase contrast between the sucrose solution inside the GUV and the glucose solution outside (not shown). We found no change in the phase contrast during the experiment, indicating that the GUV volume was constant. Under such a condition, the increase of the protrusion length inside the micropipette (Fig. 3-4B) was corresponding to an area expansion in the membrane surface; conversely, a decrease of the protrusion length (Fig. 3-4C) was corresponding to a decrease in the membrane area [7, 70]. Concomitant with the decrease of the protrusion length, fluorescence clumps appeared on the GUV surface (Fig. 3-4C). This could be explained if the bound peptides formed aggregates that included lipids either by hydrophobic interaction or by electrostatic attraction between cationic peptides and lipid mixtures containing DOPG. The same experiment was repeated several times with the same result.

3.3. Results and Analysis

Four lipids were selected for this study: one of double unsaturated chains 18:1-18:1- PC (DOPC), two of single unsaturated chain 18:0-18:1- PC (SOPC) and 18:1-14:0- PC (OMPC) and one of saturated chains 14:0-14:0-PC (DMPC). Penetratin-lipid mixtures were prepared into parallel multiple bilayers on a flat substrate. We followed the principle of X-ray diffraction which requires the samples to meet appropriate conditions in order to be correctly interpreted [71]. The condition for aligned samples is called "ideally imperfect," i.e., the sample should be composed of slightly misoriented, small mosaic blocks [71]; see examples in [24].

Each sample was measured by X-ray diffraction to produce the electron density profile of the bilayer at ~98% RH; above this humidity level we found the Bragg peaks broadened and high-order peaks diminished due to excessive layer fluctuations [68, 72]. In general, samples of high P/L were more difficult to achieve uniform alignment. All of our samples produced high quality X-ray diffraction (Fig. 3-1), except for DOPC at P/L = 10 which, despite several attempts, diffracted poorly and was therefore not used for analysis.

Note that the electron density measured by lamellar diffraction is the density per unit length in the direction normal to the bilayer, averaged over the plane of the bilayer. This density profile is overwhelmingly dominated by the lipid headgroup because of the in-plane orientation of phosphorylcholines [73] and because of the high correlation of the headgroup position from layer to layer. Interfacial bound peptides do not produce additional density to the profile because, first, they take the place of headgroups and water molecules, and their normal density is not higher than that of in-plane phosphorylcholines, and, second, the correlation of their positions from layer to layer is poor. As a contrast, the ions bound to the gramicidin channels produced distinct bumps in the density profile because of their layer-to-layer correlations [68]. But the heavy atoms labeled to membrane-bound peptides did not (H. W. Huang, unpublished results), nor did the peptides themselves even when they inserted in the low-density chain region (e.g., [74]). In short, peptides did not contribute to the peaks of the electron density profiles. The PtP of the

profile is the average phosphate-to-phosphate distance across the bilayer (see more discussions in [58]).

The multilayer alignment was not a problem for CD measurement (Fig. 3-3) since we were not measuring oriented CD. We note that, in each lipid, the spectra were α-helical-like at low P/Ls but changed to β-like as P/L increased. However both the α-like and β-like spectra are slightly different in different lipids. Such lipid dependence has long been noted for short peptides. For example, the α-helical peptide alamethicin has slightly different CD spectra in different lipids [26, 75]. This is reasonable because of the end effect; the terminal regions often deviate from a continuous α-helical conformation [76] and might vary with lipid environment.

In each lipid, we assume that the spectrum of the lowest P/L is its α-helical spectrum Spec[α] and the spectrum of the highest P/L its β-like spectrum Spec[β]. All the spectra in between were fit by $c_1 \cdot Spec[\alpha] + (1 - c_1) \cdot Spec[\beta]$. The fitting results were shown in Fig. 3-3. The fitted values of c_1 vs. P/L were plotted in Fig. 3-5. To estimate the error for the c_1 value, we re-measured DOPC (P/L = 1/20), SOPC (P/L = 1/20), SOPC (P/L = 1/15) and DMPC (P/L = 1/50) two to three times with independent samples. All reproduced c_1 within ±10%. Within the errors the CD spectra display a critical transition from α-helical-like spectrum to mixtures of α- and β-spectra in each lipid (Fig. 3-5).

From each electron density profile (e.g., Fig. 3-2), the PtP was measured and plotted as a function of P/L in Fig. 3-6. In each lipid, the PtP initially decreased

linearly with P/L until it reached a lowest PtP; it then increased approximately linearly with P/L. We designate the value of P/L corresponding to the lowest PtP by P/L*. The values of P/L* (Table 3-1) obtained from Fig. 3-6 are approximate, since only finite P/L points were measured. Most strikingly the value of P/L* is in agreement with the critical transition value of P/L where CD spectra changed abruptly from α-helical-like to mixtures including β-spectra in each of four different lipids.

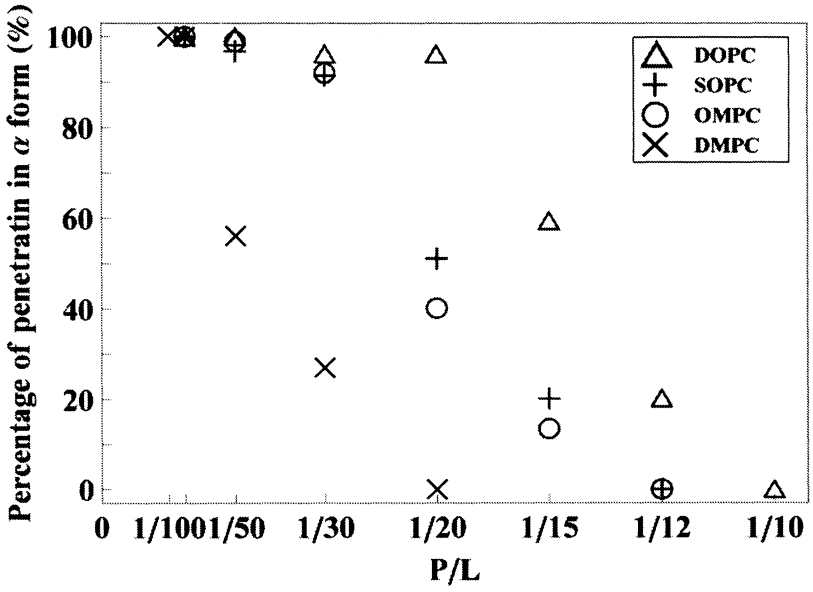

Figure 3-5 Percentage of penetratin in the α-helical form c_1 versus P/L, determined from Fig. 3-3.

	A_L (Å^2)	A_s (Å^2)	P/L^*	$\epsilon^o_\alpha - \epsilon^{o*}_\beta$
DOPC (25°C)	72.7	102	1/20	$1.3k_BT$
SOPC (25°C)	67.4	155	1/30	$1.6k_BT$
OMPC (25°C)	68.8	144	1/30	$2.1k_BT$
DMPC (33°C)	61.9	155	1/65	$-0.4k_BT$

Table 3-1 Physical constants of penetratin bound to lipid bilayers (the values of $\epsilon^o_\alpha - \epsilon^o_\beta$ are for the minimum β-aggregates).

In each panel of Fig. 3-6, PtP versus P/L below P/L* was fitted with a straight line. The P/L coordinate was projected vertically upward until it intersects the fitted line and then horizontally rightward as indicated by the dotted lines. The projected vertical coordinate of P/L was used as the coordinate of N_α/L, the number of peptides in the α-helical conformation divided by the number of lipid molecules. We then imported the data $N_\alpha/L = c_1(P/L)$ from Fig. 3-5. The experimental results in the P/L < P/L* region were clear: (1) the PtP values were well fitted by a straight line and (2) the N_α/L values were close to the corresponding P/L values, indicating that all of the bound peptides were in the α-helical form and that the membrane thinning (PtP) was proportional to the amount of the α-helical bound peptides. Therefore the N_α/L coordinate on the right-hand side of Fig. 3-6 can be viewed as representing the amount of α-helical bound peptides responsible for decreasing the bilayer thickness to the corresponding PtP value on the left-hand side coordinate.

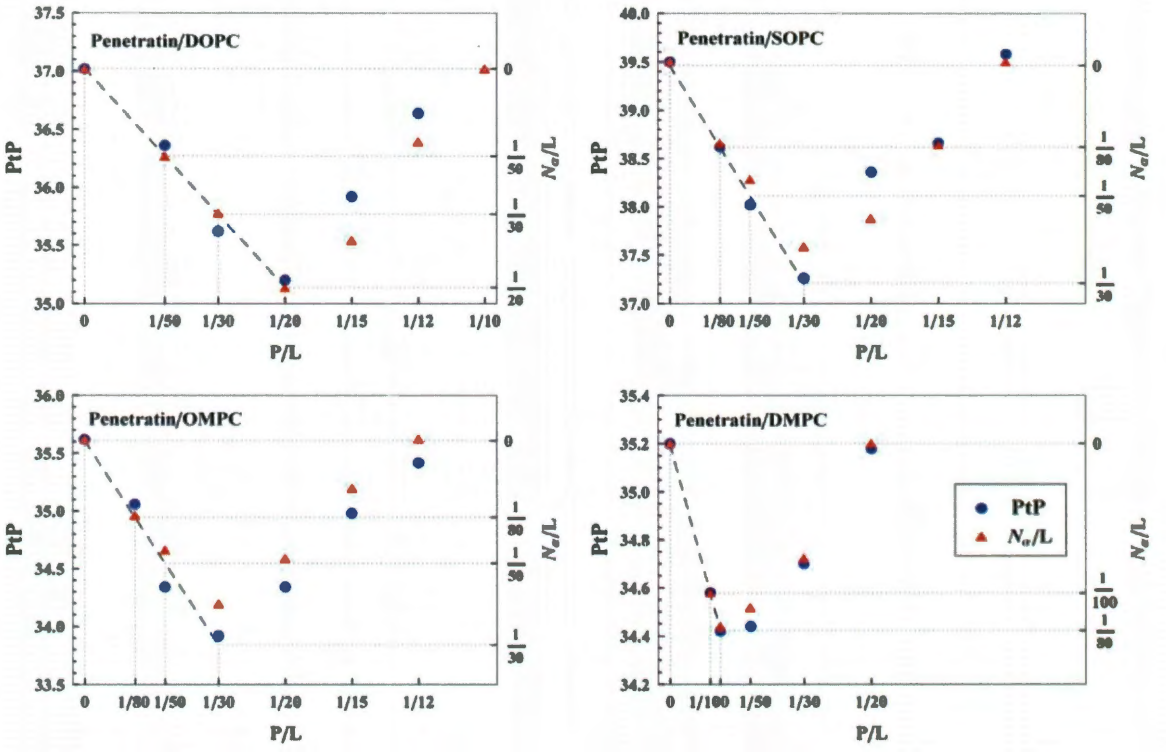

Figure 3-6 PtP vs. P/L and comparison with N_α/L. The lowest PtP point defines P/L* (Table 3-1). For P/L < P/L*, there is a linear relation between PtP and P/L shown by the dash line (a linear fit). The coordinate of N_α/L on the right-hand ordinate was chosen to coincide with the P/L value on the dash line so that there is a one-to-one correspondence between the PtP value and the N_α/L value on the same horizontal line. The agreement between PtP and N_α/L, for P/L > P/L*, supports the assumption that membrane thinning was due to the α-helical bound peptides and that the peptides in the β conformation did not affect the membrane thickness.

Thus in the P/L > P/L* region, the approximate agreement between the experimental PtP on the left coordinate and N_α/L on the right coordinate of Fig. 3-6 indicates that, even in the high P/L region, the membrane thinning was also

essentially due to the α-helical peptides only. Peptides in the β conformation did not contribute to membrane thinning. Therefore the peptides in the β conformation were most likely not embedded in the bilayers. Another possibility for the β-form penetratin not to affect the membrane thickness is for it to insert transmembrane. But this would require coincidental hydrophobic matching between the peptide aggregates and all four lipid bilayers [64]. Considering the high charge density of penetratin (7 out of 16 are positively charged), such a possibility seems unlikely.

In the third experiment, a giant unilamellar vesicle (GUV) made of 7:3 DOPC/DOPG and 0.5% lipid dye was aspirated by a micropipette and transferred to a solution containing penetratin (Fig. 3-4A). As the peptides gradually bound to the vesicle membrane, we observed the reaction of the GUV to the increasing P/L. Initially the membrane area expanded until it reached a maximum (Fig. 3-4B). Since membrane area expansion was equivalent to membrane thinning, this corresponded to P/L $\longrightarrow$ P/L* in Fig. 3-6. Then the GUV area decreased from the maximum expanded value, corresponding to the increasing membrane thickness observed in the P/L > P/L* region in Fig. 3-6. Concomitant with the area decrease, aggregates began to appear on the surface of GUV (Fig. 3-4C). This was consistent with penetratin forming β aggregates on the membrane surface when P/L exceeded P/L*.

Taken together we have high quality data from two entirely independent experiments in striking agreement with each other in each of four arbitrarily chosen lipids. The data demonstrated that penetratin initially bound to the bilayers in the α-helical form and thinned the membrane in proportion to the amount of bound

peptides per lipid P/L, until P/L reached a critical value P/L*. In this below P/L* region, practically all of the bound peptides were in the α-helical form, i.e., P/L ≈ N_α/L. As soon as P/L exceeded P/L*, β-form penetratin began to appear and the percent of β-form increased with P/Luntil it reached 100%, in parallel to the membrane thinning decreasing to zero. Even in this above P/L* region, the membrane thinning was also proportional to N_α/L, with the same proportionality as in the P/L < P/L* region.

3.4. Discussion

We now try to understand the implications of the very systematic results we have obtained. What is the implication of the essentially pure α-helical region where the membrane thickness linearly decreases with P/L? What is the implication of the existence of a critical concentration P/L* where the thinning is maximum and the β-form peptide begins to appear? What is the implication of the P/L > P/L* region where the membrane thinning decreases in proportion to the decreasing fraction of peptides in the α-form, both are in proportion to P/L − P/L*, and eventually the membrane recovers to its pure bilayer thickness when all of the peptides turn into the β-form? Finally, what is the implication of the lipid chain dependence?

3.4.1. Thermodynamics of membrane-mediated α to β conformation change

Amphipathic molecules typically bind to the hydrophilic-hydrophobic interface of the lipid bilayer first [58]. Such bindings are characterized by a membrane thinning in proportion to the amount of bound molecules per lipid, as shown in the initial phase of penetratin binding to each lipid (Fig. 3-6). Previously we have called this binding phase the S phase, which has the lowest binding free energy compared with other possible binding states [58]. However, since the interfacial binding stretches (increases) the membrane area (hence thinning), it incurs an elastic energy in the lipid bilayer. As a result the energy level of the S phase increases linearly with P/L. This has an important effect on how the peptide distributes between the interfacial binding state and other possible binding states.

Thus the most important characteristic of the S phase binding is the value A_S, the monolayer area increase caused by one peptide binding. If the number of peptides bound in the S phase is N_S, the total monolayer area increase is $\Delta A = N_S A_S$. The total monolayer area of the pure lipid bilayer is $A = A_L L$, where A_L is the cross section area per lipid molecule. The fractional area expansion $\Delta A/A$ is related to the fractional thickness decrease of the hydrocarbon region $\Delta h/h$ by the chain volume conservation [77]: $\Delta A/A \approx -\Delta h/h$, where the hydrocarbon thickness h is directly obtained from PtP by $h \approx PtP - 10$ Å [58]. It follows that

$$\Delta h/h = -(A_S/A_L)(N_S/L) \tag{3-1}$$

Thus the value of A_S can be measured from the initial slope of $\Delta h/h$ versus P/L. A_L can be independently measured by the chain volume [78] and h. These values are listed in Table 3-1.

The fractional area expansion $\Delta A/A$ is a strain whose corresponding stress is the monolayer tension $\sigma = (K_a/2)(\Delta A/A)$, where $K_a/2$ is the monolayer stretch coefficient. (K_a is the bilayer stretch coefficient; its value is about 240 mN/m for most common phophatidylcholines [79]). Therefore the energy level for the S phase binding is given by

$$E_S = -\epsilon_S^o + \sigma A_S = -\epsilon_S^o + (K_a/a)(A_S^2/A_L)(N_S/L) \tag{3-2}$$

and the chemical potential by [58]

$$\mu_S = -\epsilon_S^o + (K_a/a)(A_S^2/A_L)(N_S/L) + k_B T ln X_s \tag{3-3}$$

where ϵ_S^o is the intrinsic binding energy of penetratin to the bilayer interface and $X_S \cong N_S/L$. The last term of Eq. (3-3) comes from the entropy of mixing (where k_B is the Boltzmann constant and T the temperature) following the thermodynamic theory of micellar solutions [80]. This chemical potential describes the energetics of binding to the interface of a lipid bilayer by amphipathic molecules, including AMPs and amphipathic drugs [58]. Since the penetratin peptides bound to the S phase are in the helical conformation, we let $\mu_S = \mu_\alpha$, $\epsilon_S^o = \epsilon_\alpha^o$, $N_S = N_\alpha$, and $E_S = E_\alpha$ for the convenience of following discussion.

From our CD measurements, we know that the second membrane-binding phase of penetratin is in the β conformation. More importantly, our experimental data suggested that the β-states appeared only at concentrations P/L above a threshold value P/L*, below which there were practically no peptides in the β-states. This is a strong indication that the β-states were oligomeric aggregates, or more specifically, there were no monomeric β-states. The reason is that if there were monomeric β-states, there had to be a significant fraction of peptides occupying such states in the P/L < P/L* region according to the Boltzmann distribution. This can be shown as follows.

Assume that the smallest β-state consisted of n monomers with a chemical potential given by [80]

$$\mu_n = -n\epsilon_\beta^o + k_B T ln X_n \tag{3-4}$$

where $-\epsilon_\beta^o$ is the energy per peptide for the smallest β-state and $X_n \cong N_{\beta n}/L$; $N_{\beta n}$ is the number of n-meric β-states occupied by the peptide. As pointed out by J & L [38] , the states of proteins often reflect a kinetic effect rather than that of true thermodynamic equilibrium. Before the appearance of the smallest β-states, the only bound states accessible to the peptides in solution are the interfacial binding state in α helical conformation and the smallest β-state. The larger β-aggregates become accessible only after the appearance of the smallest β-state; this was called the kinetic barrier of nucleation [38]. Thus in the region of P/L < P/L*, the state of

the peptide is determined by the quasi-equilibrium condition $\mu_n = n\mu_\alpha$. This equation and the condition $N_\alpha + N_{\beta n} = P$ determine the values of N_α and $N_{\beta n}$, and the solution can be compared with the membrane thinning data via Eq. (3-1). The solution for N_α and $N_{\beta n}$ by curve-fitting to $\Delta h/h$ versus P/L involved three parameters: $a = (\epsilon_\alpha^o - \epsilon_\beta^o)/k_BT$, $b = K_a\,(A_S^2/2A_L)/k_BT$ *and* n. b was determined by A_S which was in turn determined by the initial slope of $\Delta h/h$ versus P/L (K_a and A_L were already known). a and n were to be determined by solution N_α agreeing with Eq. (3-1) and the data. This procedure has been described in great detail for the problem of AMPs recently [58].

However, there is an important difference between these two cases. For AMPs, the equilibrium condition between Eq. (3-3) and (3-4) was assumed to be valid for the entire range of P/L, both below and above P/L*. The curve fitting to the entire range of $\Delta h/h$ versus P/L produced a narrow range of values for parameter a and n [58]. In contrast, penetratin is expected to have multiple aggregation states larger than the minimum β-state in the P/L > P/L* region, therefore the quasi-equilibrium condition between Eq. (3-3) and (3-4) is valid only for P/L ≤ P/L*. The data required the solution to have vanishingly small $N_{\beta n}$f (more precisely, $nN_{\beta n}/P \ll 1$) for the entire range of P/L < P/L*. Although this requirement alone is insufficient to solve for the parameters a and n, it is sufficient to limit the value of n to n ≥ 4, as demonstrated in the previous analysis [58]. In other words, unless the minimum β-state is an oligomer of n ≥ 4, it is impossible to have a finite range of P/L in which essentially no peptides are in the β-state. This is the well-known critical

micellar condition [80, 81]. In a micellar solution, molecules remain monomers at concentrations below a threshold value called the critical micellar concentration or CMC, provided the smallest micelles consist of a sufficiently large number of monomers, n > 15 [58, 80]. In membranes, the micellar effect requires only n ≥ 4 because the energy level of the monomeric state includes a concentration dependent term due to membrane thinning. Thus the important conclusion from this analysis is that membrane binding facilitates the transformation of penetratin from α-monomer to β-aggregate by elevating the energy level of the monomeric state with concentration. In Table 3-1, we give the values of a for the minimum aggregates n = 4 that produce the P/L* for each lipid. (Note that the negative value of $\epsilon_\alpha^o - \epsilon_\beta^o$ for DMPC is not an anomaly. The antimicrobial peptide alamethicin also has a negative value of $\epsilon_\alpha^o - \epsilon_\beta^o$ [58].)

In a two-level micellar model, the monomer concentration remains constant above the CMC and all the amphiphiles in excess of CMC form monodisperse micelles [80]. This is essentially the case for AMPs. Like penetratin, AMPs bound to the bilayer interface and caused membrane thinning. When they formed pores above a critical concentration, the pores had no significant effect on the membrane thickness. As a result, the PtP versus P/L for AMPs had the characteristic of a two-level micellar model: the bilayer thickness decreased linearly with P/L up to P/L*, and then practically remained constant above P/L* [58], indicating that AMPs were entirely monomeric below P/L*, and, above P/L*, the concentration of monomers remained at the critical level amid the membrane pores. The case of penetratin, as

shown in Fig. 3-6, is very different. Below P/L* its behavior is identical to AMPs, but above P/L* the concentration of monomers, i.e., N_α/L, decreased more or less linearly with P/L. We believe that the reason that N_α/L decreased above P/L* is explained by the J & L model and the reason it decreased in an approximately linear fashion is particular to multilayer samples.

J & L [38] proposed nucleation-dependent polymerization as the molecular mechanism for amyloid formation. In the present case, the minimum size β-aggregate is the nucleus for β aggregation. The quasi-equilibrium condition used for the nucleation process in the P/L < P/L* region followed the J & L model. The subsequent binding of monomers to the aggregate is thermodynamically favorable because monomers contact the growing aggregate at multiple sites [38]. This means that the binding energy E_β for the monomers to the β-aggregate decreases with the growth of the aggregate, because in average the larger aggregate would present more available contact sites. According to this model, once nuclei have formed, the aggregates should grow by accumulation of monomers or by coalescence of small aggregates; until most monomers disappear. We suppose that this did not happen in our experiment because the mobility of peptide aggregates in lipid multilayers was increasingly limited as their size grew. Once monomers and very small aggregates formed a sufficiently large local aggregate, the latter were more or less frozen within the matrix of lipid multiplayers, preventing the formation of very large aggregates. Local aggregates grew to a size proportional to (P/L − P/L*), so that the size-dependent energy for the β-aggregates was in average approximately

$$E_\beta = -\epsilon_\beta^o - c(P/L - P/L^*)$$

(3-5)

where c is a positive constant. Then the equality between the chemical potential of the aggregates and μ_α(Eq. (3-3)) would lower the value of μ_α by decreasing N_α/L in proportion to (P/L − P/L*). As P/L continued to increase, eventually E_β became lower than $-\epsilon_\alpha^o$, then all of the bound peptides turned into β aggregates, and the bilayer thickness recovered the value of free lipid bilayer (Fig. 3-6).

Local aggregates in our samples of neutral lipids were not visible under microscope. However, in a lipid mixture containing anionic components, the peptides aggregates were enlarged by incorporating lipids and were visible under microscope (Fig. 3-7). The observed uniform distribution of aggregates in the multilayer samples was consistent with the assumption of local aggregation.

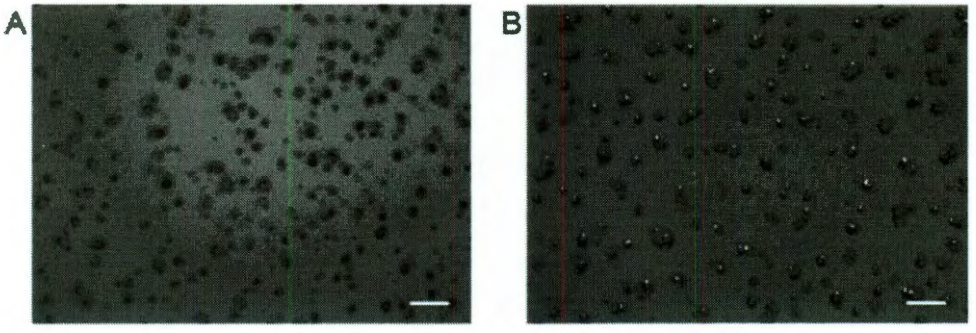

Figure 3-7 Microscopic (white light) images of DOPC/DOPG 7:3 multilayers containing penetratin (A) at P/L = 1/12 and (B) at P/L = 1/10. Scale bar = 200 μm.

3.4.2. Effect of unsaturated chains

How could the degree of chain unsaturation influence the β-formation of penetratin?

The formation of a nucleus is the defining characteristic of a nucleation-dependent polymerization. The J & L model [38] envisions the formation of a nucleus as the rate-determining step because it requires a series of association steps that are thermodynamically unfavorable. What we found is that membrane binding facilitates the development of nuclei for aggregation. The interface of a lipid bilayer provides energetically favorable binding sites for penetratin in the monomeric form. However increasing the bound molecules per lipid elevates the energy level of the bound states toward a higher level that favors creation of small β-aggregates, the nuclei for amyloid formation. This explains the observed conformation change of penetratin bound to vesicles, from α to β, as the peptide concentration increased [11-13].

If this idea were correct, qualitatively we would expect the critical concentration P/L* to increase with greater degree of unsaturation in the lipid chains, given the same headgroup. This is because chains with more unsaturations have larger cross sectional areas and will provide more room in the headgroup region; therefore, a smaller strain would be created by peptide binding in the interface. This means a larger N_α/L is required to elevate the energy level of the α bound states to the critical value favoring the formation of small β-aggregates, hence

larger P/L*. Indeed this was supported by the observation $P/L^*_{DOPC} > P/L^*_{SOPC}$, $P/L^*_{OMPC} > P/L^*_{DMPC}$ (Table 3-1).

The strain in the lipid bilayer was caused by the area expansion A_S per peptide binding. The value of A_S is roughly the cross section of the peptide (parallel to the helical axis) minus the area vacated by the water molecules released from the lipid headgroup region during the process of peptide binding [74]. The values of A_S obtained from the experimental data (Table 3-1) are consistent with the idea that A_S decreases with increasing degree of chain unsaturation. Thus the lipid chain dependence discovered in this study provided supporting evidence for the membrane-mediated nucleation theory.

Chapter 4

How Type II Diabetes Related Islet Amyloid Polypeptide Damages Lipid Bilayers

4.1. Introduction

Diabetes affects nearly 8.3% of American population and is the 7th leading cause of death in the United States. In adults, type 2 diabetes accounts for about 90% to 95% of all diagnosed cases of diabetes [82]. One possible cause of impaired insulin secretion in type 2 diabetes is attrition of insulin-producing β-cells [15]. Prevailing hypotheses that explain the underlying cell attrition are the deleterious effects on the cell membranes by human islet amyloid polypeptide (hIAPP), a 37 residue peptide that is synthesized in pancreatic islet β-cells and co-secreted with insulin [16-20]. A large body of research has described the phenomena of hIAPP interactions with lipid bilayers (see references below). Yet it has been difficult to

correlate the effects on lipid bilayers with the effects of hIAPP added to islet cells in culture which indeed induce cell death [19, 83]. In this report we studied the responses of giant unilamellar vesicles (GUVs) exposed to hIAPP in various conditions. In order to understand the physical process of hIAPP-GUV interactions, we also performed X-ray diffraction in conjunction with circular dichroism (CD) measurements. The combined results provide new structural information about the hIAPP-membrane interactions, and reveal a low threshold peptide concentration for damaging the membranes. Monomeric hIAPP molecules at concentrations above the threshold convert to β-sheet aggregates via membrane-binding, which subsequently damage the lipid bilayer. We use these results to speculate how IAPP monomers may interact with cell membranes.

A great deal of IAPP studies made use of the contrast between hIAPP which is amyloidogenic and rodent IAPP (rIAPP) which is not [84, 85]; both are 37-residue peptides differing only in $IAPP_{22\text{-}29}$ [85]. Significantly, rodents do not develop diabetes-like symptoms even when rIAPP was overexpressed [86]. Thus the occurrence of diabetes in hIAPP-transgenic rodents has been regarded as the strongest evidence associating hIAPP with diabetes [87]. However, the initial assumption that the formation of extracellular IAPP amyloid causes β-cell apoptosis has been disproved by the absence of correlation between cytotoxicity and extracellular amyloids [19, 88]. When amyloid fibrils were added to islet cells in culture, apoptosis was not induced. In contrast, if a freshly prepared aqueous solution of hIAPP was added to islet cells in culture, cell death was reproducibly

induced and electron microscopy revealed the presence of small aggregates on cell membranes that were interpreted as hIAPP oligomers disrupting the cell membrane and penetrating the cell [16, 83]. Also the drug rifampicin inhibited hIAPP amyloid formation but failed to inhibit hIAPP cytotoxicity [88]. Thus in a current amyloid hypothesis, the toxicity is caused by hIAPP oligomers which are not pre-amyloid fibrils or protofibrils, but are an off-amyloid fibril pathway form of oligomer [19]. However, so far the structures of these presumed toxic oligomers are unknown (such as their CD), nor have such oligomers been isolated [19]. The possibility of hIAPP forming low-molecular weight oligomers was recently examined by Vaiana et al. [89] using ultracentrifugation and by Soong et al. [20] using diffusion NMR spectroscopy and both obtained negative results.

The peptide hIAPP dissolves in aqueous solutions, initially in random coil configurations as indicated by CD, however the CD spectrum will gradually change to that of β-sheet indicating β-amyloid formation [17, 83]. Electron microscopy (EM) showed the peptide turned into aggregates or fibrils [83, 90, 91]. X-ray fibre diffraction [91] showed a meridional reflection at 4.7 Å and a equatorial reflection at 9.5 Å, corresponding to the typical cross-β structure seen in the fibrils formed by other amyloid diseases [92, 93]. The speed of change from random coils to β-sheets in solution depended on the peptide concentration, temperature, and other solution conditions, such as pH, ions and buffers [94]. In general the higher the concentration, the faster the change rate was. It seemed possible that the peptide would remain a random coil at very low concentrations, for example at the

physiological circulating concentrations of hIAPP (estimated to be 5-20 pM) [19, 95]. The transition from random coil to β-sheet in solution appeared not to involve α-helical configuration. This is in contrast to the conformation changes mediated by membrane binding [18, 96-98]. Human IAPP spontaneously binds to lipid bilayers; particularly if the bilayers include anionic lipids (IAPP has 3 cationic amino acids). If IAPP was initially in random coils, the binding changed its CD to α-helical form initially but the spectrum invariably transformed to that of β-sheets in time [96, 98]. Again, the membrane bound aggregates and fibrils have been seen by EM [97] and by light microscope [99].

As summarized and reviewed recently by Gorbenko and Kinnunen [100] and by Jayasinghe and Langen [18], membranes have been implicated as the catalyst that facilities fibril formation [96, 97] and as the targets of IAPP toxicity [16, 17]. A theory for membranes as amyloid-catalyses has been advanced by Apostolidou et al. [101] who obtained the EPR resolved α-helical core (residues 9-22) of hIAPP bound to lipid vesicles; they suggested that the lining-up of the helical parts on the surface of membranes facilities the aggregation and β-sheet formation of the amyloidogenic regions of hIAPP. The toxicity effect has been attributed to IAPP induced membrane permeabilization, variably described as ion channels/pores [16, 17, 90, 102-104] or membrane damage by the extraction of lipids from the bilayer [99, 105-107]. More recently Engel et al. [108] investigated the correlations between the growth of peptide fibril and their effects on lipid vesicles. They concluded that pre-formed or mature hIAPP fibrils did not interact or damage lipid bilayers, but during the growth

of fibrils from membrane-bound monomers, the peptide-lipid interactions extracted lipids from the bilayers that caused membrane damages. On the other hand, Knight et al. [98] proposed that it is the aggregation of the IAPP α-helices on the membrane that induces toxicity. Somewhat similarly Soong et al. [20] suggested the toxicity being due to well-defined ion channels formed by aggregation of monomeric IAPPs bound to the membrane.

In this report we hope to gain a better understanding of the physical process in which hIAPP induces membrane damage. We will gain this understanding by new experiments and also by comparing the effects of hIAPP with the known behaviors of other membrane-active peptides. In particular, the membrane-mediated amyloid formation of penetratin is a useful reference for the more complex reactions by hIAPP. Penetratin dissolves in solution as a random coil and has never been found in the β-amyloid form in solution. However it binds to the lipid bilayer interface in the α-helical form as long as the peptide/lipid ratio (P/L) is below a lipid-dependent threshold value. As soon as P/L exceeds the threshold value, penetration progressively transforms to β-aggregates and exits from the lipid bilayer interface [109]. The process of forming the β-aggregates extracts lipid molecules from the lipid bilayer. We will see that hIAPP exhibits a similar behavior.

4.2. Materials and Methods

4.2.1. Materials

Human IAPP, KCNTATCATQRLANFLVHSSNNFGAILSSTNVGSNTY (disulfide bridge: 2-7), was synthesized to HPLC purity > 95% by AnaSpec (Fremont, CA). DOPC, DOPG and Rh-DOPE were purchased from Avanti Polar Lipids. All chemicals were purchased from Sigma-Aldrich and were used without further purification. All experiments were performed at room temperature ~25°C.

4.2.2. Preparation of monomeric hIAPP

We followed an established protocol for the preparation of monomeric hIAPP [17, 20]. HIAPP was first dissolved in hexafluoroisopropanol at 0.5 mg/mL and sonicated for 5 minutes. The solution was then lyophilized. A stock solution of 100 μM hIAPP was prepared in 200 mM glucose solution. The peptide configuration in the solution was continuously monitored by CD. The result showed that hIAPP remained in random coil configurations for at least one week in pure glucose solution. On the other hand, if hIAPP was dissolved in 199 mM glucose and 1 mM Tris buffer (at pH 7.0), β aggregate started to form in about 4 hours. For each run of the experiment, the stock solution was diluted with 199 mM glucose and 1mM Tris (pH 7.0) to a desired hIAPP concentration. CD spectrum was measured to confirm that the peptide was in random coil form. The solution was used immediately after dilution and the experimental time for each run was about 20 minutes.

4.2.3. Preparation of hIAPP fibrils

A stock solution of 200 μM hIAPP was made in 190 mM glucose and 10 mM Tris (pH 7.0) solution. For experiment, the stock solution was diluted with 199 mM glucose and 1 mM Tris (pH 7.0) to a desired hIAPP concentration.

Fibrillization of peptide samples was monitored by a thioflavin T (ThT) dye binding assay [17, 108]. Diluted samples were mixed with ThT (2 μM) and its fluorescence was measured by a spectrophotometer (Ocean Optics, Dunedin. FL). We found that the ThT fluorescence saturated after ~6 hours (Fig. 4-1). CD spectrum was measured to check that the hIAPP was indeed in the β form. For experiments with mature hIAPP fibrils, the stock solution was kept at 4°C for two weeks.

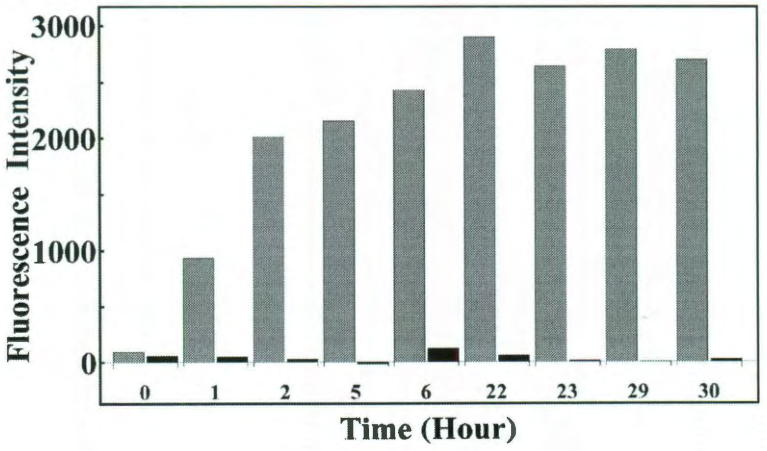

Figure 4-1 Thioflavin T (ThT) dye binding assay for fibril formation. The prepared (fibril) sample was mixed with ThT (2 μM) and its fluorescence was monitored by a spectrophotometer. Gray bars are the fluorescence intensity of the test sample and black bars are the control (without hIAPP).

4.2.4. Aspirated GUV experiments

The experiments were performed as described in Sun et al. [7]. Briefly, GUVs of pure DOPC or 7:3 DOPC/DOPG, plus 0.5 mol % Rh-DOPE, were produced in 200 mM sucrose solution by electroformation [37], and were transferred to a control chamber containing 199 mM glucose and 1 mM Tris (pH 7.0). A GUV was aspirated by a micropipette with a small constant sucking pressure (~100 Pa producing a membrane tension ~0.4 mN/m) in the control chamber and then transferred, via a transfer pipette [7], to an observation chamber containing 199 mM glucose, 1mM Tris, and hIAPP at a specified concentration. The osmolality of every solution used in the GUV experiment was measured by a dew-point Wescor model 5520 osmometer. Solutions of the same osmolality were used inside and outside of the GUV in each experiment. The experiment was recorded by fluorescence imaging using a Nikon CoolSNAP HQ2 camera. The phase contrast between the sucrose solution inside the GUV and the glucose solution outside was inspected at randomly chosen times to determine if any change occurred.

The analysis of the GUV response is based on the change of the protrusion length L_p of the GUV in the micropipette [70]: Under the condition of no volume change, the change of membrane area is $\Delta A = 2\pi R_p(1 - R_p/R_v)\Delta L_p$, where R_p and R_v are radii of the micropipette and the GUV. All the values of R_p, R_v and L_p were carefully measured and analyzed by using the Nikon NIS-Elements BR 2.30

software. To normalize the area changes in different GUVs, ΔL_p was converted to the fractional change of the vesicle area $\Delta A/A$.

4.2.5. HIAPP β-fibrils mixed with GUVs

10 μL of the GUV suspension was transferred to an observation chamber containing 199 mM glucose, 1 mM Tris at pH 7.0, and 2.5 μM hIAPP in β-fibril form. The GUVs settled to the bottom due to the density differential and were observed with a Nikon confocal microscope.

4.2.6. GUV Leakage experiment

For leakage experiment, the solution in the GUV production chamber also contained 10 μM calcein. Two observation chambers containing the same solution (199 mM glucose and 1mM Tris at pH7.0) were set side by side. 10 μL of the GUV suspension was injected into the first observation chamber and were well-mixed with the solution in the chamber by stirring with a micropipette. About ten GUVs were transferred from the first to the second chamber via a transfer pipette. The purpose of this transferring procedure was to dilute the untrapped calcein. The GUVs settled at the bottom due to the density differential and were observed under an Olympus (Tokyo, Japan) microscope model IX81 and recorded with a Hamamatsu Photonics (Hamamatsu City, Japan) digital CCD camera model C10600-10B. 0.5 μL of the monomeric hIAPP stock solution was injected into the observation chamber (to a final concentration 0.1 μM) and GUVs were observed for 5 minutes. Then another 0.5 μL was injected and observed for the next 5 minutes. This process was

repeated in the sequence of increasing hIAPP concentrations, until all the GUVs under observation ruptured. The highest final hIAPP concentration in the observation chamber was 0.5 μM. The leakage of GUV content was monitored by calcein fluorescence. During the experiment, the lipid dye and content dye were inspected alternately by switching between two dichroic/filter sets.

4.2.7. Preparation of multilayer samples for CD and X-ray diffraction

The procedure for preparing peptide/lipid mixtures in aligned multiple layers has been fully described in Ludtke et al. [63]. IAPP was first dissolved in tetrafluoroethylene. Appropriate amounts of IAPP and DOPC for a chosen peptide/lipid molar ratio, P/L, were mixed in 1:1 (v/v) chloroform and tetrafluoroethylene. The mixture was uniformly spread on a thoroughly cleaned quartz substrate (0.05 mg peptide on a 1 cm^2 quartz plate for $P/L > 1/30$; 0.3 mg of lipid on a 1 cm^2 plate for $P/L \leq 1/30$). After the solvent evaporated in vacuum, the sample was hydrated with 50% RH water vapor in room temperature overnight. The results were well-aligned parallel bilayers, as proven by X-ray diffraction. During the experiment, the samples were housed in a temperature-humidity chamber in which the hydration level of the sample was controlled by the relative humidity (RH) of water vapor [69]. All measurements were performed at 25°C and 60% to 98% RH.

4.2.8. CD Experiment

CD spectra were measured in a Jasco J-810 spectropolarimeter. The subtracts of stacked membrane were oriented normal to the incident light, as for the measurement of oriented circular dichroism [26]. The background spectrum for each sample was the spectrum for the same amount of lipid on the same substrate. After the background correction, the spectra of different *P/Ls* were normalized by the amount of IAPP for each sample.

4.2.9. X-ray Diffraction Experiment

X-ray samples were prepared and measured in a temperature-humidity chamber at the same conditions as for CD experiment. ω-2θ diffraction was collected on a Huber goniometer, with a vertical line-focused Cu K_α source operating at 35 kV and 15–30 mA.

An attenuator was used to prevent the first-order Bragg peak from saturating the detector. Each ω-2θ scan was performed from $\omega = 0.5°$ to $\omega = 7.5°$ with a step size of $\Delta\omega = 0.01°$ (for details see [64]). The scan was repeated 2-3 times for each hydration level and then averaged for data analysis. To use the swelling method [67] for the determination of the phases of diffraction amplitudes, each sample was scanned at several different hydration levels between 70% and 98% relative humidity (RH).

The procedure of data reduction was described in Section **3.2.2.** and in many of our previous works [64, 68]. After data reduction, the diffraction amplitudes were used to reconstruct the electron density profile of the bilayer. Across the bilayer profile, the phosphate peak to phosphate peak distance (PtP) was measured for the bilayer thickness. Measurements by the above described procedure have been done for various peptide-lipid mixtures for more than a decade, e.g., [64-66]. We found in each case the measured PtP reproducible within ± 0.2 Å.

4.3. Results and Analysis

4.3.1. Aspirated GUV exposed to monomeric hIAPP

The reaction of an aspirated GUV when exposed to monomeric hIAPP depended on the peptide concentration. At low concentrations (e.g., 0.05 μM), the binding of hIAPP simply lengthened the GUV protrusion length. At high concentrations (e.g., 1 μM), the binding of hIAPP caused the protrusion to increase to a maximum and then decreased. As the protrusion length decreased, small aggregates containing lipid dye appeared on the surface of GUV; some of these aggregates would come off the GUV surface (Fig. 4-2). Very importantly, we found the phase contrast between the GUV interior (sucrose) and the solution background (glucose) did not change during the whole process, indicating that no leakage of the GUV content occurred.

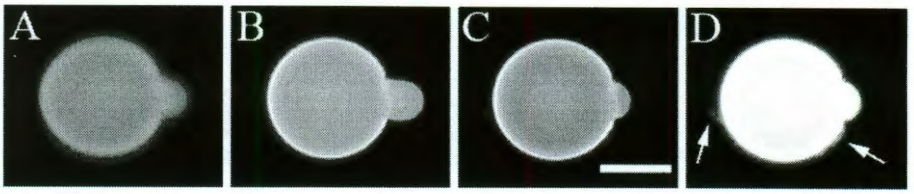

Figure 4-2 Time sequence of a GUV (7:3 DOPC/DOPG, plus 0.5 mol % Rh-DOPE) containing 200 mM sucrose exposed to 0.25 μM monomeric hIAPP in 199 mM glucose and 1 mM Tris buffer (pH 7.0). (A) t=0; (B) the protrusion length first increased; (C) then the protrusion length decreased; (D) the high-contrast fluorescence image of (C) shows aggregates (indicate by arrows)--some appeared to be coming off the surface of GUV. Scale bar = 20 μm.

The protrusion length decrease could be due to either a GUV volume increase at constant membrane area or a membrane area decrease at constant volume [57, 70, 110]. One possibility for volume increase is due to the formation of pores in GUV, as in the case of melittin binding [110, 111] or magainin binding [57]. The finite-sized pores would allow the permeation of the smaller glucose into the vesicle more than the permeation of the larger sucrose out of the vesicle; and the resulted osmolality imbalance would induce a net water influx to cause a volume increase at constant membrane area; hence the protrusion length decrease [110, 111]. This did not happen with hIAPP, since the phase contrast of the GUV did not change [111]. To further prove that the hIAPP-induced protrusion decrease was not by pore formation, we repeated the experiment with both inside and outside of GUV in sucrose solutions. In this case, the protrusion length would not decrease (since there would be no net influx or efflux) if the effect of hIAPP was inducing pores [as shown in [57]]; but the protrusion length did decrease (Fig. 4-3C). This proved that

the observed decrease of protrusion length was due to a membrane area decrease. This phenomenon is similar to the binding of penetratin to GUV reported earlier [109]. In both cases, we observed small aggregates of lipids coming off the surface of GUV while the protrusion length was decreasing.

Fig. 4-3A shows representative curves of $\Delta A/A$, the fractional change of vesicle area, as a function of time, for three different concentrations of hIAPP. At 1 μM, the increase-decrease of protrusion length occurred after ~5 sec of GUV's exposure to hIAPP and then the GUV ruptured. At 0.5 μM of hIAPP, the increase-decrease occurred about 10 sec after the hIAPP exposure. At 0.05 μM hIAPP, the protrusion length steadily increased for most of the time.

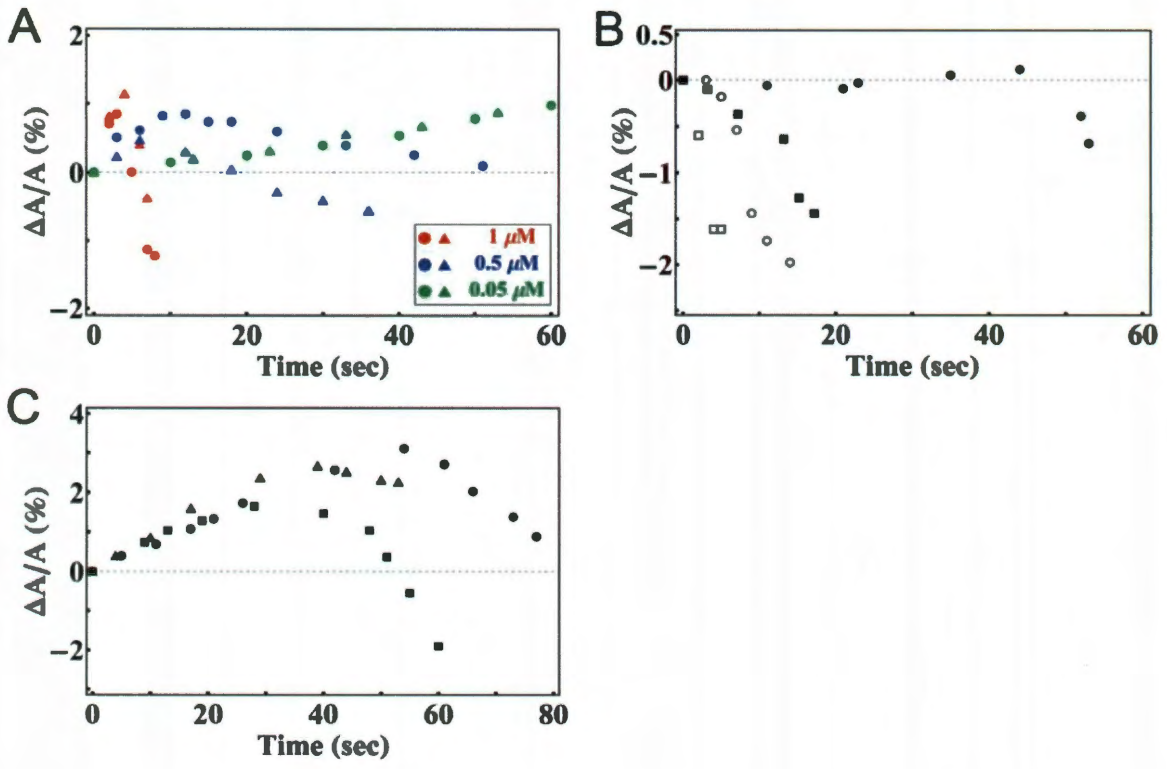

Figure 4-3 (A) GUV (7:3 DOPC/DOPG, plus 0.5 mol % Rh-DOPE) containing 200 mM sucrose exposed to three different concentrations of monomeric hIAPP in 199 mM glucose and 1 mM Tris buffer (pH 7.0). The change of protrusion length was converted to *ΔA/A* as a function of time (only two curves are shown for each concentration): 1 μM (red), 0.5 μM (blue), 0.05 μM (green) of monomeric hIAPP. (B) The experiment was performed in the same conditions as (A) except that the monomeric hIAPP was replaced by hIAPP β-fibrils at 0.25 μM. In both A and B, different symbols represent different runs. (C) GUV containing 200 mM sucrose exposed to 0.25 μM monomeric hIAPP in 199 mM sucrose and 1 mM Tris buffer (pH 7.0). The change of protrusion length is proportional to ΔA/A.

4.3.2. Leakage experiment with monomeric hIAPP

The purpose of the leakage experiment is to investigate if there is hIAPP-induced leakage from the GUV before its rupture. Free (not-aspirated) GUVs containing solution dye were first exposed to monomeric hIAPP at 0.1 μM for 5 minutes. No dye leakage was observed, but some small aggregates came off the surface from a few GUVs (same as Fig. 4-2D). When the peptide concentration was increased to 0.2 μM for the next 5 minutes and then to 0.3 μM for another 5 minutes, more aggregates were seen coming off the surface of GUVs and a few GUVs ruptured. As the peptide concentration was increased to 0.4 μM and then 0.5 μM, the rupture became more frequent. Upon rupture, the dye content of GUV leaked out instantly and the GUV disintegrated (Fig. 4-4). We have never observed gradual leakage by hIAPP. There was no leakage from the GUVs before rupture. The reaction of GUVs to monomeric hIAPP was distinctly different from the reaction of GUVs to antimicrobial peptides, such as magainin [112, 113] and melittin [111], which are known to induce pores in the membranes. Firstly, antimicrobial peptides at similar concentrations did not cause GUV disintegration. Secondly, the leakage by antimicrobial peptides was gradual and its rate changed with the peptide concentration; the smaller the concentration the slower the rate. For example, the complete leak-out time by magainin was ~1 minute at concentration ~1 μM, but lengthened to ~10 minutes as concentrations decreased to sub-μM [112].

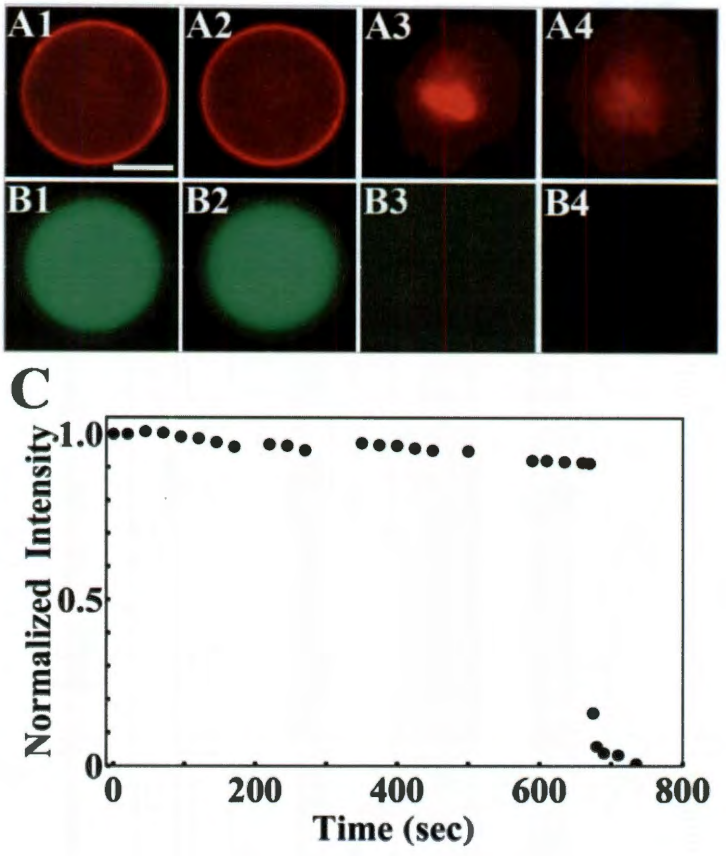

Figure 4-4 Leakage experiment. GUVs (7:3 DOPC/DOPG, plus 0.5 mol % Rh-DOPE) containing 10 μM calcein were exposed to increasing concentrations of monomeric hIAPP at 0.1, 0.2, ..., 0.5 μM in 5 minutes intervals. No gradual leakage was detected. The figure shows an example of rupture occurring at concentration 0.3 μM. The lipid dye fluorescence images A1 at 0 sec; A2 at 660 sec; A3 at 670 sec; A4 at 680 sec. The content dye fluorescence images B's were recorded ~1 sec after the corresponding lipid dye images. (C) shows the dye fluorescence intensity in time. The gradual decrease before rupture was due to photo-bleaching. The slight variations were due to varying fluorescence background. Scale bar = 20 μm.

4.3.3. GUV interaction with hIAPP fibrils

When an aspirated GUV was exposed to hIAPP fibrils, the fibrils were seen attached to the surface of GUV (it was visible because the fibrils extracted lipid molecules including dye from the bilayer). However, unlike monomeric hIAPP, fibrils did not cause an increase of the protrusion length; they only caused its decrease (Fig. 4-3B) and caused GUV rupture.

When a suspension of GUVs was injected into a suspension of hIAPP fibrils, the vesicles were disintegrated and the lipids became part of the fibril network, as shown in Fig. 4-5.

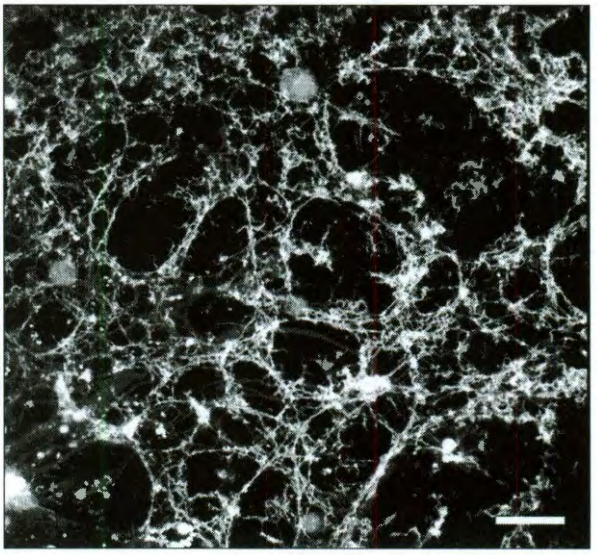

Figure 4-5 Confocal lipid-dye-fluorescence image of GUVs (7:3 DOPC/DOPG, plus 0.5 mol % Rh-DOPE) exposed to hIAPP β-fibrils (2.5 μM) in 199 mM glucose and 1 mM Tris (pH 7.0) solution. The GUVs disintegrated and lipids became part of fibril network. Scale bar =100 μm.

4.3.4. Combined results of CD and X-ray diffraction

Note that the samples were prepared in a dry condition of 50% RH (the reason will become clear). We started CD measurement from 60% RH and upward to 98% RH. Hydration above 98% would make the sample too fluid to be held vertically (necessary for both oriented CD and X-ray diffraction). DOPC/hIAPP mixtures from P/L = 1/100 to 1/20 were measured. The CD results were independent of the peptide concentration. Fig. 4-6 shows the representative result. Below ~92% RH, hIAPPs bound in lipid bilayers were in the α-helical form. According to the oriented CD spectra [26], the helical axes were parallel to the plane of the bilayers. As long as the sample was kept below 92% RH, the α-helical CD was unchanged. However, when the hydration changed to ≥ 96% RH, the CD spectrum began to change to that of β-sheet (each scan time for CD measurement including system re-setting was ~4 minutes). This change of spectrum was irreversible. If a hydrated sample was dehydrated to below 96% RH, the spectrum remained β-sheet like, independent of the hydration condition.

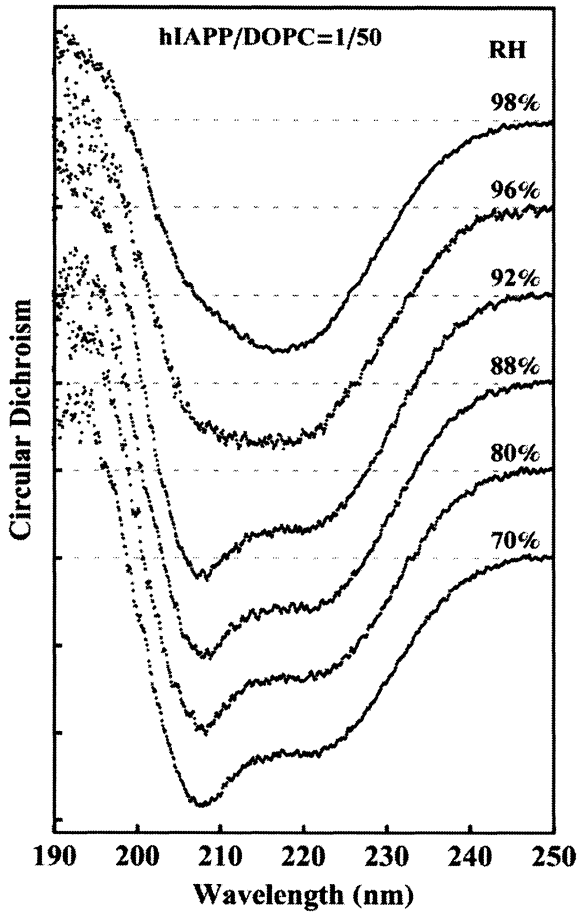

Figure 4-6 CD spectra of hIAPP in DOPC multiple bilayers at *P/L*=1/50, prepared by first co-dissolving in organic solvent and, after the solvent evaporated, hydrated to 50% RH. The CD was measured in the sequence of increasing hydrations. At and below 92% RH, hIAPP was in α-helical form. At hydrations above 96% RH, hIAPP transformed to β configurations. The configuration change is irreversible. The result is independent of *P/L* ratio from 1/100 to 1/20.

The CD samples were also measured by X-ray diffraction in the hydration sequence from 70% to 98% RH and then reversed from 98% to 70% RH. The diffraction patterns showed well-ordered bilayers in each sample of *P/L* ranged

from 1/80 to 1/30. From the reconstructed electron density profiles for the peptide-lipid bilayers, the changes of the phosphate to phosphate distance across the bilayer (PtP) are shown in Fig. 4-7. From the CD results, we know that the peptides were in α-helical configuration during the hydration sequence from 70% to 92% RH. But once the sample was hydrated to 98% RH, the peptides turned into β-sheet configuration and remained in that configuration when the sample was once again dehydrated. Fig. 4-7A shows that the thickness of pure DOPC was reversible by the hydration-dehydration cycle, but not for the lipid bilayers containing hIAPP. Once hIAPP turned into β-configurations, the bilayer thickness at full hydration became the same as pure lipid. In fact the electron density profiles obtained from the multilayers containing hIAPP in the β form are identical to that of pure lipid bilayers (Fig. 4-7B). Clearly hIAPP molecules in the β form were not within the lipid bilayers, otherwise the bilayer profiles would have been altered from the free bilayer form. The values of PtP at 92% RH are plotted as a function of *P/L* in Fig. 4-7C, showing that when the bound hIAPP was in the α-helical form, the bilayer thickness was reduced in proportion to *P/L*. Membrane thinning in proportion to *P/L* implies that the peptide in the α-helical form was bound within the headgroup region [58, 63, 65, 109].

Many independent experiments [18, 96, 98] have shown that monomeric hIAPPs bind to lipid vesicles initially in the α-helical form, and then convert to β-configurations. Our OCD and X-ray experiments with multilamellar samples are too slow to measure this transitional α-helical state in full hydration. We trapped α-

helical hIAPP in dry lipid bilayers. But by the time the samples were hydrated and measured (taking ~5 minutes), the peptide had already converted to β-configurations and exited from the headgroup region.

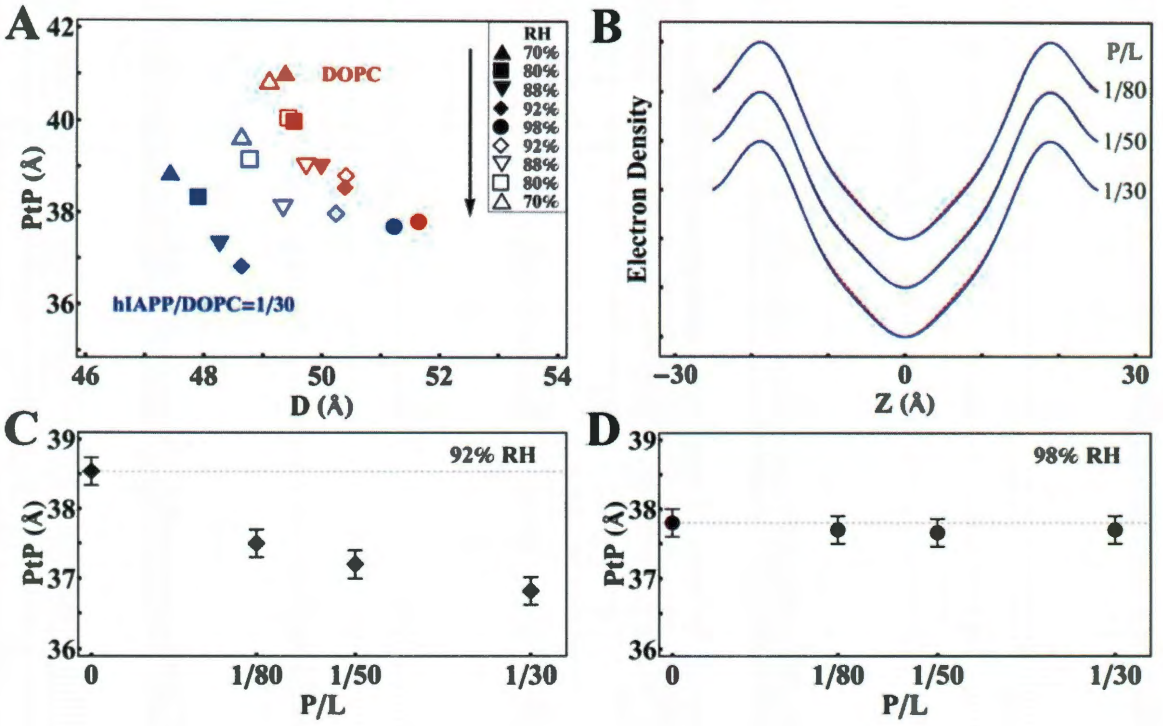

Figure 4-7 The CD samples (Fig. 4-6) were measured by X-ray diffraction. (A) The phosphate-to-phosphate distance (PtP) of the bilayer electron density profiles obtained from DOPC multilayers containing hIAPP (blue symbols) compared with that of pure DOPC (red symbols) in the sequence of hydration-dehydration cycle indicated in the inset. (B) The electron density profiles of DOPC multilayers containing hIAPP (blue line) compared with that of pure DOPC (red line; mostly overlaying the blue line) at 98% RH. The profiles are the same within experimental resolution. (C) PtP of DOPC/hIAPP changes with *P/L* at 92% RH (D) PtP of DOPC/hIAPP changes with *P/L* at 98% RH.

4.4. Discussion

The new structural information obtained from our experiments is that the β-aggregates of hIAPP bind on the surface of lipid bilayers; they do not penetrate into the bilayer structure. This is true even when the β-aggregates originated from α-helical hIAPPs bound inside the headgroup region of lipid bilayer. This behavior of hIAPP is identical to the previous finding with the amyloidogenic peptide penetratin [109]. Thus it could be a common pattern of interaction between amyloid-forming peptides and lipid bilayers, i.e., the peptides binds as helices inside the headgroup region of the bilayer, but once the peptides convert to β-aggregates, they bind on the aqueous surface of the bilayer.

The GUV experiments with monomeric hIAPP imply that there is a threshold bound-peptide/lipid ratio, below which the bound peptide does not convert to β-aggregates. This behavior of hIAPP is also similar to penetratin. Such a threshold is important because the binding of hIAPP does not damage the lipid bilayer until the peptide converts into β-aggregates.

4.4.1. Interaction of hIAPP β-fibrils with lipid bilayers

Binding of hIAPP β-fibrils to lipid vesicles was observed in two ways. When an aspirated GUV was exposed to hIAPP β-fibrils, the peptide binding did not cause a membrane expansion—no protrusion length increase, consistent with surface binding. Instead, the GUV protrusion length quickly decreased and the GUV

ruptured (Fig. 4-3B). On the other hand, if lipid vesicles were dispersed into a β-fibrils suspension, vesicles and lipids were seen attached to the fibrils and become part of the fibril aggregates. We stress that hIAPP β-fibrils bind to both neutral (DOPC) and anionic lipids (7:3 DOPC/DOPG) and that the same binding phenomena were observed during the growth of β-fibrils as well as with pre-formed β-fibrils. This is contrary to the observation by Engel et al. [108] who reported interactions only during the growth of fibrils.

Eisenberg and colleagues [92, 93] have resolved the crystalline structures of β-amyloid formed by a small peptide GNNQQNY. The universal cross-β structure for β-amyloids has three levels of organization: The first is the alignment of the peptide molecules to form a β–sheet; the second is the self-complementation of two sheets, forming the pair-of-sheets structure with a dry interface; in the third level, pair-of sheets interact to form a fibril. For an extended peptide like hIAPP, the organization at each level is bound to be imperfect (unlike the small peptide GNNQQNY), namely, there will be unpaired (positive) charges and uncovered hydrophobic regions exposed on the surface of the fibrils. It is well known that multivalent cations adsorb to lipid bilayers of both zwitterionic and acidic headgroups [114]. Therefore, it is not surprising that the positive charges on the surface of hIAPP β-fibrils bind to the surface of lipid bilayers. It is also not surprising that lipid molecules bind to the hydrophobic regions of the fibril surface.

Given such deleterious effects on lipid bilayers, why were there no interactions between hIAPP β-fibrils and cell membranes in culture [16, 83]? We speculate that perhaps the β-fibrils formed in solution cannot penetrate the carbohydrate layer (glycocalyx) [115] that covers the cell surface, so the fibrils do not come into contact with plasma membranes.

4.4.2. Interaction of hIAPP monomers with lipid bilayers

Monomers of hIAPP in solution bind to both neutral (zwitterionic) and anionic lipid bilayers. As expected, the binding affinity to the latter is stronger. In our experiments, pure lipid GUVs were introduced into a peptide solution at t = 0. Thus the bound-peptide/lipid ratio, *P/L*, increased with time. In all concentrations, the initial binding expanded the membrane area without causing molecular leakage. At peptide concentration $\lesssim 0.05$ μM, the GUV remained in this condition within our experimental time. No aggregates were observed on the GUV surface and no damage to lipid bilayers occurred. This clearly implies that before *P/L* reaches a threshold value, the bound peptides do not transform to β-aggregates. But the exact value of the threshold *P/L* is too small (< 1/100) to be measured by the multilayer experiments. In contrast, the threshold *P/L* for penetratin has been measured accurately by the multilayer experiments: four different thresholds, between 1/65 to 1/20, in four different lipids [109].

When an aspirated GUV was exposed to monomeric hIAPP at concentrations $\gtrsim 0.5$ μM, the initial membrane expansion reached a limit and then the expansion

was reversed. During the decrease of protrusion length, we observed small aggregates that included lipid dye appeared on the membrane surface but there was no molecular leakage (the vesicle phase contrast remained constant). Eventually the GUV ruptured.

Thus we can summarize the physical process of interaction between monomeric hIAPP with lipid bilayers as follows. HIAPP spontaneously binds to lipid bilayers. If the bound *P/L* is below a certain threshold value, the binding causes a membrane expansion but otherwise causes no leakage or damage. However if the *P/L* exceeds the threshold value, the bound peptides convert to β-aggregates which exit from the bilayer and bind on the bilayer surface. The process of conversion to the β-aggregates probably extracts lipid molecules from the bilayer. As long as the β-aggregates are sufficiently small, the extraction of lipid does not cause molecular leakage. However small β-aggregates seed the formation of fibrils, as demonstrated by the Jarrett-Lansbury model [38]. The large size fibrils eventually rupture the lipid bilayer via electrostatic and hydrophobic interactions.

Our observation at high concentrations of monomeric hIAPP essentially agrees with Engel et al. [108]. Many previous investigations have reported ion conduction caused by hIAPP monomers while detected no molecular leakage [16, 17, 90, 102-104]. This phenomenon may be correlated to the extraction of lipid molecules from the bilayer during the hIAPP's conversion to β-aggregates. It has been reported that defects of a lipid bilayer allow ion conduction, for example near the fluid-gel phase transition point, but no molecular leakage [116].

Finally, as stated above, we speculate that β-fibrils cannot pass through the glycocalyx to reach the plasma membranes of cells, but we assume that hIAPP monomers can. The latter assumption is based on the observation that antimicrobial peptides (which are monomeric in solution and many of them are of similar size of hIAPP) can readily reach the plasma membranes [117]. Based on our knowledge of how hIAPP interacts with lipid bilayers, the soluble monomers are the most likely form of hIAPP that could affect cell membranes in culture. The possible damage strongly depends on the peptide concentration. The damage caused by high concentrations of hIAPP may not occur in low concentrations.

Chapter 5

Transmembrane Pores formed by Human Antimicrobial Peptide LL-37

5.1. Introduction

Human antimicrobial peptide LL-37 is the most studied member of cathelicidins [118], which are a major family of mammalian proteins that play varieties of roles in host defense and inflammation [118-122]. It is remarkable, considering its small size and relatively simple structure, that LL-37 contains all the necessary information to exert and perform multiple diverse functions, including antimicrobial activity, chemotactic effects that contribute to immune responses, release of inflammatory mediators, transcriptional responses, wound healing and others [118, 123]. Most of these functions require specific molecular interactions, except for its direct antimicrobial activity. Like all other antimicrobial peptides (AMPs) [49], LL-37 is water soluble, but spontaneously binds to bacterial LPS and

lipid bilayers [119], and permeabilizes microbial membranes, which then leads to rapid cell death [119, 124]. The question is how does LL-37 permeabilize membranes? Previous experiments have found LL-37 bound to lipid bilayers in the α-helical form [125] with the helical axis lying parallel to the plane of bilayer [124, 126]. Based on this finding, it is widely believed that LL-37 does not form pores in membranes, rather it permeabilizes or destroying membranes by a "nonpore carpet mechanism" [124, 125, 127].

We report here the discovery of transmembrane pores induced by LL-37. The pore formation coincided with the detection of LL-37's helical axis oriented approximately normal to the plane of the membranes. The water channel of the detected pores ranged from 23 to 33 Å in radius, depending on the peptide/lipid ratio. We found the reason that explained why previous investigations did not observe LL-37 inserted in membranes. In all peptide orientation measurements whether by solid state NMR [126] or by polarized FTIR [124], the membranes were prepared in multilayers. In the commonly prepared membrane multilayers, the periodic spacing of bilayers (the D spacing) is up to ~52 Å at full hydration. Under such conditions, our measurements agreed with the previous studies [124, 127] that LL-37 helices were in the plane of the bilayers and no pores were detected. However, we found that LL-37 helices were oriented approximately normal to the plane of the bilayers when the D spacing exceeded ~70 Å. For multilayers this was a condition with excessive water, a swollen state. It was as if the D spacing needed to substantially exceed the length of the peptide (~37×1.5 or 55 Å, assuming a helix

[125]) in order to find LL-37 inserted in the membranes. Multilayers in swollen states were investigated by X-ray diffraction to make sure that the lipid/peptide bilayers were in the lamellar phase. The thermal fluctuations of bilayers in swollen lamellar states are of theoretical interest in statistical physics [128, 129]. Therefore they have been extensively analyzed by X-ray diffraction [129-131] and are now well understood. We used the method of oriented circular dichroism [26] to measure the peptide orientation in swollen states and used neutron in-plane scattering to detect and measure the transmembrane pores induced by LL-37. The results were correlated with the kinetic effect of LL-37 binding to giant unilamellar vesicles (GUVs). We conclude that the membrane permeabilization mechanism of LL-37 is consistent with the two-state model exhibited by other well studied pore forming peptides [22, 111].

5.2. Materials and Methods

5.2.1. Materials

Human LL-37 (LLGDF FRKSK EKIGK EFKRI VQRIK DFLRN LVPRT ES) was synthesized by GenScript USA Inc. (Piscataway, NJ) to >95% purity by HPLC. DOPC and Rh-DOPE were purchased from Avanti Polar Lipids. Calcein was purchased from Invitrogen (Carlsbad, CA). Other chemicals were purchased from Sigma-Aldrich and were used without further purification. All experiments were performed at room temperature ~25°C.

5.2.2. Stacked Membrane

Preparation of open stacked membranes has been described previously [63]. Briefly a mixture of LL-37 and DOPC (in the peptide/lipid molar ratio P/L = 1/100, 1/80, or 1/50) in organic solvent (1:1 (v/v) chloroform and tetrafluoroethylene) was directly deposited on a cleaned quartz plate and dried in vacuum before hydrated by water vapor (referred to as open samples, each with 0.2-0.4 mg of lipid). X-ray diffraction indicated that the multiple bilayers were well aligned parallel to the substrate. The sample was kept in a temperature-humidity chamber as described in [69]. Once the humidity sensor reached a new hydration level, the sample equilibration time was at most a couple of minutes (this was seen by continuous X-ray scanning). For data acquisition, we allowed at least 10 minutes for equilibration.

For neutron experiments which required a large amount of sample (~30 mg of lipid), we used stacked membranes sandwiched between two quartz plates as described in [24]. Briefly the peptide-lipid mixture was first lyophilized and then hydrated by 100% RH water vapor over night to a gel-like texture at ~35°C. The gel-like mixture was spread on one quartz plate and then covered by a second plate (referred to as sandwiched samples at full hydration). For swollen state samples, an amount of water equal to the lipid in weight was added to the fully hydrated peptide-lipid mixture and then covered by a second substrate and equilibrated for 1 hour or longer (referred to as sandwiched samples in a swollen state). Double substrates have proven to be capable of aligning thick lipid multilayers [23]. The

membrane alignment in a sandwiched sample can be examined by polarized microscopy [23, 24] or neutron diffraction, or by X-ray diffraction if one substrate was replaced by a mylar sheet.

5.2.3. OCD

CD spectra were measured in a Jasco J-810 spectropolarimeter. To measure oriented circular dichroism (OCD), the substrates of stacked membranes were oriented normal to the incident light [26]. The detailed analysis of OCD for α-helices, including its experimental verification as well as its limitation, is given in [26]. The technique has also been independently confirmed by other laboratories, e.g., [132-134].

5.2.4. Neutron In-plane Scattering

Neutron experiment was performed at the HFIR Bio-SANS CG-3 station [25] in the Oak Ridge National Laboratory. The small angle scattering beamline was equipped with a 1 x 1 m area detector (5.1 x 5.1 mm^2 pixels) with adjustable sample to detector distance 1-15 m. The neutron wavelength was 6 Å with $\Delta\lambda/\lambda \sim 15\%$. The detector was positioned to record the q range from 0.013 to 0.3 $Å^{-1}$. Sandwiched samples were sealed in an aluminum holder that provided a beam path of 16 mm in diameter. The scattering data were collected for 10-30 minutes per sample. More technical details can be found in [24].

5.2.5. X-ray Lamellar Scattering

The equipment, experimental procedure and data analysis for X-ray lamellar diffraction by multilayers have been described in Section **3.2.2**. and in many of previous studies, e.g., [109]. The open sample was housed in a temperature-humidity chamber where the hydration level of the sample was controlled by the relative humidity (RH) of water vapor. The substrate orientation was vertical. ω-2θ scans were recorded at a humidity level up to ~100% RH and at a few lower RH values. The hydration dependence was used to determine the diffraction phases by the swelling method. The diffraction patterns at RH higher than ~98% suffered undulation damping. Thus the patterns at ~98% RH were used to construct the electron density profiles across the bilayer.

5.2.6. Grazing-angle X-ray Scattering

The equipment and experimental procedure for grazing angle scattering was described in [135]. Swollen samples were sandwiched between a Si wafer and a mylar sheet. The sample was held horizontally and then tilted $\leq 0.5^0$ for scanning. X-ray from a point source of Cu K_α radiation (operating at 35 mA/40kV) was double-focused (by a pair of bent mirrors) horizontally at the sample. The scattering pattern was recorded by a CCD area detector (Gemstar HS 75, Photonic Science Ltd. E. Sussex, UK). The beam center and the sample-to-detector distance were determined by powder scattering from Ag-behenate.

5.2.7. GUV Experiment

GUVs of DOPC plus 0.5 mole % Rh-DOPE were produced in 200 mM sucrose solution by electroformation [57]. The osmolality of every solution used in the GUV experiment was measured by a Wescor model 5520 dew-point Osmometer. Micropipettes and the glass walls of experimental chambers were coated with 1% bovine serum albumin in order to neutralize the charge on the bare glass surface and then washed extensively with water. All GUV experiments were performed at room temperature ~25°C.

For the leakage experiment, the solution in the GUV production chamber also contained 10 μM calcein. A small amount of the GUV suspension was transferred to an observation chamber containing 190 mM glucose, 10 mM HEPES at pH 7.0 and 5 μM LL-37. The GUVs settled at the bottom due to the density differential and were observed under an Olympus microscope model IX81 and recorded by a Hamamatsu Photonics digital CCD Camera C10600-10B. The content leakage was monitored by calcein fluorescence. At the end of the leakage, we used the lipid dye image to inspect the effect on the vesicle membrane.

For aspiration experiments, a GUV was aspirated by a micropipette with a small constant sucking pressure (~100 Pa producing a membrane tension ~0.4 mN/m) and transferred, via a transfer pipette [57], to an observation chamber containing 190 mM glucose, 10 mM HEPES at pH 7.0 and 0.5 μM LL-37. Equi-osmolality between the inside and outside of the GUV was maintained throughout

the experiment. The experiment was recorded by fluorescence image using a Photometrics coolSNAP HQ2 camera. The technical details of aspiration experiment can be found in [57].

5.3. Results and Analysis

5.3.1. OCD of LL-37 Embedded in Stacked Membrane

The open sample was kept in a temperature-humidity chamber, in which the sample and a water source had separate temperature controls [69]. OCD was measured with the sample substrate oriented vertically, so that the UV beam for circular dichroism incident perpendicularly to the plane of bilayers [26]. By varying the temperature of the water source from below up to the same as the sample temperature (20°C), the humidity at the sample (measured by a humidity sensor in the vicinity of the sample) varied from ~70% to ~100% RH. In this range of RH, the spectrum was independent of RH (Fig. 5-1A). The OCD indicated that peptide helices were oriented approximately parallel to the plane of the bilayers [26]. This result is consistent with the previous measurements by solid state NMR [126] and by polarized FTIR [124]. X-ray diffraction of the sample showed that the D spacing increased from 47 Å at ~70% RH to 52 Å at ~100% RH (Fig. 5-2A). The Bragg peaks at ~100% RH were broadened and diminished at high orders, indicating bilayer undulations in water [72, 128].

We then set the water temperature 1° to 2° above the sample temperature. This caused water vapor to condense on the sample. As water visibly condensed on the sample, the surface of the sample slowly slid downward and out of the beam path (because the substrate was vertical). In the meantime, the OCD changed its shape with an overall decreasing amplitude (Fig. 5-1A), indicating a decreasing amount of sample in the beam path, but an increasing fraction of the remaining peptide helices had changed to perpendicular to the plane of the bilayers. Eventually the OCD changed into a spectrum corresponding to all helices oriented approximately normal to the plane of the bilayers [26]. At that moment, the humidity chamber was open to expose the sample to the room air (~50% RH) and the sample was held horizontally for ~10 minutes. That stopped the sample flowing, and the OCD changed back to the original spectrum of all helices parallel to membranes, but the amplitude was smaller than the original due to the partial loss of the sample. From the last two spectra, we obtained the two mutually normalized OCD spectra of LL-37 helices, one oriented approximately parallel (the S spectrum) and one approximately perpendicular (the I spectrum) to the plane of the membranes (Fig. 5-1B). The same experiment was repeated several times for each of P/L = 1/80 and 1/50 samples, with the same result.

The sandwiched samples used in neutron experiments were too thick (~30 mg of lipid) for CD measurement. Thus we reproduced sandwiched samples for CD measurement with a smaller amount of lyophilized peptide-lipid mixture (~0.5 mg of lipid). Two different hydration conditions were used. In one case, the mixture

was hydrated by ~100% RH, and then the measured OCD was the S spectrum, consistent with open samples hydrated by ~100% RH. In another case (the swollen state), the lyophilized peptide-lipid mixture was equilibrated with the same weight of water as the amount of lipid. However, to avoid air bubbles in the sandwiched sample, the second cover inevitably applied pressure and squeezed out a small but unknown amount of water from the holder, despite the use of a spacer between the two substrates. The exact amount of water in a swollen state was difficult to reproduce, but the water content was nevertheless precisely measured by its D spacing. In all swollen cases, the measured OCD was a linear combination of the S and I spectra [26], indicating that 30% to 60% of LL-37 were oriented perpendicular to the bilayers (one example shown in Fig. 5-1B). It appeared that as long as the sample was in a swollen state, a substantial fraction of LL-37 peptides were oriented normal to the bilayers.

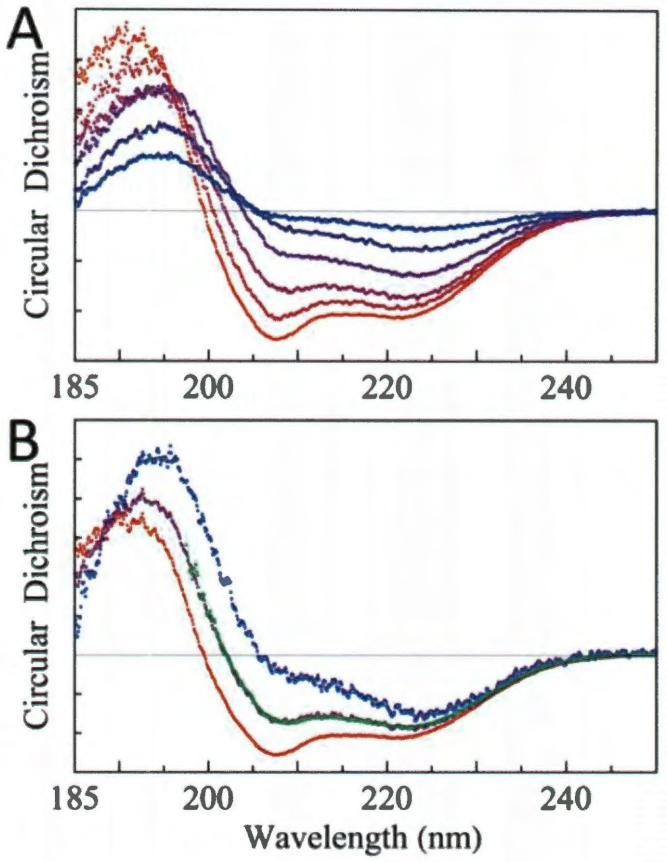

Figure 5-1 Oriented circular dichroism (OCD). (A) The bottom red spectrum is the OCD of an open sample of P/L = 1/50, unchanged from 50% to 100% RH. As excessive water condensed on the sample, the spectrum gradually changed in time from bottom to top, while the amount of sample in the CD beam path was decreasing because the surface of the sample slowly slid downward. It took 40 minutes of continuous OCD scanning from the red to the blue spectrum. The scan time for each spectrum was ~4 minutes. Ten spectra were taken but for clarity only 5 were shown. (B) At the appearance of the top blue spectrum in (A) which was rescaled in (B), the sample was open to 50% RH and held horizontally for ~10 minutes--this made the sample stopped flowing and the spectrum turned to the bottom red curve. The blue and red spectra were from the same amount of sample; blue is the I spectrum for helices normal to the bilayers and red is the S spectrum for helices parallel to the bilayers. The green spectrum was obtained from a sandwiched sample in a swollen state, fit by a linear combination of the I and S spectra: 0.4 *I*+0.6 *S* (purple line), indicating 40% of the helices were oriented normal to the bilayers.

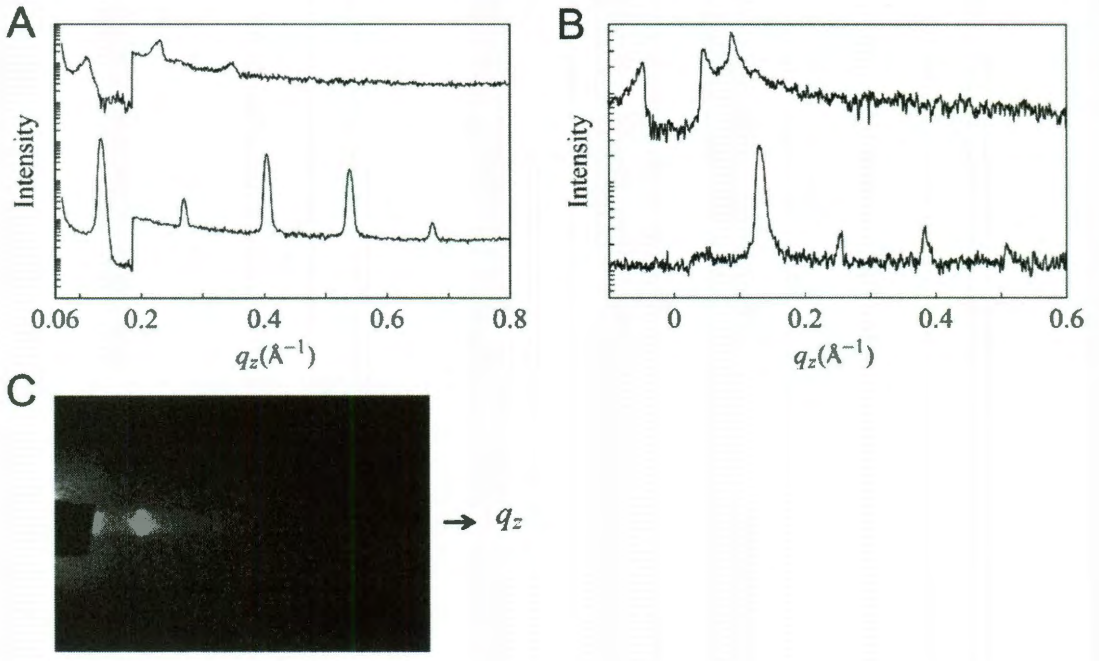

Figure 5-2 (A) X-ray lamellar diffraction by ω-2θ scan from an open sample of P/L = 1/50 equilibrating at 98% RH (bottom) and at 100% RH (top) (an attenuator below q = 0.19 Å^{-1}). Note that at 100% RH, the peaks were strongly damped by layer undulations. (B) X-ray grazing angle scattering from an open sample of P/L = 1/50 equilibrated at 60% RH (bottom) and (top) in a swollen state (covered by a mylar sheet; also an attenuator below q = 0.04 Å^{-1}). Note that in the swollen state, the first order peak has the characteristic power-law line shape as predicted by the Caillé theory due to layer undulations in the swollen lamella. (C) The grazing angle scattering from the swollen lamella (B) recorded on the CCD detector which was oriented with the z-axis vertically up. The beam center was at the base line. The rectangular diffraction peak image was the shape of the X-ray beam cross section. The intensity profile along the z-axis was shown in (B) top.

Solution CD studies on LL-37 showed that the peptide was a random coil in water containing no salt (as in our stacked membranes preparation) but changed to α-helical upon the introduction of lipid vesicles [119, 126, 136]. Thus it is clear that the LL-37 peptides in our stacked membranes were membrane-bound whether in non-swollen or swollen states, since the CD spectra were clearly that of α-helices. One important question is how might the bilayers undulations in the swollen states have affected the orientation of the peptide? Firstly the swollen state was examined by X-ray diffraction (Fig. 5-2B and 5-2C). In this case the cover for the sandwiched sample was a mylar sheet transparent to X-ray. Fig. 5-2C shows the scattering pattern of a lamellar phase (D spacing ~71 Å) where the first order peak has the characteristic power-law line shape (Fig. 5-2B top) as predicted by the Caillé theory [128-131]. The undulations of bilayers in swollen lamellar phase are well understood. The spectrum of out-of-plane undulations of bilayers is long-wavelength dominated, thus despite the enhanced fluctuations by swelling, the dominant tilt angles are still small [128-131]. The fact that the I spectrum was measured is a proof that the bilayers were well aligned in average and it could only be explained by the majority of helices being approximately normal to the plane of the lamellar phase [26].

To prove that the I and 40% I spectra in Fig. 5-1B could not be the results of bilayer undulations with surface bound helices, imagine that the bilayers became vesicles (with the helices on the bilayer surface), then the CD spectrum would be the familiar CD of helices in solution, which is (1/3)I +(2/3)S [26]. Thus if helices were

on the bilayer surface, even the worst-case perturbation of bilayers could not produce the 40% I spectrum, not to mention the I spectrum.

According to the NMR study of LL-37 adsorbed on a lipid micelle [125], the membrane-bound LL-37 is largely α-helical with a bend in the helical axis at K12, which is similar to the melittin helix [137] or the alamethicin helix [76] both of which exhibited the S and I states in membranes [26, 29]. Oriented NMR was performed on LL-37 in DMPC at P/L = 1/50 in stacked membranes prepared with 30 mol of H_2O per mole of lipid/peptide, but the exact hydration condition was unknown (most likely not in swollen states, because the authors would have noted the sample flow problem) [126]. The authors concluded that the α-helix is oriented parallel to the surface of the bilayer (the measured $\sigma_{33} \sim 10°$-$25°$ relative to the surface). The first investigation on the LL-37 orientation was by Oren et al. [124] using the method of polarized Four-transform infrared spectroscopy (FTIR) on stacked membranes of LL-37 in PC/cholesterol and PC/PG at P/L ~ 1/70, hydrated with saturated D_2O vapor. The measured order parameter was consistent with helical axes parallel to the membrane surface.

CD has broad spectra, therefore is a low resolution spectroscopy. It is an appropriate spectroscopy for fluid lipid systems where structures such as orientation are subject to significant fluctuations therefore intrinsically of low resolution, as shown by the result of solid state NMR measurement [126]. Within the spectral resolution the I spectrum is consistent with the great majority of helices approximately oriented normal to the plane of the membranes and the S spectrum is

consistent with the great majority approximately oriented parallel to the plane of the membranes, as dictated by the Moffitt theory [26]. The exact orientations of the I and S states are not important to the conclusion. What is significant is that we have detected two distinct orientation states, one approximately parallel and one approximately normal to the plane of membranes, and, furthermore, the detection of the I state was coincidental with the detection of pores and no pores were detected in the S state (see neutron section below). As pointed out in [26], OCD cannot distinguish whether an intermediate state between I and S (such as the 40%I spectrum in Fig. 5-1B) is due to uniformly tilted helices or due to a mixture of two distinct orientation states. For instance, the series of intermediate states in Fig. 5-1A could be interpreted as the helices uniformly stabilized in a series of tilt angles. But this is physically unlikely and has never been observed in any peptide. It is more reasonable to assume that the intermediate spectrum in Fig. 5-1B represents a mixture of helices in the S and I states.

5.3.2. Neutron In-plane Scattering

This technique makes use of the large difference (contrast) between the neutron scattering by hydrogen and by deuterium. The water in our multilayer samples was exchanged to D_2O by exposing the samples to D_2O vapor. Then, in the plane, the bilayers had a uniform scattering density except for the D_2O channels in the transmembrane pores, as long as the magnitude of the scattering vector was less than $2\pi/(4.5\text{Å})$ (the denominator is the size of the cross section of a hydrocarbon chain) [24]. Thus if peptides formed pores in the membrane, neutron in-plane

scattering would detect a collection of D_2O channels representing the pores diffusing in a two-dimensional uniform background [24].

We used a stack of 3 sandwiched samples, each containing 8-10 mg of lipid, for neutron scattering. The substrates were aligned perpendicularly to the incident neutron beam. The scattering vector q at small angle scattering ($q < 0.3$ Å^{-1}) was essentially in the plane of the aligned multilayers. Each sample was scanned in three conditions in the following sequence: (1) the sample was equilibrated with 100% RH D_2O vapor, (2) the sample was equilibrated in a swollen condition with 1:1 (w/w) D_2O to lipid ratio, and (3) the sample was equilibrated in a swollen condition with H_2O. The results of P/L = 1/50 are shown in Fig. 5-3. The sample in the first condition showed only a lamellar peak at $q = 0.124$ Å^{-1} corresponding to a D spacing of 51 Å, the same as open samples measured by X-ray in the same hydration condition. The lamellar peak was due to oily streak defects in multilayers [23, 24]. The absence of other scattering signal indicated no pores in the bilayers. In the second condition, there was a broad peak at 0.041 Å^{-1} and a shoulder peak at 0.085 Å^{-1}. The shoulder peak which also appeared in other samples in swollen conditions with D_2O, was a lamellar peak due to oily streak detects corresponding to a D spacing of 74 Å. Both peaks disappeared in the third condition.

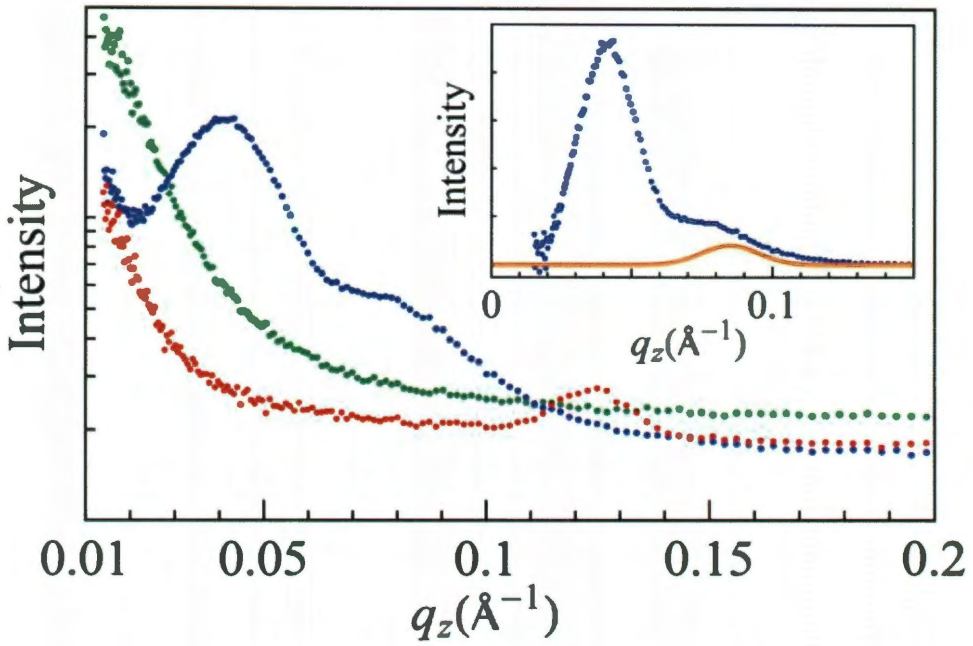

Figure 5-3 Neutron in-plane scattering of a sandwiched sample of P/L = 1/50 in three conditions: equilibrated at 100% RH D_2O (red), equilibrated with excessive D_2O in a swollen state (blue), and equili-brated with excessive H_2O in a swollen state (green). Inset: Obtainedfrom the circles curve after removing the background (the empty sample cell). The shoulder peak was fit with a Gaussian curve (orange) at 0.085 $Å^{-1}$.

The broad peak at 0.041 $Å^{-1}$ was due to the presence of D_2O columns in the membranes, therefore it implied the presence of transmembrane pores. The peak disappeared upon exchange to H_2O as expected, since H_2O columns in membranes had no significant contrast against the lipid background by neutron scattering. Similar neutron in-plane scattering peaks induced by magainin, alamethicin, protegrin and melittin had been thoroughly studied previously [24, 138-140]. It

was demonstrated that in some lipids these peaks could be crystallized into a rhombohedral lattice [135], therefore amenable to X-ray diffraction analysis [21, 141]. The structures revealed by diffraction were indeed transmembrane pores [21, 141].

The in-plane scattering intensity I(q) is theoretically expressed as $I(q) = A|F(q)|^2 S(q)$, where F(q) is the form factor, i.e., the scattering amplitude of an individual pore; $S(q) = < \sum_{i,j} \exp[-i\boldsymbol{q} \cdot (\boldsymbol{r}_i - \boldsymbol{r}_j)] > / N$ is the structure factor, where $\boldsymbol{r}_i$ is the position of the center of a pore in the plane of bilayer, < > represents the ensemble average, N is the total number of pores; and A is the normalization constant. The analysis of neutron in-plane scattering has been described in detail in previous study [24], which showed that F(q) is dominated by the scattering amplitude of the D_2O channel inside the pore, therefore is essentially determined by the radius of the cylindrical D_2O channel. S(q) can be simulated by randomly distributed disks on a plane representing pores in the bilayer. The peak comes from the interference due to non-overlapping between disks. Therefore the diameter of the disk represents the collision distance between two pores in the membrane. The fit to the data was carried out by adjusting three independent parameters: (1) the disk diameter is essentially determined by the position of the peak, (2) the fit to the left side of the peak is essentially determined by the density of the disks in the plane which is the density of the pores in the membrane, and (3) the fit to the right side of the peak is essentially determined by the form factor (q) or the radius of the water channel.

The results by minimum χ^2 fit are shown in Fig. 5-4. At P/L = 1/50, the water channel radius is 33 Å and the collision distance, i.e., the closest approach between two pores, is 130 Å. At P/L = 1/100, the water channel radius is 23 Å and the collision distance is 82 Å. In comparison, the water channels of magainin pores are 15-25 Å in radius, with collision distance 70-84 Å [138]. The melittin pores, in one measurement, had a water channel of radius 21 Å and collision distance 77 Å [29]. The previous results, particularly that of magainin, were obtained by repeated measurements in different P/L and in different lipid compositions [138, 140]. Therefore, the range of pore radius 23-33 Å for LL-37 measured here should be regarded as a minimum range. Perhaps not surprisingly the pores induced by LL-37 are larger than those by smaller peptides magainin or melittin. The number of LL-37 peptides participating in each pore was ~5, calculated by assuming that all peptides were in pore formation. The precise number was unknown because it depended on the fraction of the peptides oriented normal to the bilayers (as noted above the neutron samples could not be directly measured by OCD). In comparison, magainin pores were estimated to contain 4 - 7 peptides in each pore [138].

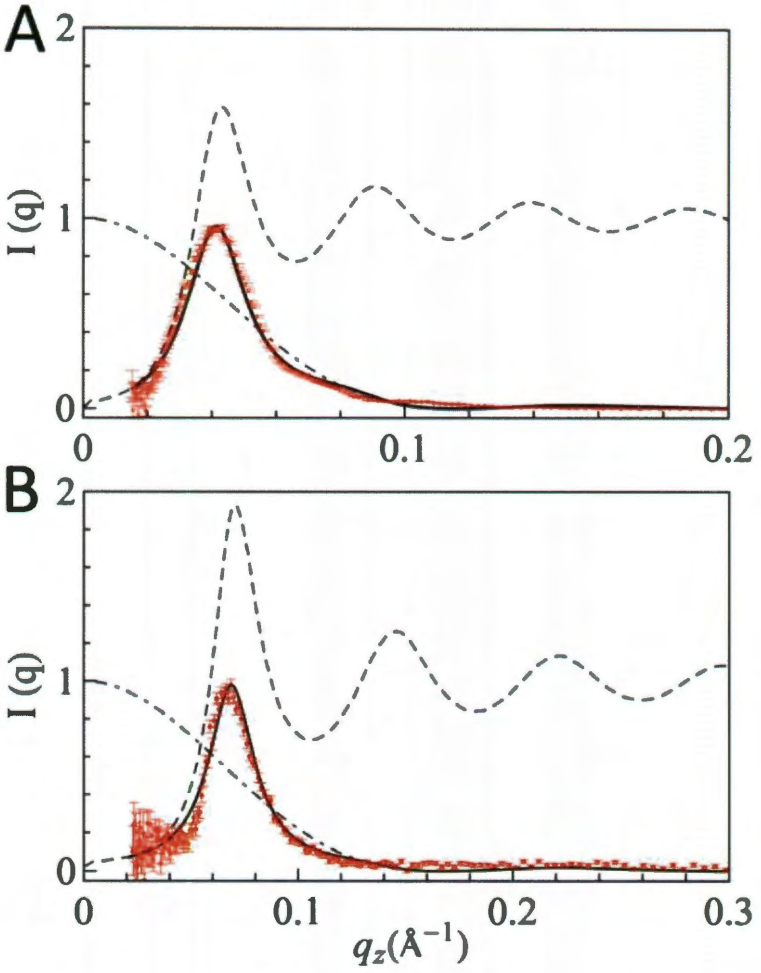

Figure 5-4 Analysis of neutron in-plane scattering, (A) P/L = 1/50 (data from Fig. 5-3 inset, after subtracting the shoulder peak); (B) P/L = 1/100. Dash-dot curve is $|F(q)|^2$, dash curve $S(q)$, and the solid curve is the minimum χ^2 fit.

5.3.3. X-ray Lamellar Scattering in Nonswellon Conditions

X-ray diffraction was used to investigate the condition of lipid bilayers in stacked membranes for both the swollen states (see the OCD section) and non-

swollen states. In the non-swollen states, LL-37 helices were parallel to the bilayers as determined by OCD. We performed X-ray diffraction to investigate the effect of surface-bound LL-37 on the lipid bilayers. The electron density profiles of DOPC bilayers containing LL-37 at P/L = 0, 1/80 and 1/50 were constructed from the lamellar diffraction patterns obtained at ~98% RH (Fig. 5-5). The profile peaks at the phosphate group on both sides of bilayer. Thus the peak-to-peak distance (PtP) can be used to measure the changes of the bilayer thickness (as explained in [109] the peptides do not contribute to the X-ray profile). As in previous measurements with various peptides in their surface bound states [22], there was membrane thinning linearly proportional to P/L (Fig. 5-5). This membrane thinning effect by surface bound peptides has also been detected by other techniques, such as atomic force microscopy on supported lipid bilayers [142] and small angle X-ray scattering on lipid vesicles [143]. Our result is analyzed as follows. Let A_P be the monolayer area expansion per peptide embedded in the headgroup region of the monolayer, and A_L the cross section area per lipid. Then the fractional area expansion of the lipid monolayer (or of the lipid bilayer) is $\Delta A/A = (P/L)(A_P/A_L)$. From the chain volume conservation, we have $\Delta A/A = -\Delta h/h = (P/L)(A_P/A_L)$, where the hydrocarbon thickness h is directly obtained from PtP by $h \approx$ PtP −10 Å [58]. Therefore from the slope of the membrane thinning data (Fig. 5-5), we obtained the value of A_P = 309 Å^2. This is not the along-the-axis cross section of the LL-37 helix. The peptide binding involves release of water molecules from the headgroup region that makes A_P smaller than the physical size of the peptide [74].

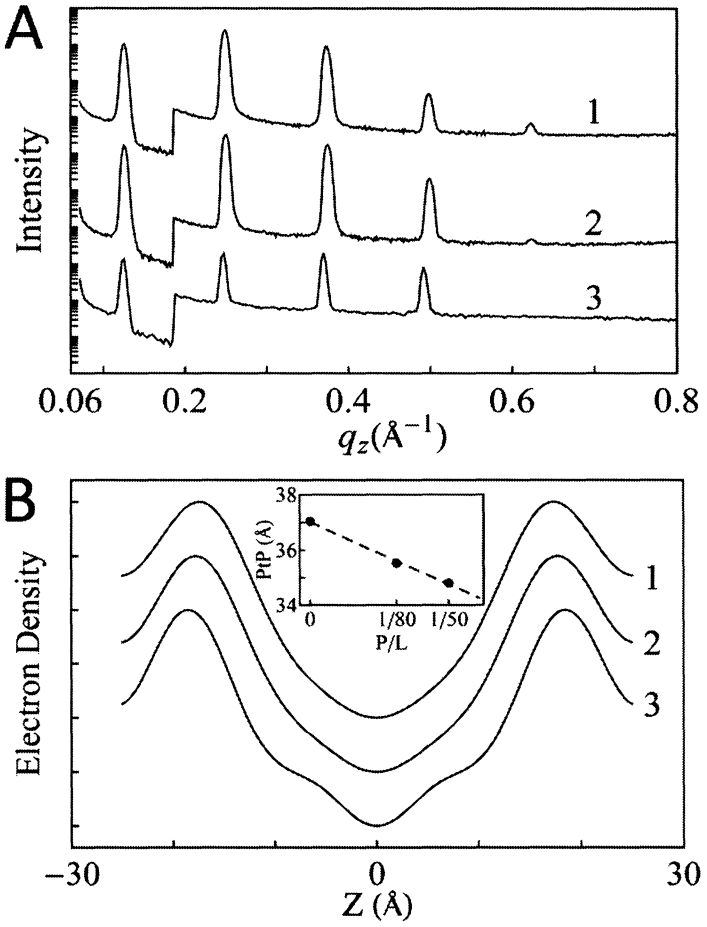

Figure 5-5 X-ray lamellar diffraction of open samples of (1) P/L = 1/50, (2) P/L = 1/80, and (3) pure DOPC (all at ~98% RH, 25°C). (A) diffraction patterns. (B) constructed electron density profiles across one unit cell (the coordinate z normal to the bilayer) from which the peak-to-peak (PtP) was measured and plotted in the inset as a function of P/L.

5.3.4. Effects of LL-37 Binding on GUVs

GUVs with lipid dye (red) in the bilayers and solution dye (green) in their contents were brought to a solution containing 5 μM LL-37. Leakage occurred stochastically (i.e., at random times) to individual GUVs as observed in magainin leakage experiment [112]. Fig. 5-6A shows one example, in which the content dye leaked out in about 100 sec while the vesicle remained intact. This was to show that the pores induced by LL-37 were stable (not expanding indefinitely or disappeared during the experimental time) and did not disintegrate the lipid vesicle.

The method of aspiration [70] allowed us to distinguish the surface binding from the pore formation [7, 57, 110, 111]. A GUV formed in 200 mM sucrose solution was aspirated and brought to an isotonic glucose/HEPES solution containing 0.5 μM LL-37 (Fig. 5-6B). The binding of the peptide initially expanded the protrusion inside the pipette which allowed us to calculate the fractional area expansion $\Delta A/A$ [70]. The protrusion length reached a maximum and then began to decrease. This was the indication of pore formation in the membrane and the influx of the smaller sugar (glucose) molecules exceeding the outflow of the larger sugar (sucrose) molecules resulting in an increase of the GUV volume [110, 111]. The same experiment was repeated 9 times with an average maximum $\Delta A/A$ = 1.3 ± 0.7 %.

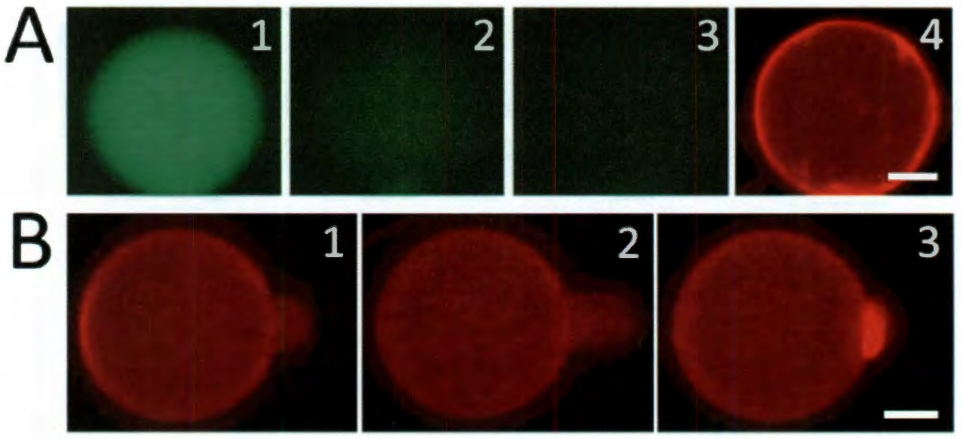

Figure 5-6 (A) A GUV with red dye in the lipid and green dye in its content was exposed to 5 μM LL-37. Leakage occurred stochastically. (1) t = 0, right before leakage occurred. (2) t = 30 sec. (3) t = 60 sec. (4) t = 300 sec, the GUV was still intact. In 60 sec, the leakage reduced the content dye intensity to ~10% of the t = 0 value, while photo-bleaching decreased the intensity of a non-leaking GUV to ~90%. Leakage was complete at t ~200 sec. (B) (1) An aspirated GUV was exposed to 0.5 μM LL-37. (2) The protrusion length initially increased indicating a membrane area expansion without pore formation; the image shows the maximum protrusion. (3) After reaching the maximum, the protrusion length decreased indicating pore formation in the membrane . In 9 runs of aspiration experiments, the average time to reach the maximum protrusion was ~13 sec and the average time for decreasing to the original protrusion length (where ΔA/A=0) was ~10 sec. Both scale bars =10 μm.

5.4. Discussion

The stability of the pores induced by LL-37 was demonstrated by the leakage experiment from GUVs. When a GUV was exposed to LL-37 in the solution, the dye inside the vesicle leaked out while the vesicle remained intact (Fig. 5-6). This indicated the formation of finite-sized pores in the membrane of GUV, lasting the entire experimental time. The same phenomena have been observed with magainin by Tamba and Yamazaki [112]. This observation did not imply pore-size stability during the kinetic process. Recent kinetic studies showed that the pores induced by magainin and other pore-forming peptides initially leaked out large-size dye molecules but only smaller ones at later time [113, 144]. Whether LL-37 has similar pore-size kinetics remains to be investigated. All these pore-forming peptides, including LL-37, did not dissolve the lipid bilayer as a detergent would.

The experiment with aspirated GUVs provided further insight into the process [7, 57, 110, 111]. In this experiment, the amount of peptide bound to the GUV, or the P/L, increased with time. The initial phase of LL-37 binding extended the protrusion length inside the micropipette, indicating a membrane area expansion of the GUV without pore formation [70]. When the fractional area expansion $\Delta A/A$ reached a value $\sim$1.3%, the protrusion length began to decrease, indicating the formation of pores in the membrane. The decrease of the protrusion length was due to the finite-size of the peptide induced pores that allowed the permeation of the smaller glucose more than the permeation of the larger sucrose; and the resulted osmolality imbalance induced a net water influx. This increase and

then decrease of the GUV protrusion has been carefully analyzed with other peptides, with variations of sugar concentrations and with the exchange of sucrose and glucose [7, 57, 110, 111]. The maximum area expansion $\Delta A/A$ of GUV can be directly related to a critical peptide concentration P/L*: $(\Delta A/A)_{max}$ = (P/L)*(A_P/ A_LE***rro***r! Bookmark not defined. [92]) [111]. From the values of $(\Delta A/A)_{max}$, A_P *and* A_L , we obtained P/L* ~ 1/320. This is the critical P/L value. When the P/L of the peptides adsorbed to the bilayer was below P/L*, the bound peptides expanded the membrane area without pore formation. Further binding of the solution peptides to the GUV made P/L exceed P/L*, then the peptides began to form pores. This P/L* value for LL-37 in DOPC is too small to be measured in equilibrium experiments. To detect the peptides or the effect of peptides in stacked membranes by OCD or X-ray/neutron techniques, P/L needs to be ~1/150 or greater. For example, melittin in di20:1PC (P/L* ~ 1/70) and in di22:1PC (P/L* ~ 1/40), the same value of P/L* was obtained separately by kinetic and equilibrium experiments [111].

The structural data obtained from stacked membranes of peptide-lipid mixtures corroborated the GUV findings. When the P/L of the peptide-lipid mixture was above P/L*, a substantial fraction of LL-37 peptides embedded in the bilayer with their helical axes normal to the plane of the bilayer, consistent with pore formation. The surprise finding was that the normal orientation of LL-37 helices was observed only in swollen states which had the D spacing exceeding ~70 Å, but not observed in the same stacked membranes fully hydrated by ~100% RH water

vapor, which had a D spacing ~52 Å, or in any dryer condition. We assume that stacked membranes at larger D spacings are closer to the situation where peptides interact with bilayer membranes in solution.

In swollen states with P/L > P/L*, neutron scattering indeed found LL-37 forming transmembrane pores in lipid bilayers with a water channel, but no pores were detected at non-swollen conditions. Since the primary purpose of this investigation was to determine if LL-37 forms pores, we only measured LL-37 in DOPC bilayers in two P/L values 1/80 and 1/50. Pores were detected in both cases, with the water channel radius at 23 and 33 Å, respectively. Much more systematic neutron studies have been done previously on the pores formed by smaller peptides, i.e., alamethicin [24], magainin [138], melittin [29] and protegrin [135]. We have analyzed, and confirmed by anomalous X-ray diffraction, two types of peptide-induced transmembrane pores: the barrel-stave pore and the toroidal pore [21, 29, 141]. Only the special peptide alamethicin, which is electrically neutral and barely soluble in water, forms barrel-stave pores. All other peptides, which are highly cationic and water soluble, form toroidal pores. Toroidal pores of magainin, melittin and protegrin have water channel radii in the range of 15-25 Å, and are variable in size depending on the peptide-lipid ratio and on the lipid composition [138]. The toroidal pores are substantially larger than the barrel stave pores of alamethicin, which have a water channel radius 9 Å [24]. The pores formed by LL-37 are characteristic of the toroidal type. The GUV experiments are consist with LL-37 binding on the membrane surface at low P/L ratios and forming transmembrane

pores at high P/L ratios. Its mechanism is consistent with the two-state model exhibited by magainin and protegrin [22].

Human cathelicidin LL-37 is a widely expressed archetypal AMP [118]. Recently the activity of the Alzheimer's disease-associated amyloid β-protein against microbial organisms was compared to the microbicidal activity of LL-37 [145]. It is significant that, despite the versatile multifunctionality of LL-37, our experimental results suggest that its molecular mechanism for direct antimicrobial activity might be similar to that of smaller AMPs, such as magainin and protegrin. Finally, we wonder if the necessity of studying LL-37 in swollen states implies that a similar consideration should be applied to other large membrane-active peptides and proteins.

Chapter 6

Conclusions

There are several goals which we achieve in this work. First, we have demonstrated the nucleation process of β-amyloid formation explicitly in our membrane system. Thus we have provided a first experimental support for the Jarrett-Lansbury's seeded polymerization model. Second, with the knowledge of how membrane binding facilitates nucleation-dependent β-aggregation, we further investigated the physical process of how hIAPP causes membrane damages. Third, a controversial peptide LL-37, which we discovered forming toroidal pores, is studied as a contrast to amyloid-forming peptides to demonstrate the generality of the two-state model.

The current understanding of amyloid formation by proteins is based on the nucleation theory proposed by Jarrett and Lansbury in 1993. As Jarrett and Lansbury pointed out, experimental proof for a seeded polymerization model is

difficult due to the near impossibility of quantifying the intermediate products during the aggregation. Although the theory is highly believable, it has so far received little direct experimental support. Therefore we wish to draw attention to our experimental results that provide explicit support for the Jarrett-Lansbury model: first, the existence of a nucleation process and second, the growth of β-aggregates once the nucleus has formed. Most importantly, we have demonstrated the catalytic role of membrane binding in facilitating the nucleation. In contrast to amyloid formation in solution, the membrane mediated version of the Jarrett-Lansbury model can be observed and quantified through its effect on the lipid bilayers. Penetratin is monomeric monomer in water solution. However, even at low concentrations (e.g., 0.1 μM) penetratin form β aggregates in the presence of anionic lipid vesicles. The mechanism for the formation of β aggregates described above is not specific to penetratin. The same mechanism is likely applicable to other peptides, such as Alzheimer's Aβ 1-40 which has exhibited the same conformation changes as penetratin does with lipid charge and with peptide concentration. Aβ 1-40 is present extracellularly as a soluble peptide in human cerebrospinal fluid at extremely low concentrations (in the range of nM). However, if it binds and accumulates on cell membranes, the mechanism described here could turn the peptide into β-amyloid.

The study of hIAPP interacting with lipid bilayer membrane is an extended investigation on amyloid-forming peptides. Our experimental results showed that unlike α-monomers bind on the interface of lipid bilayers, β-aggregates of hIAPP

bind on the surface of lipid bilayers. The behavior of hIAPP is identical to our finding of the amyloidogenic peptide penetratin. Peptides in the α-helical form binds in the headgroup region of the bilayer, but once the peptides aggregate to the β form via membrane-binding, they bind on the surface of the bilayer. This behavior showed by penetratin and hIAPP could be a general pattern of interaction between amyloid-forming peptides and lipid bilayers. The GUV experiments with monomeric hIAPP imply that there is a threshold bound peptide-to-lipid ratio, below which the bound peptide form does not convert to β-aggregates. This behavior of hIAPP is also similar to the behavior of penetratin. Such a threshold is important because the binding of hIAPP does not damage the lipid bilayer until the peptide aggregates into large size β-fibrils. The process of this membrane-mediated conformation change to β-aggregrate probably extracts lipid molecules from lipid membrane. This extraction process does not damage lipid membrane as long as the β-aggregates are small in size. However, small β-aggregates seed the formation of fibrils, as demonstrated by the Jarrett-Lansbury model. The large size fibrils eventually rapture the lipid bilayer via electrostatic and hydrophobic interactions.

The formation of the β-aggregates on the bilayer membrane can also be explained by a two-state model proposed by Huang to understand the action of antimicrobial peptides. Through the investigation on human antimicrobial peptide LL-37, we found out that the pores formed by LL-37 are characteristic of the toroidal type. The GUV experiments are consistent with LL-37 binding on the membrane surface at low P/L ratios and forming transmembrane pores at high P/L

ratios. Its mechanism is consistent with the two-state model exhibited by magainin and melittin. i.e., peptides first bind on the interface of lipid chain region as the first state (the surface state) and increase the free energy of peptide binding. Once the energy exceeds a certain threshold value, the binding peptide goes to the second state (the insertion state) which has a lower free energy. The inserted peptides then aggregate to form pores on the lipid membranes. Similar to the two-state model of antimicrobial peptides, the first state for the amyloid-related peptides is α-helical binding on the membrane interface. This surface binding stretches the membrane area and hence causes the free energy of surface binding increase. Once the free energy of surface binding exceeds a threshold value, the binding peptide goes to the second state, the aggregate state as in the case of amyloid-forming peptides. This aggregate state is facilitated by accumulating surface binding on the bilayer membrane that increases the chemical potential of the interfacial bound state.

References

1. Seifert, K., K. Fendler, and E. Bamberg (1993) Charge Transport by Ion Translocating Membrane-Proteins on Solid Supported Membranes. *Biophysical Journal.* 64: 384-391.
2. Spruce, A.E., A. Iwata, J.M. White, and W. Almers (1989) Patch Clamp Studies of Single Cell-Fusion Events Mediated by a Viral Fusion Protein. *Nature.* 342: 555-558.
3. Singer, S.J. and G.L. Nicolson (1972) Fluid Mosaic Model of Structure of Cell-Membranes. *Science.* 175: 720-&.
4. Hung, W.C., M.T. Lee, F.Y. Chen, and H.W. Huang (2007) The condensing effect of cholesterol in lipid bilayers. *Biophysical Journal.* 92: 3960-3967.
5. He, K., S.J. Ludtke, H.W. Huang, and D.L. Worcester (1995) Antimicrobial Peptide Pores in Membranes Detected by Neutron Inplane Scattering. *Biochemistry.* 34: 15614-15618.
6. Wu, Y., H.W. Huang, and G.A. Olah (1990) Method of Oriented Circular-Dichroism. *Biophysical Journal.* 57: 797-806.
7. Sun, Y., C.C. Lee, W.C. Hung, F.Y. Chen, M.T. Lee, and H.W. Huang (2008) The bound states of amphipathic drugs in lipid bilayers: study of curcumin. *Biophys J.* 95: 2318-24.
8. Sun, Y., C.C. Lee, T.H. Chen, and H.W. Huang (2010) Kinetic Process of beta-Amyloid Formation via Membrane Binding. *Biophysical Journal.* 99: 544-552.
9. Terzi, E., G. Holzemann, and J. Seelig (1997) Interaction of Alzheimer beta-amyloid peptide(1-40) with lipid membranes. *Biochemistry.* 36: 14845-14852.
10. Terzi, E., G. Holzemann, and J. Seelig (1995) Self-association of beta-amyloid peptide (1-40) in solution and binding to lipid membranes. *J Mol Biol.* 252: 633-42.
11. Lindberg, M., H. Biverstahl, A. Graslund, and L. Maler (2003) Structure and positioning comparison of two variants of penetratin in two different membrane mimicking systems by NMR. *Eur J Biochem.* 270: 3055-63.
12. Magzoub, M., L.E. Eriksson, and A. Graslund (2002) Conformational states of the cell-penetrating peptide penetratin when interacting with phospholipid vesicles: effects of surface charge and peptide concentration. *Biochim Biophys Acta.* 1563: 53-63.
13. Magzoub, M., L.E. Eriksson, and A. Graslund (2003) Comparison of the interaction, positioning, structure induction and membrane perturbation of cell-penetrating peptides and non-translocating variants with phospholipid vesicles. *Biophys Chem.* 103: 271-88.
14. Wong, P.T., J.A. Schauerte, K.C. Wisser, H. Ding, E.L. Lee, D.G. Steel, and A. Gafni (2009) Amyloid-beta membrane binding and permeabilization are distinct processes influenced separately by membrane charge and fluidity. *J Mol Biol.* 386: 81-96.

15. Gepts, W. and P.M. Lecompte (1981) The pancreatic islets in diabetes. *Am J Med.* 70: 105-15.
16. Janson, J., R.H. Ashley, D. Harrison, S. McIntyre, and P.C. Butler (1999) The mechanism of islet amyloid polypeptide toxicity is membrane disruption by intermediate-sized toxic amyloid particles. *Diabetes.* 48: 491-8.
17. Anguiano, M., R.J. Nowak, and P.T. Lansbury, Jr. (2002) Protofibrillar islet amyloid polypeptide permeabilizes synthetic vesicles by a pore-like mechanism that may be relevant to type II diabetes. *Biochemistry.* 41: 11338-43.
18. Jayasinghe, S.A. and R. Langen (2007) Membrane interaction of islet amyloid polypeptide. *Biochim Biophys Acta.* 1768: 2002-9.
19. Haataja, L., T. Gurlo, C.J. Huang, and P.C. Butler (2008) Islet amyloid in type 2 diabetes, and the toxic oligomer hypothesis. *Endocr Rev.* 29: 303-16.
20. Soong, R., J.R. Brender, P.M. Macdonald, and A. Ramamoorthy (2009) Association of highly compact type II diabetes related islet amyloid polypeptide intermediate species at physiological temperature revealed by diffusion NMR spectroscopy. *J Am Chem Soc.* 131: 7079-85.
21. Qian, S., W. Wang, L. Yang, and H.W. Huang (2008) Structure of transmembrane pore induced by Bax-derived peptide: evidence for lipidic pores. *Proc Natl Acad Sci U S A.* 105: 17379-83.
22. Huang, H.W. (2000) Action of antimicrobial peptides: two-state model. *Biochemistry.* 39: 8347-52.
23. Powers, L. and P.S. Pershan (1977) Monodomain samples of dipalmitoyl phosphatidylcholine with varying concentrations of water and other ingredients. *Biophys J.* 20: 137-52.
24. He, K., S.J. Ludtke, D.L. Worcester, and H.W. Huang (1996) Neutron scattering in the plane of membranes: structure of alamethicin pores. *Biophys J.* 70: 2659-66.
25. Lynn, G.W., W.T. Heller, V. Urban, G.D. Wignall, K. Weiss, and D.A. Myles (2006) Bio-SANS—A dedicated facility for neutron structural biology at Oak Ridge National Laboratory *Physica B: Condensed Matter.* 385-386: 880-882.
26. Wu, Y., H.W. Huang, and G.A. Olah (1990) Method of oriented circular dichroism. *Biophys J.* 57: 797-806.
27. Huang, H.W. and Y. Wu (1991) Lipid-Alamethicin Interactions Influence Alamethicin Orientation. *Biophysical Journal.* 60: 1079-1087.
28. Ludtke, S.J., K. He, Y.L. Wu, and H.W. Huang (1994) Cooperative Membrane Insertion of Magainin Correlated with Its Cytolytic Activity. *Biochimica Et Biophysica Acta-Biomembranes.* 1190: 181-184.
29. Yang, L., T.A. Harroun, T.M. Weiss, L. Ding, and H.W. Huang (2001) Barrel-stave model or toroidal model? a case study on melittin pores. *Biophys J.* 81: 1475-1485.
30. Lee, C.C., Y. Sun, S. Qian, and H.W. Huang (2011) Transmembrane Pores Formed by Human Antimicrobial Peptide LL-37. *Biophysical Journal.* 100: 1688-1696.

31. Evans, E. and D. Needham (1987) Physical-Properties of Surfactant Bilayer-Membranes - Thermal Transitions, Elasticity, Rigidity, Cohesion, and Colloidal Interactions. *Journal of Physical Chemistry.* 91: 4219-4228.
32. Rawicz, W., K.C. Olbrich, T. McIntosh, D. Needham, and E. Evans (2000) Effect of chain length and unsaturation on elasticity of lipid bilayers. *Biophysical Journal.* 79: 328-339.
33. Evans, E. and M. Metcalfe (1984) Free-Energy Potential for Aggregation of Giant, Neutral Lipid Bilayer Vesicles by Vanderwaals Attraction. *Biophysical Journal.* 46: 423-426.
34. Evans, E. and D. Needham (1988) Attraction between Lipid Bilayer-Membranes in Concentrated-Solutions of Nonadsorbing Polymers - Comparison of Mean-Field Theory with Measurements of Adhesion Energy. *Macromolecules.* 21: 1822-1831.
35. Evans, E., D. Needham, and J. Janzen (1987) Nonspecific Adhesion of Phospholipid-Bilayer Membranes in Solutions of Plasma-Proteins - Measurement of Free-Energy Potentials and Theoretical Concepts. *Acs Symposium Series.* 343: 88-102.
36. Sun, Y., C.C. Lee, and H.W. Huang (2011) Adhesion and Merging of Lipid Bilayers: A Method for Measuring the Free Energy of Adhesion and Hemifusion. *Biophysical Journal.* 100: 987-995.
37. Angelova, M.I., *Liposome Electroformation*, in *Giant Vesicles*, P.L. Luisi and P. Walde, Editors. 2000, John Wiley & Sons: Chichester. p. pp. 27-36.
38. Jarrett, J.T. and P.T. Lansbury, Jr. (1993) Seeding "one-dimensional crystallization" of amyloid: a pathogenic mechanism in Alzheimer's disease and scrapie? *Cell.* 73: 1055-8.
39. Derossi, D., A.H. Joliot, G. Chassaing, and A. Prochiantz (1994) The third helix of the Antennapedia homeodomain translocates through biological membranes. *J Biol Chem.* 269: 10444-50.
40. Koppaka, V., C. Paul, I.V. Murray, and P.H. Axelsen (2003) Early synergy between Abeta42 and oxidatively damaged membranes in promoting amyloid fibril formation by Abeta40. *J Biol Chem.* 278: 36277-84.
41. Matsuzaki, K. (2007) Physicochemical interactions of amyloid beta-peptide with lipid bilayers. *Biochim Biophys Acta.* 1768: 1935-42.
42. Chi, E.Y., C. Ege, A. Winans, J. Majewski, G. Wu, K. Kjaer, and K.Y. Lee (2008) Lipid membrane templates the ordering and induces the fibrillogenesis of Alzheimer's disease amyloid-beta peptide. *Proteins.* 72: 1-24.
43. Relini, A., O. Cavalleri, R. Rolandi, and A. Gliozzi (2009) The two-fold aspect of the interplay of amyloidogenic proteins with lipid membranes. *Chem Phys Lipids.* 158: 1-9.
44. Chiti, F. and C.M. Dobson (2006) Protein misfolding, functional amyloid, and human disease. *Annu Rev Biochem.* 75: 333-66.
45. Qian, Y.Q., M. Billeter, G. Otting, M. Muller, W.J. Gehring, and K. Wuthrich (1989) The structure of the Antennapedia homeodomain determined by

NMR spectroscopy in solution: comparison with prokaryotic repressors. *Cell.* 59: 573-80.

46. Melikov, K. and L.V. Chernomordik (2005) Arginine-rich cell penetrating peptides: from endosomal uptake to nuclear delivery. *Cell Mol Life Sci.* 62: 2739-49.
47. Fischer, R., M. Fotin-Mleczek, H. Hufnagel, and R. Brock (2006) Break on through to the other side-biophyiscs and cell biology shet light on cell-penetrating peptides. *Chembiochem.* 6: 2126-2142.
48. Duchardt, F., M. Fotin-Mleczek, H. Schwarz, R. Fischer, and R. Brock (2007) A comprehensive model for the cellular uptake of cationic cell-penetrating peptides. *Traffic.* 8: 848-66.
49. Zasloff, M. (2002) Antimicrobial peptides of multicellular organisms. *Nature.* 415: 389-95.
50. Drin, G., H. Demene, J. Temsamani, and R. Brasseur (2001) Translocation of the pAntp peptide and its amphipathic analogue AP-2AL. *Biochemistry.* 40: 1824-34.
51. Thoren, P.E., D. Persson, M. Karlsson, and B. Norden (2000) The antennapedia peptide penetratin translocates across lipid bilayers - the first direct observation. *FEBS Lett.* 482: 265-8.
52. Persson, D., P.E. Thoren, M. Herner, P. Lincoln, and B. Norden (2003) Application of a novel analysis to measure the binding of the membrane-translocating peptide penetratin to negatively charged liposomes. *Biochemistry.* 42: 421-9.
53. Matsuzaki, K. (1999) Why and how are peptide-lipid interactions utilized for self-defense? Magainins and tachyplesins as archetypes. *Biochim Biophys Acta.* 1462: 1-10.
54. Shai, Y. (1999) Mechanism of the binding, insertion and destabilization of phospholipid bilayer membranes by alpha-helical antimicrobial and cell non-selective membrane-lytic peptides. *Biochim Biophys Acta.* 1462: 55-70.
55. Hung, W.C., F.Y. Chen, C.C. Lee, Y. Sun, M.T. Lee, and H.W. Huang (2008) Membrane-thinning effect of curcumin. *Biophys J.* 94: 4331-8.
56. Seelig, A. (2007) The role of size and charge for blood-brain barrier permeation of drugs and fatty acids. *J Mol Neurosci.* 33: 32-41.
57. Sun, Y., W.C. Hung, F.Y. Chen, C.C. Lee, and H.W. Huang (2009) Interaction of tea catechin (-)-epigallocatechin gallate with lipid bilayers. *Biophys J.* 96: 1026-35.
58. Huang, H.W. (2009) Free energies of molecular bound states in lipid bilayers: lethal concentrations of antimicrobial peptides. *Biophys J.* 96: 3263-72.
59. Su, Y., R. Mani, T. Doherty, A.J. Waring, and M. Hong (2008) Reversible sheet-turn conformational change of a cell-penetrating peptide in lipid bilayers studied by solid-state NMR. *J Mol Biol.* 381: 1133-44.

60. Beschiaschvili, G. and J. Seelig (1990) Melittin binding to mixed phosphatidylglycerol/phosphatidylcholine membranes. *Biochemistry.* 29: 52-8.
61. Wenk, M.R. and J. Seelig (1998) Magainin 2 amide interaction with lipid membranes: calorimetric detection of peptide binding and pore formation. *Biochemistry.* 37: 3909-16.
62. Christiaens, B., S. Symoens, S. Verheyden, Y. Engelborghs, A. Joliot, A. Prochiantz, J. Vandekerckhove, M. Rosseneu, and B. Vanloo (2002) Tryptophan fluorescence study of the interaction of penetratin peptides with model membranes. *Eur J Biochem.* 269: 2918-26.
63. Ludtke, S., K. He, and H. Huang (1995) Membrane thinning caused by magainin 2. *Biochemistry.* 34: 16764-9.
64. Harroun, T.A., W.T. Heller, T.M. Weiss, L. Yang, and H.W. Huang (1999) Experimental evidence for hydrophobic matching and membrane-mediated interactions in lipid bilayers containing gramicidin. *Biophys J.* 76: 937-45.
65. Wu, Y., K. He, S.J. Ludtke, and H.W. Huang (1995) X-ray Diffraction Study of Lipid Bilayer Membrane Interacting with Amphiphilic Helical Peptides: Diphytanoyl Phosphatidylcholine with Alamethicin at Low Concentrations. *Biophys J.* 68: 2361-2369.
66. Weiss, T.M., P.C. van der Wel, J.A. Killian, R.E. Koeppe, 2nd, and H.W. Huang (2003) Hydrophobic mismatch between helices and lipid bilayers. *Biophys J.* 84: 379-85.
67. Blaurock, A.E. (1971) Structure of the nerve myelin membrane: proof of the low-resolution profile. *J Mol Biol.* 56: 35-52.
68. Olah, G.A., H.W. Huang, W.H. Liu, and Y.L. Wu (1991) Location of ion-binding sites in the gramicidin channel by X-ray diffraction. *J Mol Biol.* 218: 847-58.
69. Yang, L. and H.W. Huang (2003) A rhombohedral phase of lipid containing a membrane fusion intermediate structure. *Biophys J.* 84: 1808-17.
70. Kwok, R. and E. Evans (1981) Thermoelasticity of large lecithin bilayer vesicles. *Biophys J.* 35: 637-52.
71. Warren, B.E., *X-ray Diffraction*. 1990, Mineola, N.Y.; pp. 41-47, 51-54.: Dover Publications,. pp. 41-47, 51-54.
72. Chen, F.Y., W.C. Hung, and H.W. Huang (1997) Critical swelling of phospholipid bilayers. *Phys. Rev. Lett.* 79: 4026-4029.
73. Buldt, G., H.U. Gally, A. Seelig, J. Seelig, and G. Zaccai (1978) Neutron diffraction studies on selectively deuterated phospholipid bilayers. *Nature.* 271: 182-4.
74. Lee, M.T., F.Y. Chen, and H.W. Huang (2004) Energetics of pore formation induced by membrane active peptides. *Biochemistry.* 43: 3590-9.
75. Olah, G.A. and H.W. Huang (1988) Circular dichroism of oriented α-helices. *J. Chem. Phys.* 89: 2531-2538.
76. Fox, R.O., Jr. and F.M. Richards (1982) A voltage-gated ion channel model inferred from the crystal structure of alamethicin at 1.5-A resolution. *Nature.* 300: 325-30.

77. Seemann, H. and R. Winter (2003) Volumetric properties, compressibilities, and volume fluctuations in phospholipid-cholesterol bilayers. *Z. Phys. Chem.* 217: 831-846.
78. Nagle, J.F. and S. Tristram-Nagle (2000) Structure of lipid bilayers. *Biochim Biophys Acta.* 1469: 159-95.
79. Rawicz, W., K.C. Olbrich, T. McIntosh, D. Needham, and E. Evans (2000) Effect of chain length and unsaturation on elasticity of lipid bilayers. *Biophys J.* 79: 328-39.
80. Blankschtein, D., G.M. Thurston, and G.B. Benedek (1986) Phenomenological theory of equilibrium thermodynamic properties and phase separation of micellar solutions. *J. Chem. Phys.* 85: 7268-7288.
81. Debye, P. (1949) Light scattering in soap solutions. *Ann. N.Y. Acad. Sci.* 51: 575-592.
82. CDC, *Centers for Disease Control and Prevention. Atlanta, GA* http://www.cdc.gov/diabetes/pubs/pdf/ndfs_2011.pdf.
83. Konarkowska, B., J.F. Aitken, J. Kistler, S. Zhang, and G.J. Cooper (2006) The aggregation potential of human amylin determines its cytotoxicity towards islet beta-cells. *FEBS J.* 273: 3614-24.
84. Sanke, T., G.I. Bell, C. Sample, A.H. Rubenstein, and D.F. Steiner (1988) An islet amyloid peptide is derived from an 89-amino acid precursor by proteolytic processing. *J Biol Chem.* 263: 17243-6.
85. Westermark, P., U. Engstrom, K.H. Johnson, G.T. Westermark, and C. Betsholtz (1990) Islet amyloid polypeptide: pinpointing amino acid residues linked to amyloid fibril formation. *Proc Natl Acad Sci U S A.* 87: 5036-40.
86. Huang, C.J., C.Y. Lin, L. Haataja, T. Gurlo, A.E. Butler, R.A. Rizza, and P.C. Butler (2007) High expression rates of human islet amyloid polypeptide induce endoplasmic reticulum stress mediated beta-cell apoptosis, a characteristic of humans with type 2 but not type 1 diabetes. *Diabetes.* 56: 2016-27.
87. Matveyenko, A.V. and P.C. Butler (2006) Islet amyloid polypeptide (IAPP) transgenic rodents as models for type 2 diabetes. *ILAR J.* 47: 225-33.
88. Meier, J.J., R. Kayed, C.Y. Lin, T. Gurlo, L. Haataja, S. Jayasinghe, R. Langen, C.G. Glabe, and P.C. Butler (2006) Inhibition of human IAPP fibril formation does not prevent beta-cell death: evidence for distinct actions of oligomers and fibrils of human IAPP. *Am J Physiol Endocrinol Metab.* 291: E1317-24.
89. Vaiana, S.M., R. Ghirlando, W.M. Yau, W.A. Eaton, and J. Hofrichter (2008) Sedimentation studies on human amylin fail to detect low-molecular-weight oligomers. *Biophys J.* 94: L45-7.
90. Kayed, R., Y. Sokolov, B. Edmonds, T.M. McIntire, S.C. Milton, J.E. Hall, and C.G. Glabe (2004) Permeabilization of lipid bilayers is a common conformation-dependent activity of soluble amyloid oligomers in protein misfolding diseases. *J Biol Chem.* 279: 46363-6.
91. Sumner Makin, O. and L.C. Serpell (2004) Structural characterisation of islet amyloid polypeptide fibrils. *J Mol Biol.* 335: 1279-88.

92. Balbirnie, M., R. Grothe, and D.S. Eisenberg (2001) An amyloid-forming peptide from the yeast prion Sup35 reveals a dehydrated beta-sheet structure for amyloid. *Proc Natl Acad Sci U S A.* 98: 2375-80.
93. Nelson, R., M.R. Sawaya, M. Balbirnie, A.O. Madsen, C. Riekel, R. Grothe, and D. Eisenberg (2005) Structure of the cross-beta spine of amyloid-like fibrils. *Nature.* 435: 773-8.
94. Nielsen, L., R. Khurana, A. Coats, S. Frokjaer, J. Brange, S. Vyas, V.N. Uversky, and A.L. Fink (2001) Effect of environmental factors on the kinetics of insulin fibril formation: elucidation of the molecular mechanism. *Biochemistry.* 40: 6036-46.
95. Butler, P.C., J. Chou, W.B. Carter, Y.N. Wang, B.H. Bu, D. Chang, J.K. Chang, and R.A. Rizza (1990) Effects of meal ingestion on plasma amylin concentration in NIDDM and nondiabetic humans. *Diabetes.* 39: 752-6.
96. Jayasinghe, S.A. and R. Langen (2005) Lipid membranes modulate the structure of islet amyloid polypeptide. *Biochemistry.* 44: 12113-9.
97. Knight, J.D. and A.D. Miranker (2004) Phospholipid catalysis of diabetic amyloid assembly. *J Mol Biol.* 341: 1175-87.
98. Knight, J.D., J.A. Hebda, and A.D. Miranker (2006) Conserved and cooperative assembly of membrane-bound alpha-helical states of islet amyloid polypeptide. *Biochemistry.* 45: 9496-508.
99. Sparr, E., M.F. Engel, D.V. Sakharov, M. Sprong, J. Jacobs, B. de Kruijff, J.W. Hoppener, and J.A. Killian (2004) Islet amyloid polypeptide-induced membrane leakage involves uptake of lipids by forming amyloid fibers. *FEBS Lett.* 577: 117-20.
100. Gorbenko, G.P. and P.K. Kinnunen (2006) The role of lipid-protein interactions in amyloid-type protein fibril formation. *Chem Phys Lipids.* 141: 72-82.
101. Apostolidou, M., S.A. Jayasinghe, and R. Langen (2008) Structure of alpha-helical membrane-bound human islet amyloid polypeptide and its implications for membrane-mediated misfolding. *J Biol Chem.* 283: 17205-10.
102. Quist, A., I. Doudevski, H. Lin, R. Azimova, D. Ng, B. Frangione, B. Kagan, J. Ghiso, and R. Lal (2005) Amyloid ion channels: a common structural link for protein-misfolding disease. *Proc Natl Acad Sci U S A.* 102: 10427-32.
103. Kawahara, M., Y. Kuroda, N. Arispe, and E. Rojas (2000) Alzheimer's beta-amyloid, human islet amylin, and prion protein fragment evoke intracellular free calcium elevations by a common mechanism in a hypothalamic GnRH neuronal cell line. *J Biol Chem.* 275: 14077-83.
104. Mirzabekov, T.A., M.C. Lin, and B.L. Kagan (1996) Pore formation by the cytotoxic islet amyloid peptide amylin. *J Biol Chem.* 271: 1988-92.
105. Green, J.D., L. Kreplak, C. Goldsbury, X. Li Blatter, M. Stolz, G.S. Cooper, A. Seelig, J. Kistler, and U. Aebi (2004) Atomic force microscopy reveals defects within mica supported lipid bilayers induced by the amyloidogenic human amylin peptide. *J Mol Biol.* 342: 877-87.

106. Harroun, T.A., J.P. Bradshaw, and R.H. Ashley (2001) Inhibitors can arrest the membrane activity of human islet amyloid polypeptide independently of amyloid formation. *FEBS Lett.* 507: 200-4.
107. Zhao, H., E.K. Tuominen, and P.K. Kinnunen (2004) Formation of amyloid fibers triggered by phosphatidylserine-containing membranes. *Biochemistry.* 43: 10302-7.
108. Engel, M.F., L. Khemtemourian, C.C. Kleijer, H.J. Meeldijk, J. Jacobs, A.J. Verkleij, B. de Kruijff, J.A. Killian, and J.W. Hoppener (2008) Membrane damage by human islet amyloid polypeptide through fibril growth at the membrane. *Proc Natl Acad Sci U S A.* 105: 6033-8.
109. Lee, C.C., Y. Sun, and H.W. Huang (2010) Membrane-mediated peptide conformation change from alpha-monomers to beta-aggregates. *Biophys J.* 98: 2236-45.
110. Longo, M.L., A.J. Waring, L.M. Gordon, and D.A. Hammer (1998) Area expansion and permeation of phospholipid membrane bilayer by influenza fusion peptides and melittin. *Langmuir.* 14: 2385-2395.
111. Lee, M.T., W.C. Hung, F.Y. Chen, and H.W. Huang (2008) Mechanism and kinetics of pore formation in membranes by water-soluble amphipathic peptides. *Proc Natl Acad Sci U S A.* 105: 5087-92.
112. Tamba, Y. and M. Yamazaki (2005) Single giant unilamellar vesicle method reveals effect of antimicrobial peptide magainin 2 on membrane permeability. *Biochemistry.* 44: 15823-33.
113. Tamba, Y., H. Ariyama, V. Levadny, and M. Yamazaki (2010) Kinetic pathway of antimicrobial peptide magainin2 induced pore formation in lipid membranes. *J. Phys. Chem. B.* 114: 12018-12026.
114. Lis, L.J., W.T. Lis, V.A. Parsegian, and R.P. Rand (1981) Adsorption of divalent cations to a variety of phosphatidylcholine bilayers. *Biochemistry.* 20: 1771-7.
115. Alberts, B., A. Johnson, J. Lewis, M. Raff, K. Roberts, and P. Walter, *Molecular Biology of the Cell.* 4th Edition ed. 2002, New York: Garland Science.
116. Heimburg, T. (2010) Lipid ion channels. *Biophys Chem.* 150: 2-22.
117. Boman, H.G., J. Marsh, and J.A. Goode, eds. *Antimicrobial peptides.* Ciba Found Symp. Vol. 186. 1994, John Wiley and Sons: Chichester.
118. Zanetti, M. (2004) Cathelicidins, multifunctional peptides of the innate immunity. *J Leukoc Biol.* 75: 39-48.
119. Turner, J., Y. Cho, N.N. Dinh, A.J. Waring, and R.I. Lehrer (1998) Activities of LL-37, a cathelin-associated antimicrobial peptide of human neutrophils. *Antimicrob Agents Chemother.* 42: 2206-14.
120. Scott, M.G., D.J. Davidson, M.R. Gold, D. Bowdish, and R.E. Hancock (2002) The human antimicrobial peptide LL-37 is a multifunctional modulator of innate immune responses. *J Immunol.* 169: 3883-91.
121. Koczulla, R., G. von Degenfeld, C. Kupatt, F. Krotz, S. Zahler, T. Gloe, K. Issbrucker, P. Unterberger, M. Zaiou, C. Lebherz, A. Karl, P. Raake, A. Pfosser, P. Boekstegers, U. Welsch, P.S. Hiemstra, C. Vogelmeier, R.L. Gallo, M. Clauss,

and R. Bals (2003) An angiogenic role for the human peptide antibiotic LL-37/hCAP-18. *J Clin Invest.* 111: 1665-72.
122. Zaiou, M. (2007) Multifunctional antimicrobial peptides: therapeutic targets in several human diseases. *J Mol Med.* 85: 317-29.
123. De, Y., Q. Chen, A.P. Schmidt, G.M. Anderson, J.M. Wang, J. Wooters, J.J. Oppenheim, and O. Chertov (2000) LL-37, the neutrophil granule- and epithelial cell-derived cathelicidin, utilizes formyl peptide receptor-like 1 (FPRL1) as a receptor to chemoattract human peripheral blood neutrophils, monocytes, and T cells. *J Exp Med.* 192: 1069-74.
124. Oren, Z., J.C. Lerman, G.H. Gudmundsson, B. Agerberth, and Y. Shai (1999) Structure and organization of the human antimicrobial peptide LL-37 in phospholipid membranes: relevance to the molecular basis for its non-cell-selective activity. *Biochem J.* 341 (Pt 3): 501-13.
125. Porcelli, F., R. Verardi, L. Shi, K.A. Henzler-Wildman, A. Ramamoorthy, and G. Veglia (2008) NMR structure of the cathelicidin-derived human antimicrobial peptide LL-37 in dodecylphosphocholine micelles. *Biochemistry.* 47: 5565-72.
126. Henzler Wildman, K.A., D.K. Lee, and A. Ramamoorthy (2003) Mechanism of lipid bilayer disruption by the human antimicrobial peptide, LL-37. *Biochemistry.* 42: 6545-58.
127. Sood, R., Y. Domanov, M. Pietiainen, V.P. Kontinen, and P.K. Kinnunen (2008) Binding of LL-37 to model biomembranes: insight into target vs host cell recognition. *Biochim Biophys Acta.* 1778: 983-96.
128. Caille, A. (1972) Physique cristalline:remarques sur la diffusion des rayons X dans les smectiques. *A.C.R. Acad. Sci. Paris Ser. B.* 274: 891-893.
129. Lei, N., C.R. Safinya, and R.F. Bruinsma (1995) Discrete harmonic model for stacked membranes: theory and experiment. *J. Phys. II France.* 5: 1155-1163.
130. Safinya, C.R., D. Roux, G.S. Smith, S.K. Sinha, P. Dimon, N.A. Clark, and A.M. Bellocq (1986) Steric interactions in a model multimembrane system: a synchrotron X-ray study. *Phys. Rev. Lett.* 57: 2718-2721.
131. Wack, D.C. and W.W. Webb (1989) Measurement by X-ray diffraction methods of the layer compressional elastic constant B in the lyotropic smectic-A (L-alpha) phase of the lecithin-water system. *Phys. Rev. A.* 40: 1627-1636.
132. Ladokhin, A.S. and S.H. White (2004) Interfacial folding and membrane insertion of a designed helical peptide. *Biochemistry.* 43: 5782-91.
133. Burck, J., S. Roth, P. Wadhwani, S. Afonin, N. Kanithasen, E. Strandberg, and A.S. Ulrich (2008) Conformation and membrane orientation of amphiphilic helical peptides by OCD. *Biophys J.* 95: 3872-3881.
134. Cheng, J.T., J.D. Hale, M. Elliot, R.E. Hancock, and S.K. Straus (2009) Effect of membrane composition on antimicrobial peptides aurein 2.2 and 2.3 from Australian southern bell frogs. *Biophys J.* 96: 552-65.
135. Yang, L., T.M. Weiss, and H.W. Huang (2000) Crystallization of antimicrobial pores in membranes: Magainin and protegrin. *Biophys. J.* 79: 2002-2009.

136. Johansson, J., G.H. Gudmundsson, M.E. Rottenberg, K.D. Berndt, and B. Agerberth (1998) Conformation-dependent antibacterial activity of the naturally occurring human peptide LL-37. *J Biol Chem.* 273: 3718-24.
137. Terwilliger, T.C., L. Weissman, and D. Eisenberg (1982) The structure of melittin in the form I crystals and its implication for melittin's lytic and surface activities. *Biophys J.* 37: 353-61.
138. Ludtke, S.J., K. He, W.T. Heller, T.A. Harroun, L. Yang, and H.W. Huang (1996) Membrane pores induced by magainin. *Biochemistry.* 35: 13723-8.
139. Yang, L., T.A. Harroun, W.T. Heller, T.M. Weiss, and H.W. Huang (1998) Neutron off-plane scattering of aligned membranes. I. Method Of measurement. *Biophys J.* 75: 641-5.
140. Yang, L., T.M. Weiss, T.A. Harroun, W.T. Heller, and H.W. Huang (1999) Supramolecular structures of peptide assemblies in membranes by neutron off-plane scattering: method of analysis. *Biophys J.* 77: 2648-56.
141. Qian, S., W. Wang, L. Yang, and H.W. Huang (2008) Structure of the alamethicin pore reconstructed by X-ray diffraction analysis. *Biophys J.* 94: 3512-3522.
142. Mecke, A., D.K. Lee, A. Ramamoorthy, B.G. Orr, and M.M.B. Holl (2005) Membrane thinning due to antimicrobial peptide binding: An atomic force microscopy study of MSI-78 in lipid bilayers. *Biophysical Journal.* 89: 4043-4050.
143. Pabst, G., S. Danner, R. Podgornik, and J. Katsaras (2007) Entropy-driven softening of fluid lipid bilayers by alamethicin. *Langmuir.* 23: 11705-11.
144. Fuertes, G., A.J. Garcia-Saez, S. Esteban-Martin, D. Gimenez, O.L. Sanchez-Munoz, P. Schwille, and J. Salgado (2010) Pores formed by baxalpha5 relax to a smaller size and keep at equilibrium. *Biophys J.* 99: 2917-25.
145. Soscia, S.J., J.E. Kirby, K.J. Washicosky, S.M. Tucker, M. Ingelsson, B. Hyman, M.A. Burton, L.E. Goldstein, S. Duong, R.E. Tanzi, and R.D. Moir (2010) The Alzheimer's disease-associated amyloid beta-protein is an antimicrobial peptide. *PLoS One.* 5: e9505.

In general, the change of the GUV radius (ΔR_v) was too small to measure accurately under the fluorescence microscopy. However, with the method of the micropipette aspiration, protrusion length can be measured much more precisely. Therefore, if one tries to calculate the area change of a GUV, aspirated method will result in much more accurate quantitative results than non-aspirated one.

Under other conditions, such as pores formed by peptides on the GUV or osmotic pressure unbalanced inside and outside the GUV, the volume of the GUV would change due to water influx and efflux while the area of the GUV remains the same. Under such a condition ($\Delta A=0$), the change of the volume can also be directly related to the change of the protrusion length by

$$\Delta V = -\pi R_p (R_v - R_p)\Delta L \tag{2-26}$$

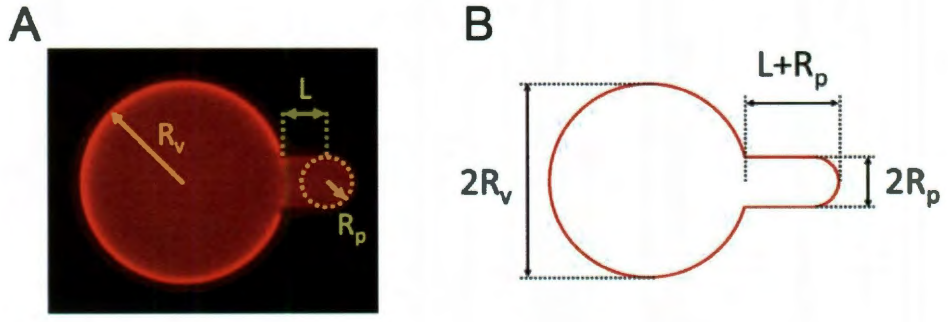

Figure 2-14 (A) A fluorescent image of an aspirated GUV. R_v is the radius of the GUV, R_p is the radius of the micropipette and L is the protrusion length inside the micropitette. (B) Schematic of how to analysis a GUV image. R_v and R_p are determined by the diameters of the GUV and micropipette. L is determined by the total protrusion length minus the radius of the micropipette.